Testing the GRB fireball scenario with GROND

Robert Filgas

Vollständiger Abdruck der von der Fakultät für Physik der Technischen Universität München zur Erlangung des akademischen Grades eines

Doktors der Naturwissenschaften (Dr. rer. nat.)

genehmigten Dissertation.

<table>
<tr><td>Vorsitzender:</td><td colspan="2">Univ.-Prof. Dr. Alejandro Ibarra</td></tr>
<tr><td>Prüfer der Dissertation:</td><td>1.</td><td>Priv.-Doz. Dr. Jochen Greiner</td></tr>
<tr><td></td><td>2.</td><td>Univ.-Prof. Dr. Lothar Oberauer</td></tr>
</table>

Die Dissertation wurde am 27.10.2011 bei der Technischen Universität München eingereicht und durch die Fakultät für Physik am 05.12.2011 angenommen.

Abstract

Gamma-ray bursts (GRBs) are the most compact and luminous electromagnetic explosions in the Universe. They emit a large amount of energy, of the order of $\sim 10^{51}$ erg in γ-rays, on very short time scales between 10^{-3} and 10^3 seconds. The leading model for the emission of GRBs is the fireball shock scenario, where the outflow reaches ultra-relativistic ($\Gamma > 100$) velocities and is collimated into a jet. The interactions between fireball shells with different speeds, so-called "internal shocks", are responsible for the prompt γ-ray emission, while the collisions of fireball shells with the external medium, so-called "external shocks", produce the afterglow emission, which can be detected in all wavelength ranges from radio, optical to X-rays, up to days or months after the explosion. This afterglow emission can be explained by a non-thermal synchrotron radiation.

This PhD thesis describes the scientific analysis of the GRB afterglow data obtained by the Gamma-Ray burst Optical/Near-infrared Detector (GROND), a seven-channel imager with four optical and three near-infrared (NIR) detectors, covering the wavelength range of $360 - 2300$ nm. Its unique capability to observe in all bands simultaneously, together with rapid triggering, precise photometry and high temporal resolution, give us the opportunity to study light curves and spectral energy distributions (SED) of GRB afterglows in unprecedented detail.

The thesis is structured as follows: Chapter 1 gives a basic description of GRBs, together with a brief history of the observational and theoretical progress in the field. The standard fireball scenario and various additions to it are described in detail afterwards. Chapter 2 contains instrumental details about the *Swift* satellite and GROND. The observations with GROND in the Rapid Response Mode are described, as well as the automatic triggering and reduction software. Data handling and the software tools developed for data reduction and analysis are presented in this chapter as well. Chapters 3, 4 and 5 demonstrate the scientific interpretations of the multi-wavelength datasets obtained by GROND and *Swift*/XRT for the afterglows of GRBs 080413B, 091127 and 091029, and show the increasing difficulties of the fireball shock scenario to model the well-sampled multi-color afterglows observed with the latest generation of GRB instruments. While GRB 080413B can be explained by assuming two co-aligned jets, GRB 091127 can only be explained if ϵ_B, hitherto always assumed to be constant, evolves in time. For GRB 091029, finally, a self-consistent explanation could not be found.

The broad-band light curve of the afterglow of GRB 080413B is well fitted with an on-axis two-component jet model. The narrow ultra-relativistic jet is responsible for the initial decay, while the rise of the moderately relativistic wider jet near its deceleration time is the cause of the rebrightening of the light curve. The later evolution of the optical/NIR light curve is then dominated by the wide component, the signature of which is almost negligible at X-ray wavelengths. The opening angles of the narrow and wide outflow were derived to be $\theta_n \sim 1.7°$ and $\theta_w \sim 9°$, and Lorentz factors to be $\Gamma_n > 188$ and $\Gamma_w \sim 18.5$.

Both the multi-color light curve and the broad-band SED of the afterglow of GRB 091127 show evidence of a cooling break moving from high to lower energies. The early light curve is well described by a broken power-law, where the initial decay in the optical/NIR wavelength range is considerably flatter than at X-rays. Detailed fitting of the time-resolved SED shows that the break is very smooth with a sharpness index of 2.2 ± 0.2, and evolves towards lower frequencies as a power-law with index -1.23 ± 0.06. This evolution is not consistent with the predictions of the standard model, wherein $\nu_c \propto t^{-0.5}$ is expected. A possible explanation for the observed behavior is a time dependence of the microphysical parameters, in particular the fraction of the total energy in the magnetic field ϵ_B.

The optical/NIR and the X-ray light curves of the afterglow of GRB 091029 are seemingly nearly totally decoupled. To explain this decoupling, a two-component outflow is proposed. Several models are tested and only the model with components in two different stages of the spectral evolution can explain both the decoupled light curves with asynchronous peaks and the peculiar SED evolution. However, this model has so many unknown free parameters that we are unable to reliably confirm or disprove its validity, making the afterglow of GRB 091029 difficult to explain in the frame of the fireball shock model.

Zusammenfassung

Gammastrahleblitze (Englisch: Gamma-Ray Burst, GRBs) sind die am kompaktesten und hellsten elektromagnetischen Explosionen des Universums. Sie strahlen große Mengen an Energie ab, in der Größenordnung von $\sim 10^{51}$ erg, auf sehr kurzen Zeitskalen zwischen 10^{-3} und 10^3 Sekunden. Das allgemein akzeptierte Modell ist das Feuerball-Shock Modell, bei dem ein Materieausfluß zu einem eng kollimierten Strahl (English: Jet) gebündelt wird und dabei ultra-relativistische Geschwindigkeiten ($\Gamma > 100$) erreicht. Die Wechselwirkung von Materiaschalen des Feuerballs untereinander, die sich mit verschiedenen Geschwindigkeiten fortbewegen, sogenannte "interne Schockfronten", sind für den anfänglichen γ-Strahlungsausbruch verantwortlich, während die Kollision der Schalen mit dem umgebenden Medium, die sogenannten "externen Schockfronten", das Nachglühen (Englisch: Afterglow) erzeugen, welches über Tage oder sogar Monate hinweg über einen weiten Wellenlängenbereich von Radio- über optische bis hin zu Röntgenstrahlung beobachtet werden kann. Die Strahlung des Afterglows lässt sich mit nicht-thermischer Synchrotonstrahlung erklären.

Diese Dissertation beschreibt die wissenschaftliche Analyse von GRB-Afterglow Daten, die mit dem Gamma-Ray burst Optical/Near-infrared Detector (GROND) Instrument gewonnen worden sind, eine Sieben-Band Kamera mit vier optischen Detektoren und dreien im nahen Infrarot (NIR), die einen Wellenlängenbereich von $360 - 2300$ nm abdecken. Ihre einmalige Fähigkeit, in all diesem Bändern zugleich zu beobachten, sowie eine schnelle Reaktionszeit, präzise Photometrie und eine hohe zeitliche Auflösung erlauben es uns, die Lichtkurven und spektralen Energieverteilungen (Englisch: Spectral Energy Distribution, SED) von GRB Afterglows in bisher ungeahntem Detail zu studieren.

Diese Dissertation ist wie folgt strukturiert: Kapitel 1 legt die grundsätzliche Beschreibung von GRBs dar, zusammen mit einer kurzen Übersicht des beobachterischen sowie des theoretischen Fortschritts in diesem Gebiet. Daraufhin wird das Standard-Feuerball-Szenarium sowie seine vielfältigen Erweiterungen beschrieben. Kapitel 2 dreht sich um Details zur Instrumentierung des *Swift*-Satelliten sowie der GROND-Kamera. Die Beobachtungen mit GROND im Modus Rascher Reaktion werden beschrieben, sowie die automatische Beobachtungsauslösung und die Software zur Datenreduktion. Die Datenaufbereitung sowie die Software-Werkzeuge, die zur Datenreduktion und -analyse verwendet werden, werden in diesem Kapitel ebenso beschrieben. Die Kapitel 3, 4 und 5 gehen dann auf die wissenschaftliche Interpretation der Multi-Wellenlängen Datensätze, die durch GROND sowie *Swift* XRT für die Afterglows der GRBs 080413B, 091127 and 091029 gewonnen worden sind, ein, und weisen auf die immer größeren Schwierigkeiten des Standard-Feuerball-Szenariums hin, die datenreichen Multi-Farben-Afterglows erfolgreich zu modellieren, die mit der jüngsten Generation von GRB-Detektoren gewonnen werden. Während GRB 080413B erklärt werden kann, indem man zwei aneinander ausgerichtete Jets annimmt, kann GRB 091127 nur mittels einer Evolution von ϵ_B, welches bisher als eine konstante Größe angenommen worden war, interpretiert werden. Für GRB 091029 schließlich konnte keine intern konsistente Erklärung gefunden werden.

Die Breitband-Lichtkurve des Afterglows von GRB 080413B kann gut mit einem achsennahen Zwei-Komponenten-Jet-Modell angepaßt werden. Der schmale ultrarelativistische Jet ist für den anfänglichen Helligkeitsabfall verantwortlich, während im Anstieg des moderat relativistischen, breiteren Jets um die Zeit seiner Abbremsung herum der Grund für das Wiederaufhellen der Lichtkurve zu finden ist. Die spätere Entwicklung der optischen/NIR Lichtkurve wird dann von der breiteren Komponente dominiert, welche im Wellenlängenbereich der Röntgenstrahlung fast keine Signatur aufweist. Die Öffnungswinkel für den schmalen und den breiten Ausfluß wurden zu $\theta_n \sim 1.7°$ und $\theta_w \sim 9°$, sowie die Lorentzfaktoren zu $\Gamma_n > 188$ und $\Gamma_w \sim 18.5$ bestimmt.

Sowohl die Multi-Farben-Lichtkurve wie auch die Breitband-SED des Afterglows von GRB 091127 enthalten Hinweise auf eine Kühlungsknickstelle, die sich von hohen zu niedrigeren Energien bewegt. Die frühe Lichtkurve kann gut durch ein gebrochenes Potenzgesetz beschrieben werden, wobei der anfängliche Helligkeitsabfall im optischen/NIR Wellenlängenbereich wesentlich flacher abläuft als im Röntgenbereich. Detailliertes Fitten der zeitaufgelösten SED offenbart, dass die Knickstelle sehr glatt ist, mit einem Schärfe-Index von nur 2.2 ± 0.2, und dass sie sich zu niedrigeren Frequenzen hin entwickelt, wobei sie einem Potenzgesetz mit Index -1.23 ± 0.06 folgt. Diese Evolution stimmt nicht mit den Vorhersagen des Standardmodells überein, für die man $\nu_c \propto t^{-0.5}$ erwarten würde. Eine mögliche Erklärung für das beobachtete Verhalten wäre eine Zeitabhängigkeit der mikrophysikalischen Paramter, insbesondere des Anteils der Gesamtenergie, die im magnetischen Feld gespeichert ist, ϵ_B.

Die optischen/NIR sowie Röntgenlichtkurven des Afterglows von GRB 091029 sind anscheinend fast komplett entkoppelt. Um diese Entkopplung zu erklären wird ein Ausfluß, der aus zwei Komponenten besteht, vorgeschlagen. Mehrere Modelle werden getestet, und nur dasjenige, welches Komponenten beinhaltet, die sich in zwei unterschiedlichen Phasen der spektralen Entwicklung befinden, vermag sowohl die entkoppelten Lichtkurven mit asynchronen Maxima sowie die seltsame Entwicklung der SED zu erklären. Dieses Modell hat jedoch so viele unbekannte freie Parameter, dass wir dessen Gültigkeit weder mit Zuverlässigkeit bestätigen noch widerlegen können, wodurch der Afterglow von GRB 091029 im Rahmen des Feuerball-Schock-Modells nur schwierig zu erklären ist.

Contents

Chapter 1

Introduction

1.1 Introduction to GRBs

The scientists got a first hint about the existence of gamma-ray bursts (GRBs) in the early seventies, when the data from the Vela satellites were published (Klebesadel et al., 1973) and showed that these military satellites monitoring for compliance with the nuclear test ban treaty were detecting these extraterrestrial events since the late sixties. Their nature and origin remained a mystery for two decades until the launch of the Compton Gamma-Ray Observatory (CGRO) in 1991 with its Burst and Transient Experiment (BATSE) which showed that GRBs are isotropically distributed in the sky, giving significant suggestion of their cosmological origin (Meegan et al., 1992). This theory was confirmed in 1997 with the launch of the Italian-Dutch satellite Beppo-SAX, which detected and localized GRBs in the X-ray wavelengths (Costa et al., 1997) and enabled ground-based follow-up observations (van Paradijs et al., 1997) including redshift measurements that confirmed the cosmological distances of these events (Metzger et al., 1997; Kulkarni et al., 1998).

The cosmological origin of GRBs implies an extreme luminosity of GRB sources, they release $\sim 10^{51} - 10^{53}$ erg or even more over a time of just few seconds (Piran, 1999), making them the most concentrated and brightest electromagnetic explosions in the Universe. The BATSE satellite recorded over 2700 GRBs over the 9-year CGRO mission at an average rate of 1 burst per day, observing non-thermal spectra having a smoothly-joining broken power-law shape with the break at $\sim 0.1 - 1$ MeV (Band et al., 1993). The durations of GRBs range from 10^{-3} to 10^{3} seconds following a bi-modal distribution of spectrally harder "short" GRBs with duration $t_\gamma \lesssim 2$ s and "long" GRBs with duration $t_\gamma \gtrsim 2$ s (Kouveliotou et al., 1993). Afterglows of short GRBs were only detected after the launch of the *Swift* satellite in 2004 (Gehrels et al., 2004), which started a third epoch of GRB discoveries after BATSE and Beppo-SAX. Thanks to its precise localization of GRBs in gamma-ray, X-ray and UV wavelengths, follow-up observations were possible starting minutes after the burst trigger. These revealed early X-ray behavior, such as the transition from the prompt emission to the later long-lasting afterglow, as well as the diverse properties of the optical light curves
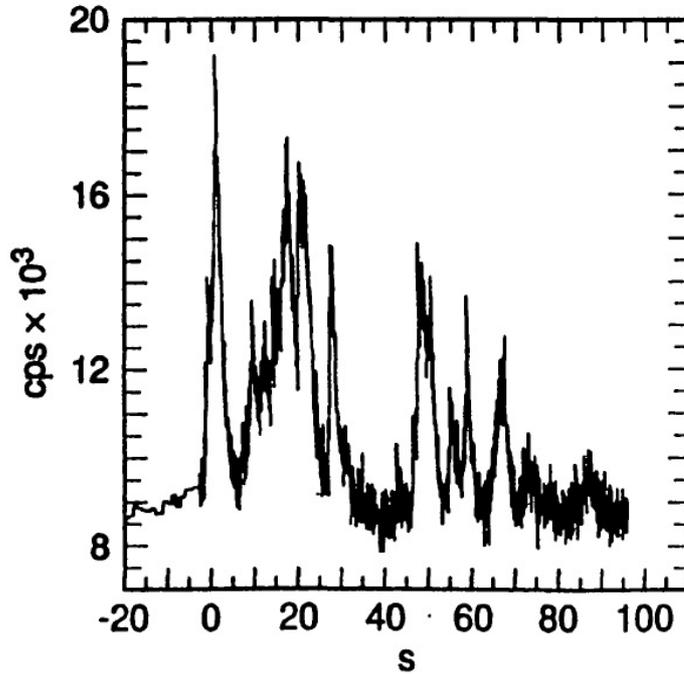
Figure 1.1 Typical GRB light curve observed with BATSE showing photon count rate in the 50-300 keV band versus time. From Fishman and Meegan (1995).

like the ones discussed in this thesis.

While the source of GRBs was unknown for a long time due to their very short duration and difficult localization, the observational evidence now points towards a catastrophic energy release of a dying star (van Paradijs et al., 2000). Long GRBs are generally associated with a core collapse of a massive star into a black hole (Woosley, 1993; Paczynski, 1998; Fryer et al., 1999; MacFadyen and Woosley, 1999). This collapsar theory is supported by a rising number of observed supernovae (SNe) events associated with GRBs (e.g. Galama et al., 1998; Stanek et al., 2003; Hjorth et al., 2003; Campana et al., 2006; Malesani et al., 2004). Short GRBs on the other hand are believed to be mergers of neutron star binaries or neutron star and black hole binaries (Paczynski, 1986; Goodman, 1986; Eichler et al., 1989; Meszaros and Rees, 1992, 1997b). These binaries would lose angular momentum by emitting gravitational waves and would undergo a merger (Mészáros, 2006). In both the collapsar and merger scenarios, the result of the explosion is a black hole. The gravitational energy released in the first few milliseconds is then further augmented on timescales of seconds to hundreds of seconds by the accretion of the surrounding gas onto this black hole (Mészáros, 2006).

2
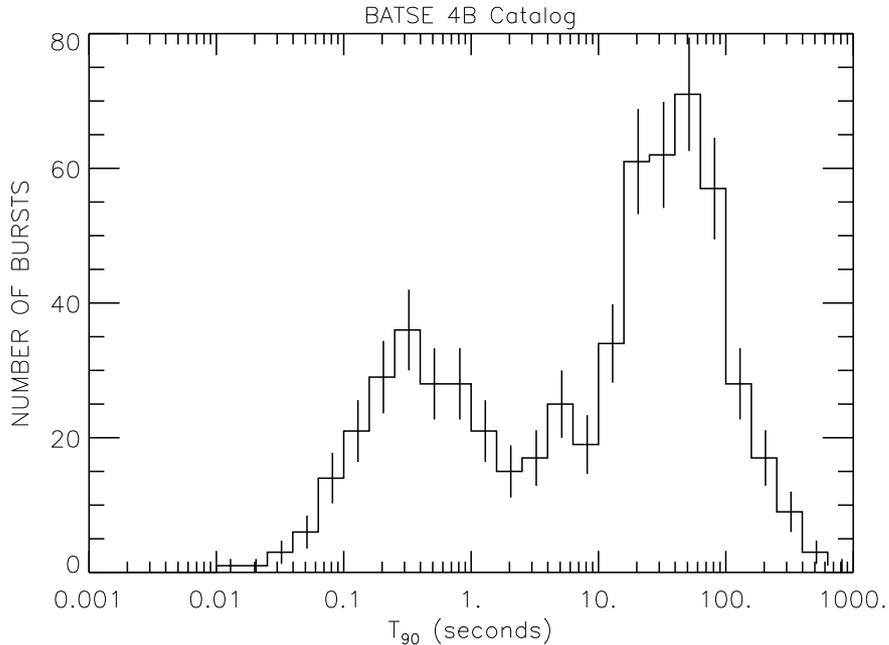
Figure 1.2 Bimodal distribution of BATSE bursts showing two types of GRBs based on their duration, short bursts with $T_{90} < 2$ s and long bursts with $T_{90} > 2$ s, where the duration parameter T_{90} is the time over which a burst emits from 5% of its total measured counts to 95%. From Paciesas et al. (1999).

1.2 Standard fireball scenario

Most of the gravitational energy is believed to be converted into gravitational waves (in case of short bursts) and thermal neutrinos, while significantly smaller fraction ($\lesssim 1\%$) is released in a form of a fireball consisting of $e^{\pm}$, γ-ray photons and baryons, the result of the very intense and compact explosion (Cavallo and Rees, 1978; Paczyn-ski, 1986; Goodman, 1986). Another result of high energy and short timescale is a relativistic expansion of such fireball if the compact region where the fireball forms contains relatively few baryons (Shemi and Piran, 1990; Paczynski, 1990). A low baryonic loading is required for the fireball to achieve ultra-relativistic speeds as the initial radiation pressure is converted into kinetic speed. The more baryons need to be accelerated the lesser is the bulk speed of the ejecta. A low contamination of the fireball with baryons results in the whole emitting region moving towards the observer with high Lorentz factor ($\Gamma \gtrsim 100$). The kinetic energy of such flow is then re-converted into the radiation via "internal shocks" when the fireball becomes optically thin (Rees and Meszaros, 1992; Meszaros and Rees, 1993b; Meszaros et al., 1993). Such shocks arise when the faster shell catches up with the shell with lower Lorentz factor created earlier (Sari and Piran, 1995; Rees and Meszaros, 1994). These shocks raise the entropy by chaotic electric and magnetic fields and accelerate particles to ultra-relativistic energies

3
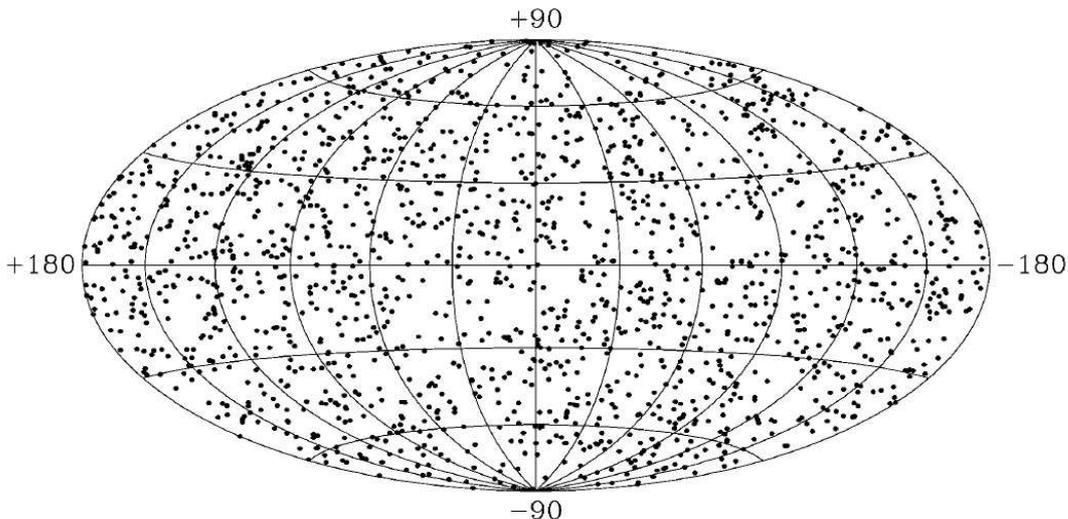
Figure 1.3 Sky distribution of the 1637 BATSE bursts showing their isotropic distribution. From Paciesas et al. (1999).

(Blandford and Eichler, 1987). The relativistic electrons then produce a non-thermal radiation via the synchrotron emission, i.e. emission from relativistic electrons gyrating in a magnetic field, and the inverse Compton scattering, where the photon gains energy upon interaction with matter.

After the shells interact with each other and emit the prompt gamma-ray emission (i.e. GRB itself), the fireball propagates into the ambient medium, where it produces a blast wave. This "external shock" is responsible for the afterglow emission detected in all wavelengths below gamma-rays (Fig. 1.4). The external medium in the standard scenario is either an interstellar matter (ISM) or a stellar wind which the progenitor star ejected prior to the collapse. As the external shock ploughs into the ambient medium, it is heated into extreme temperatures. The fraction of electrons at the shocks are then Fermi accelerated to relativistic velocities with power-law distribution of energies $N(\gamma_e) \propto \gamma_e^{-p}$ and the total energy of electrons is a fraction ϵ_e of the total energy in the shocked region. The magnetic field behind the external shock can increase thanks to the turbulent dynamo effects (Meszaros and Rees, 1993b,a) and the resulting magnetic field can be characterized by the parameter ϵ_B, which represents fraction of the energy density in the magnetic field relative to the internal energy (Mészáros, 2006). Relativistic electrons moving in the magnetic field emit non-thermal synchrotron radiation, characteristic for GRB afterglows. These microphysical parameters p, ϵ_e and ϵ_B are considered constant for each GRB and fitted from the data (Wijers and Galama, 1999; Panaitescu and Kumar, 2001, 2002; Harrison et al., 2001; Yost et al., 2003). These parameters and the lack of theoretical constraints of their values show our problems with tackling the standard fireball scenario.
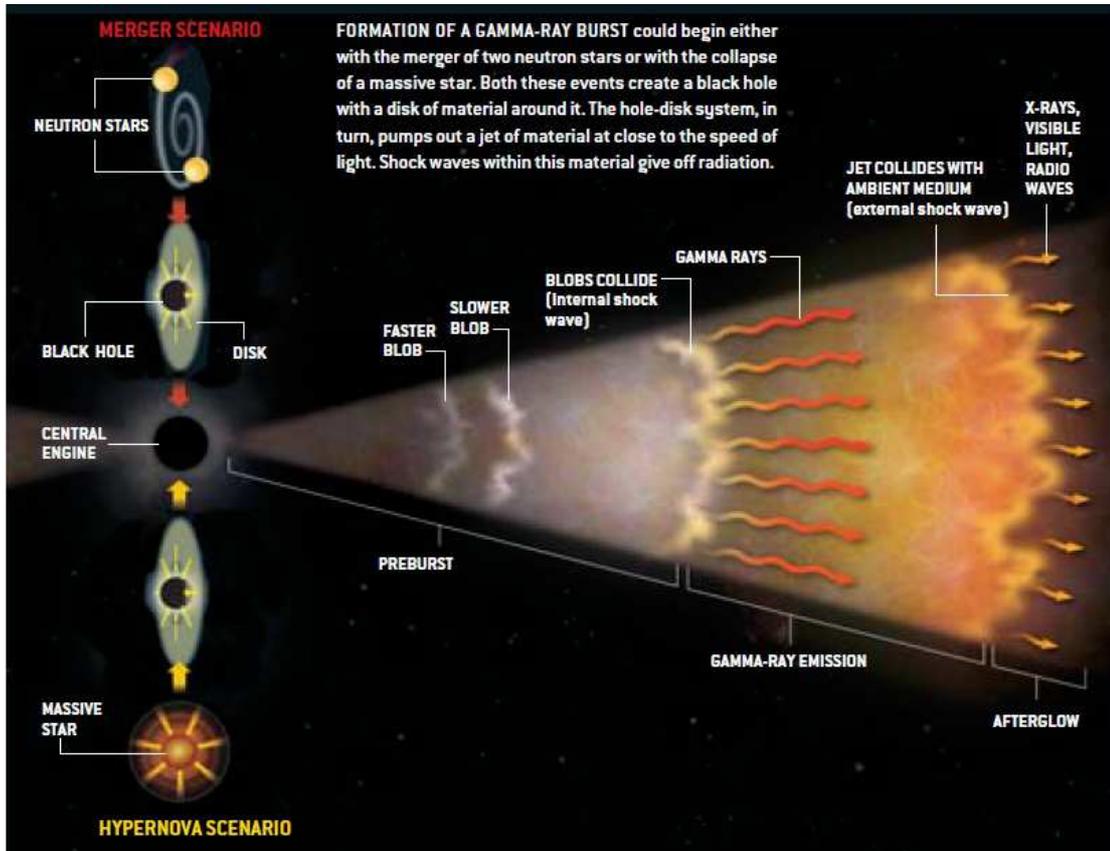
Figure 1.4 Schematics of the fireball shock model showing two types of progenitors, internal shocks responsible for the gamma-ray emission and the external shock responsible for the multi-wavelength GRB afterglow. From Scientific American, December 2002.

The spectra of GRB afterglows consist of four power-law segments connected at three frequencies typical for the synchrotron emission (Fig. 1.5). The lowest break frequency ν_a represents synchrotron self-absorption, below which the afterglow is optically thick and which causes a steep cut-off of the spectrum at low frequencies (Katz and Piran, 1997; Waxman, 1997). The other two break frequencies are the injection frequency ν_m, corresponding to the minimum energy acquired by the accelerated electrons, and the cooling frequency ν_c, above which the electrons cool (i.e. lose energy by radiation) more rapidly. Depending on which of the last two frequencies is higher, there are two types of the spectra (Sari et al., 1998). The fast cooling case ($\nu_m > \nu_c$) shortly after GRB when the external shock immensely accelerates the electrons and their minimum

Lorentz factor is high. In this case the spectrum is

$$F_\nu = F_{\nu,\max} \begin{cases} (\nu_a/\nu_c)^{1/3}(\nu/\nu_a)^2 & \nu < \nu_a \\ (\nu/\nu_c)^{1/3} & \nu_a \leq \nu < \nu_c \\ (\nu/\nu_c)^{-1/2} & \nu_c \leq \nu < \nu_m \\ (\nu_m/\nu_c)^{-1/2}(\nu/\nu_m)^{-p/2} & \nu_m \leq \nu. \end{cases} \qquad (1.1)$$

At later times when the external medium slows down the fireball ejecta, the minimum Lorentz factor of the electrons is much lower and the afterglow is in the slow cooling case ($\nu_m < \nu_c$). In this regime the spectrum is

$$F_\nu = F_{\nu,\max} \begin{cases} (\nu_a/\nu_m)^{1/3}(\nu/\nu_a)^2 & \nu < \nu_a \\ (\nu/\nu_m)^{1/3} & \nu_a \leq \nu < \nu_m \\ (\nu/\nu_n)^{-(p-1)/2} & \nu_m \leq \nu < \nu_c \\ (\nu_c/\nu_m)^{-(p-1)/2}(\nu/\nu_c)^{-p/2} & \nu_c \leq \nu \end{cases} \qquad (1.2)$$

where $F_{\nu,\max}$ is the flux density at the peak frequency of the GRB afterglow spectrum (ν_c in the fast cooling case and ν_m in the slow cooling case).

As the fireball ejecta sweeps up more and more external matter, the bolometric luminosity of the external shock increases as $L \propto t^2$ (Mészáros, 2006) while the Lorentz factor decreases with radius r or the observer's time t as (Zhang and Mészáros, 2004)

$$\Gamma \propto r^{-3} \propto t^{-3/7}, r \propto t^{1/7}$$
$$\Gamma \propto r^{-3/2} \propto t^{-3/8}, r \propto t^{1/4}, \qquad (1.3)$$

where the first relation is valid for the evolution of a fully radiative fireball. In this case the momentum of the fireball stays constant while the radiation is responsible for the energy loss (Meszaros et al., 1998; Panaitescu and Meszaros, 1998; Cohen et al., 1998). This fully radiative case is only possible in the fast-cooling regime. The second relation is valid for the evolution of a fully adiabatic fireball, in which the energy stays constant. This case is valid at the later times (∼hours) for all the afterglows and in many afterglows even at earlier times (Zhang and Mészáros, 2004). The fireball is probably not strictly fully adiabatic or fully radiative and the best approximation is a quasi-adiabatic fireball evolution with small radiative correction (Sari, 1997).

The typical synchrotron frequencies ν_m, ν_c, ν_a and the normalization $F_{\nu,\max}$ in Eq. 1.1 and 1.2 evolve with time as power-laws. Assuming a fully adiabatic evolution and $p > 2$ (relations for $p < 2$ are derived in Chapter 4), these time dependencies can be quantified using the microphysics parameters $\epsilon_e, \epsilon_B, p$ and the burst properties as (Sari
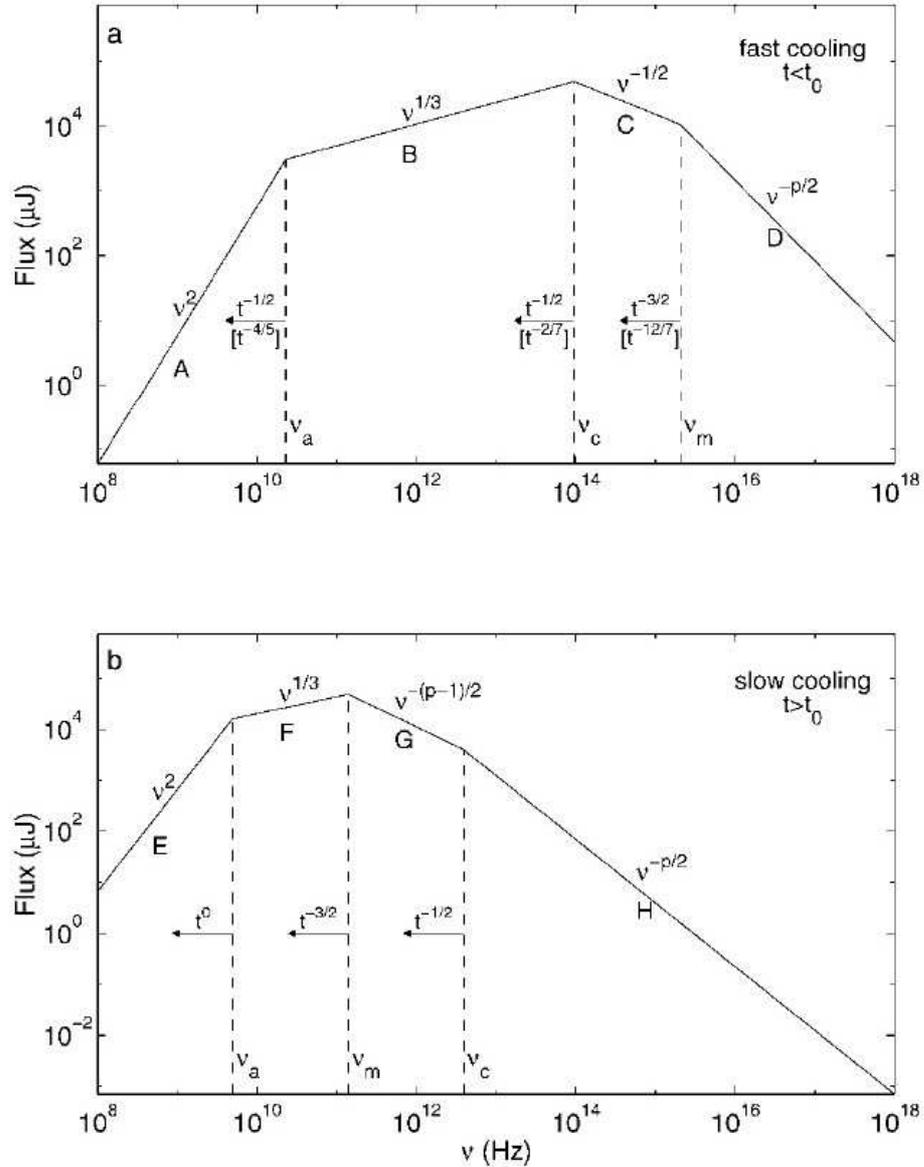
Figure 1.5 Synchrotron spectrum of the relativistic external shock. The upper image shows the case of the fast cooling, where $\nu_c < \nu_m$. The spectrum consists of four power-laws connected at three typical synchrotron frequencies, which decrease with time as indicated. The scalings in square brackets correspond to fully radiative evolution, the other scalings are valid for fully adiabatic evolution. The lower image shows the slow cooling case, where $\nu_c > \nu_m$ and the evolution is always adiabatic. From Sari et al. (1998).

7

et al., 1998; Zhang and Mészáros, 2004)

$$\nu_a \propto (1+z)^{-1} E_{\text{iso}}^{1/5} \epsilon_B^{1/5} \epsilon_e^{-1} n^{3/5},$$

$$\nu_c \propto (1+z)^{-1/2} E_{\text{iso}}^{-1/2} \epsilon_B^{-3/2} n^{-1} t^{-1/2},$$

$$\nu_m \propto (1+z)^{1/2} E_{\text{iso}}^{1/2} \epsilon_B^{1/2} \epsilon_e^2 t^{-3/2},$$ (1.4)

$$F_{\nu,\text{max}} \propto (1+z) E_{\text{iso}} \epsilon_B^{1/2} n^{1/2} D_L^{-2},$$

where t is the time since the GRB trigger, E_{iso} is the isotropic energy of the GRB, n is the density profile of the circum-burst medium and D_L is the luminosity distance of the GRB. Although the normalization of the parameters in Eq. 1.4 differ with the chosen value of p for various works, the scalings on them are equal to those in Eq. 1.4. Using these relations and fixing the observation frequency in Eq. 1.1 and 1.2, the temporal evolution of the afterglow light curves can be calculated. However, in order for the fireball model to be consistent with the observed afterglow light curves, some assumptions of the simplest model must be abandoned.

The most unrealistic assumption is the isotropic emission of GRBs. Given that bursts are detected at very large redshifts, the measured fluence (time-integrated flux) in gamma-ray wavelengths would imply a large spread of total energies from $\sim 10^{51}$ erg to $\sim 10^{54}$ erg (Mészáros, 2002), the latter value being a thousand times larger than the total kinetic energies associated with core-collapse supernovae. To alleviate these energy requirements, an emission in a relativistic concentrated flow has been proposed (Rhoads, 1997, 1999). When accounting for this "jet", the inferred spread in the total gamma-ray energy is then reduced by Γ to one order of magnitude around $\sim 10^{51}$ erg, showing that GRBs may have a standard energy reservoir (Frail et al., 2000; Bloom et al., 2002; Rossi et al., 2002; Zhang and Mészáros, 2002a). Such total energies are comparable to those released isotropically over weeks in the optical range after the explosions of the supernovae, although emission of GRBs is mainly in the gamma-ray range, very short and concentrated in jets. Therefore the brightness of the GRB for an observer aligned with the jet is much more intense.

Jets are strongly supported by the observational data, which show a break in the afterglow light curves followed by a steepening of the decay (e.g., Kulkarni et al., 1999; Fruchter et al., 1999; Castro-Tirado et al., 1999). This is caused by the relativistic principle that the emission of an object moving with the Lorentz factor Γ is beamed into a cone with opening angle $1/\Gamma$. Initially, when the object moves ultra-relativistically, the observer only receives signal from within the light cone and has no information from the outside of it. As the jet slows down, the light cone becomes wider and the observer receives emission from regions of the jet, where earlier the observer was outside of those light cones. The whole jet is visible to the observer when $1/\Gamma = \theta$, where θ is the opening angle of the jet itself. As the external shock slows down and loses its energy, the afterglow light curve decays as a power-law in time. However, this light curve decay is influenced by the fact that the observer sees an increasing amount of light from the slowing jet. When $1/\Gamma = \theta$, the observer sees the complete jet, there is
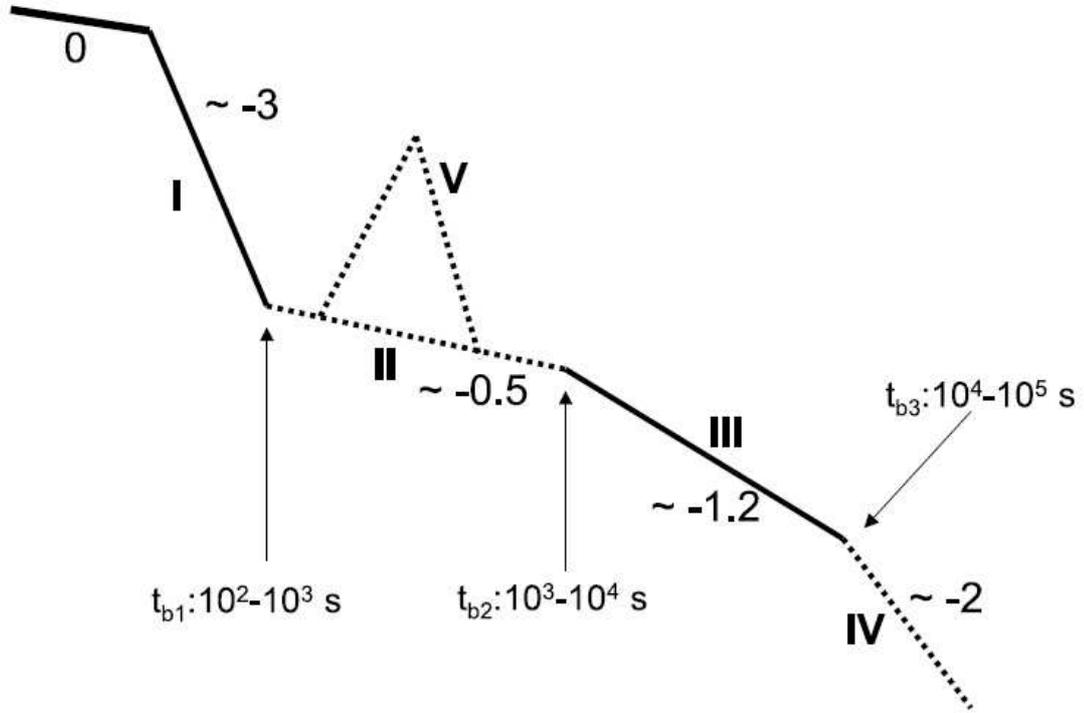
Figure 1.6 Canonical X-ray light curve of the GRB afterglow. The segment 0 denotes the prompt emission, segments I-IV represent the afterglow emission. Segment I is a tail of the GRB emission, i.e. transition from the prompt phase to the afterglow. Segment II is due to continuous energy injection by the central engine. Segment III is the normal spherical decay of the afterglow by the decelerating fireball. Segment IV is the decay after the jet break and segment V represents a random flare. From Zhang et al. (2006).

no more emission to compensate for the energy loss and therefore a break in the light curve occurs, followed by the steepening of the decay. This "jet break" is demonstrated in the canonical X-ray afterglow light curve in Fig. 1.6 as a transition from segments III to IV.

While the simplest jet model assumes a homogeneous outflow with no emission outside of θ (Rhoads, 1999; Woods and Loeb, 1999), there are studies proposing the kinetic energy in the jet per solid angle parametrized for example as a Gaussian (Zhang and Mészáros, 2002a), a power-law (Meszaros et al., 1998), or as two components with different Lorentz factors (Peng et al., 2005). The shape of the resulting light curve then depends on the jet structure (Fig. 1.7) and the observers viewing angle (Rossi et al., 2002). The Lorentz factor is dependent on the distance to the symmetry axis of the jet (Kumar and Granot, 2003) and therefore this geometric offset between observers line of sight and the jets symmetry axis has a distinct signature in the afterglow light curve (Granot and Kumar, 2003). In the case of an observer located off-axis to the symmetry
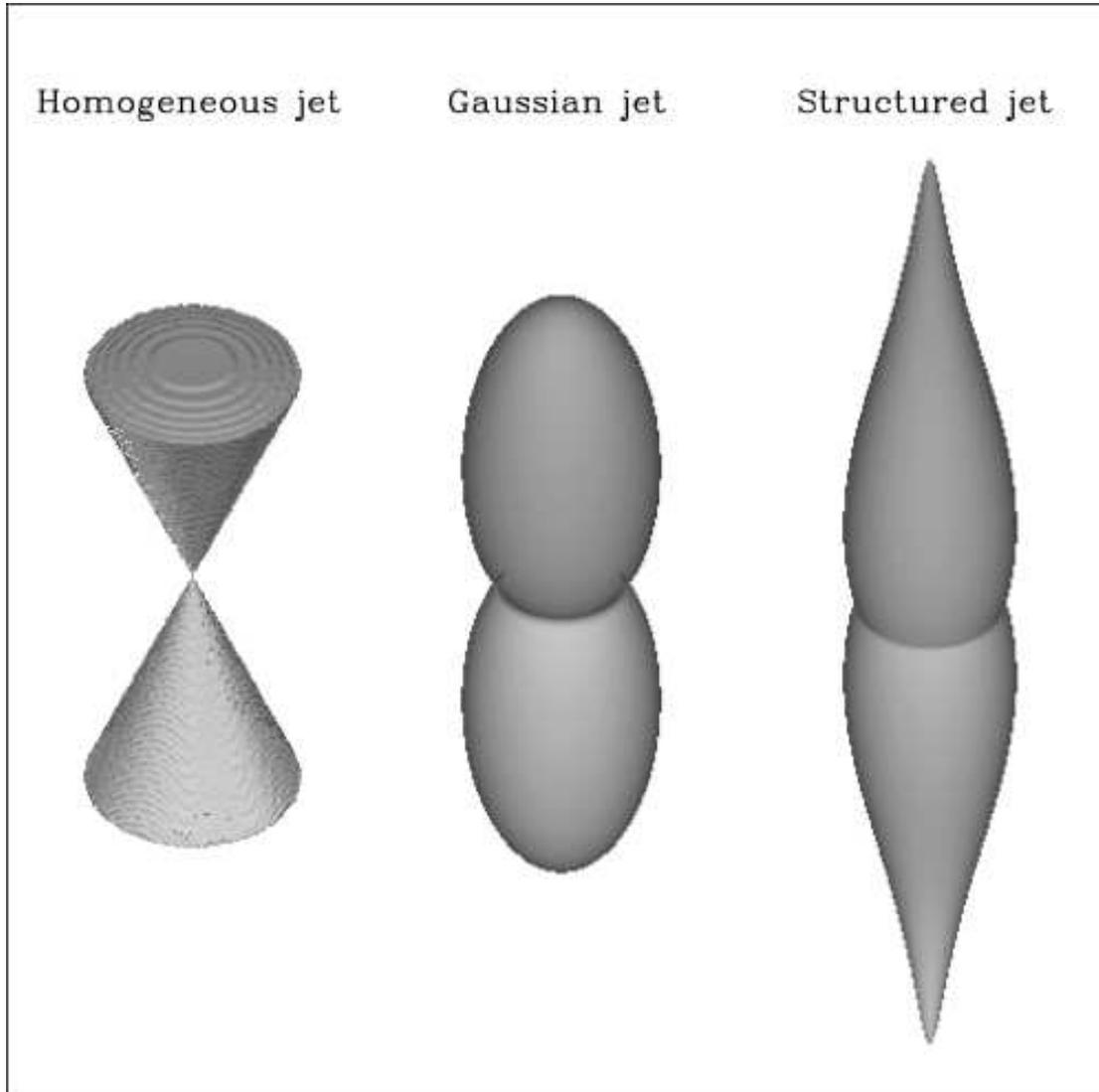
Figure 1.7 Cartoon of different jet configurations. The figure shows the energy per unit solid angle of the jets scaled logarithmically. The scale is different for each jet, it has been chosen in order to visually emphasize the characteristics of each configuration. From Rossi et al. (2004).

axis of the jet, the early optical afterglow light curve will have a rising phase (Panaitescu et al., 1998; Granot et al., 2002). The temporal index of the rise then depends on the off-axis angle and the jet structure. The larger is the distance of the observer from the central emitting cone or the faster the energy per solid angle decreases outside of the jet, the shallower is the observed rise (Panaitescu and Vestrand, 2008).

The simplest afterglow model is based on an assumption that the ambient density

around the GRB is constant, i.e. that the density profile n does not change with the radial distance r from the burst. However, a well discussed option is that the external medium is a stellar wind from the massive star progenitor. In this wind scenario, the density profile of the external medium decreases with the distance from the burst as $n \propto r^{-2}$ (Chevalier and Li, 1999). This density profile changes the fireball dynamics as (Zhang and Mészáros, 2004)

$$\Gamma \propto r^{-1/2} \propto t^{-1/4}, r \propto t^{1/2} \qquad (1.5)$$

and the light curves and spectra evolution are modified accordingly (Fig. 1.8). Although the wind-like medium would be expected around massive star progenitors, most of the GRBs are consistent with the constant density ISM (e.g., Panaitescu and Kumar, 2001; Frail et al., 2001; Panaitescu and Kumar, 2002). However, a not negligible number of GRBs are well modelled by the wind environment (e.g., Chevalier and Li, 2000; Li and Chevalier, 2001, 2003). A convenient way to test various model regimes and ambient density profiles is to obtain simultaneous measurements of the temporal and the spectral indices. Adopting a convention that the flux density of the GRB afterglow can be described as $F_\nu(t) \propto t^{-\alpha} \nu^{-\beta}$, where α is the temporal and β the spectral index, the "closure relations" between α and β for various scenarios are shown in Fig. 1.8.

This more complex model with beaming and two types of ambient density profiles then worked surprisingly well with a majority of the observed GRB afterglows. It is only with the arrival of the most modern telescopes, as the ones discussed later in this section, that even this advanced model is not complex enough to model the light curves obtained by the detectors with high temporal resolution, precise photometry and multi-wavelength capabilities. Several additions to the standard fireball model have been proposed in order to explain bumps, rebrightenings and flares in the light curves and non-standard behavior of the spectra of many GRBs observed since the launch of the *Swift* satellite.

1.2.1 Reverse shock emission

Due to the imprecise localization of GRBs, slow slewing of instruments and long time for the alert to reach follow-up telescopes, early observations of the afterglow light curves have started hours after the burst trigger. At that time, the fireball blastwave has been decelerated and the afterglow behavior is determined by the total energy per solid angle in the fireball and the characteristics of the ambient medium (Zhang and Mészáros, 2004). With the growing number of optical robotic telescopes around the world and the launch of Beppo-SAX, the time between the trigger and the optical follow-up decreased significantly and revealed new early light curve features, like the initial rise of the optical light curve in the first four bursts, whose afterglow has been observed within 10 minutes of the trigger: GRB 990123 (Akerlof et al., 1999), GRB 021004 (Fox et al., 2003b), GRB 021211 (Fox et al., 2003a; Li et al., 2003) and GRB 030418 (Rykoff et al., 2004; Zhang and Kobayashi, 2005). One of the proposed explanation for the early optical flashes in optical afterglows is the emission from a reverse shock (Sari and

Closure Relations

		β	a No Energy Injection $\alpha(\beta)$ $(p > 2)$	b $\alpha(\beta)$ $(1 < p < 2)$	c Energy Injection $\alpha(\beta)$ $(p > 2)$
			ISM, Slow Cooling		
1	$\nu_m < \nu < \nu_c$	$\frac{p-1}{2}$	$\alpha = \frac{3\beta}{2}$	$\alpha = \frac{3(2\beta+3)}{16}$	$\alpha = (q-1) + \frac{(2+q)\beta}{2}$
2	$\nu > \nu_c$	$\frac{p}{2}$	$\alpha = \frac{3\beta-1}{2}$	$\alpha = \frac{3\beta+5}{8}$	$\alpha = \frac{q-2}{2} + \frac{(2+q)\beta}{2}$
			ISM, Fast Cooling		
3	$\nu_c < \nu < \nu_m$	$\frac{1}{2}$	$\alpha = \frac{\beta}{2}$	$\alpha = \frac{\beta}{2}$	$\alpha = (q-1) + \frac{(2-q)\beta}{2}$
4	$\nu > \nu_m$	$\frac{p}{2}$	$\alpha = \frac{3\beta-1}{2}$	$\alpha = \frac{3\beta+5}{8}$	$\alpha = \frac{q-2}{2} + \frac{(2+q)\beta}{2}$
			Wind, Slow Cooling		
5	$\nu_m < \nu < \nu_c$	$\frac{p-1}{2}$	$\alpha = \frac{3\beta+1}{2}$	$\alpha = \frac{2\beta+9}{8}$	$\alpha = \frac{q}{2} + \frac{(2+q)\beta}{2}$
6	$\nu > \nu_c$	$\frac{p}{2}$	$\alpha = \frac{3\beta-1}{2}$	$\alpha = \frac{\beta+3}{4}$	$\alpha = \frac{q-2}{2} + \frac{(2+q)\beta}{2}$
			Wind, Fast Cooling		
7	$\nu_c < \nu < \nu_m$	$\frac{1}{2}$	$\alpha = \frac{1-\beta}{2}$	$\alpha = \frac{1-\beta}{2}$	$\alpha = \frac{q}{2} - \frac{(2-q)\beta}{2}$
8	$\nu > \nu_m$	$\frac{p}{2}$	$\alpha = \frac{3\beta-1}{2}$	$\alpha = \frac{\beta+3}{4}$	$\alpha = \frac{q-2}{2} + \frac{(2+q)\beta}{2}$
			Uniform Jet (spreading), Slow Cooling		
9	$\nu_m < \nu < \nu_c$	$\frac{p-1}{2}$	$\alpha = 2\beta + 1$	$\alpha = \frac{2\beta+7}{4}$	$\alpha = 2\beta + 1 - \frac{2(1-q)(\beta+2)}{3}$
10	$\nu > \nu_c$	$\frac{p}{2}$	$\alpha = 2\beta$	$\alpha = \frac{\beta+3}{2}$	$\alpha = 2\beta - \frac{2(1-q)(\beta+1)}{3}$
			ISM, Uniform Jet (nonspreading)		
11	$\nu_m < \nu < \nu_c$	$\frac{p-1}{2}$	$\alpha = \frac{6\beta+3}{4}$	$\alpha = \frac{6\beta+21}{16}$	$\alpha = \frac{6\beta+3}{4} - \frac{(1-q)(2\beta+5)}{4}$
12	$\nu > \nu_c$	$\frac{p}{2}$	$\alpha = \frac{6\beta+1}{4}$	$\alpha = \frac{3\beta+11}{8}$	$\alpha = \frac{6\beta+1}{4} - \frac{(1-q)(2\beta+3)}{4}$
			Wind, Uniform Jet (nonspreading)		
13	$\nu_m < \nu < \nu_c$	$\frac{p-1}{2}$	$\alpha = \frac{3\beta+2}{2}$	$\alpha = \frac{2\beta+13}{8}$	$\alpha = \frac{3\beta+2}{2} - \frac{(1-q)(\beta+2)}{2}$
14	$\nu > \nu_c$	$\frac{p}{2}$	$\alpha = \frac{3\beta}{2}$	$\alpha = \frac{\beta+5}{4}$	$\alpha = \frac{3\beta}{2} - \frac{(1-q)(\beta+2)}{2}$
			ISM, Structured Jet		
15	$\nu_m < \nu < \nu_c$	$\frac{p-1}{2}$	$\alpha = \frac{3k+12\beta}{8-k}$		
16	$\nu > \nu_c$	$\frac{p}{2}$	$\alpha = \frac{12\beta+2k-4}{8-k}$		
			Wind, Structured Jet		
17	$\nu_m < \nu < \nu_c$	$\frac{p-1}{2}$	$\alpha = \frac{6\beta+k\beta+2}{4-k}$		
18	$\nu > \nu_c$	$\frac{p}{2}$	$\alpha = \frac{6\beta+k-k\beta-2}{4-k}$		

Figure 1.8 Closure relations between the temporal index α and the spectral index β in various regimes. From Racusin et al. (2009)

Piran, 1999a,b; Mészáros and Rees, 1999; Kobayashi and Sari, 2000; Kobayashi, 2000; Kobayashi and Zhang, 2003b; Zhang et al., 2003; Wu et al., 2003; Kobayashi and Zhang, 2003a; Kobayashi et al., 2004).
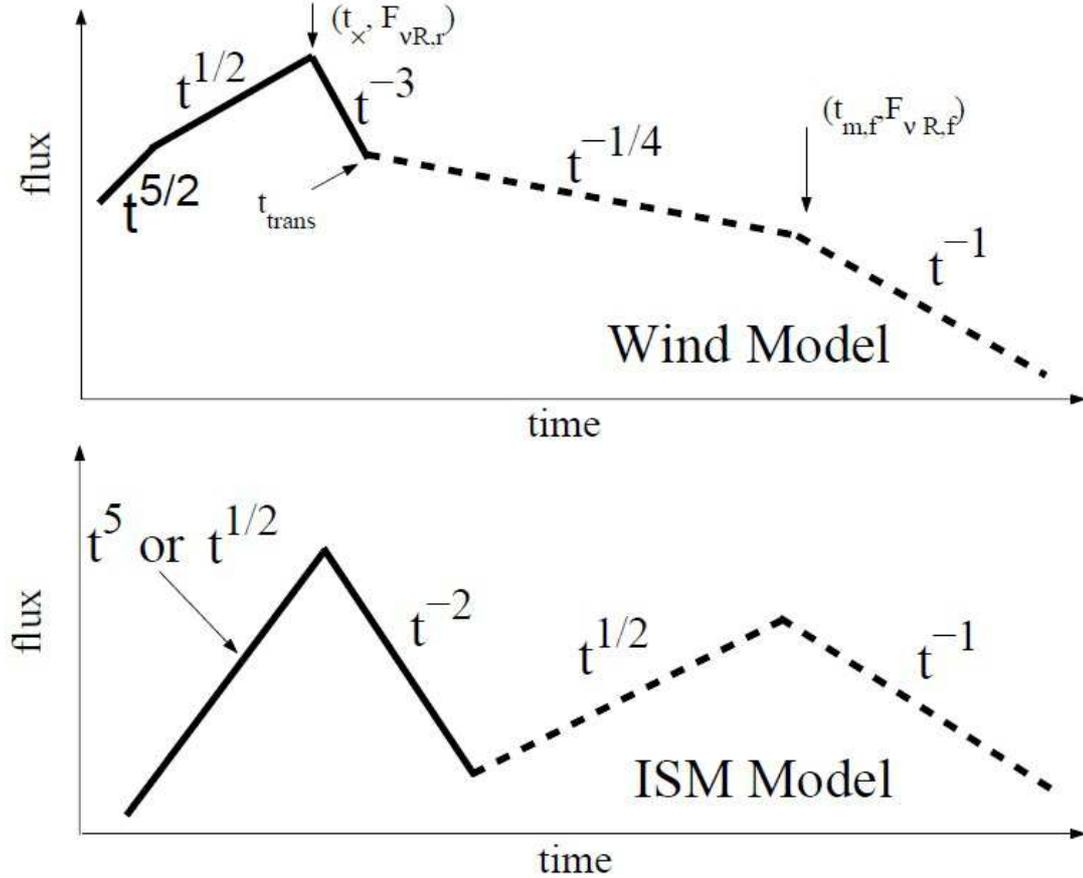
Figure 1.9 Optical light curve with the wind-like ambient medium (upper panel) and ISM (lower panel). Solid lines represent the emission from the reverse shock, dashed lines represent the forward shock component. From Kobayashi and Zhang (2003a).

In the reverse shock scenario, the external shock responsible for the afterglow emission consists of a forward shock, a blast wave propagating into the ambient medium, and a reverse shock, which propagates back into the fireball ejecta (Meszaros and Rees, 1993b). The emission from this reverse shock then produces bright optical flashes in the early part of the afterglow light curves (Shao and Dai, 2005). This reverse shock emission peaks very early and is short-lived, because the electrons are continuously accelerated only until the reverse shock crosses the initial fireball shell. Until the crossing time, the internal energy density across the contact discontinuity and the pressure are the same, but the shocked shell has much larger particle density than the shocked ambient medium. Given similar microphysical parameters, the typical energy per electron
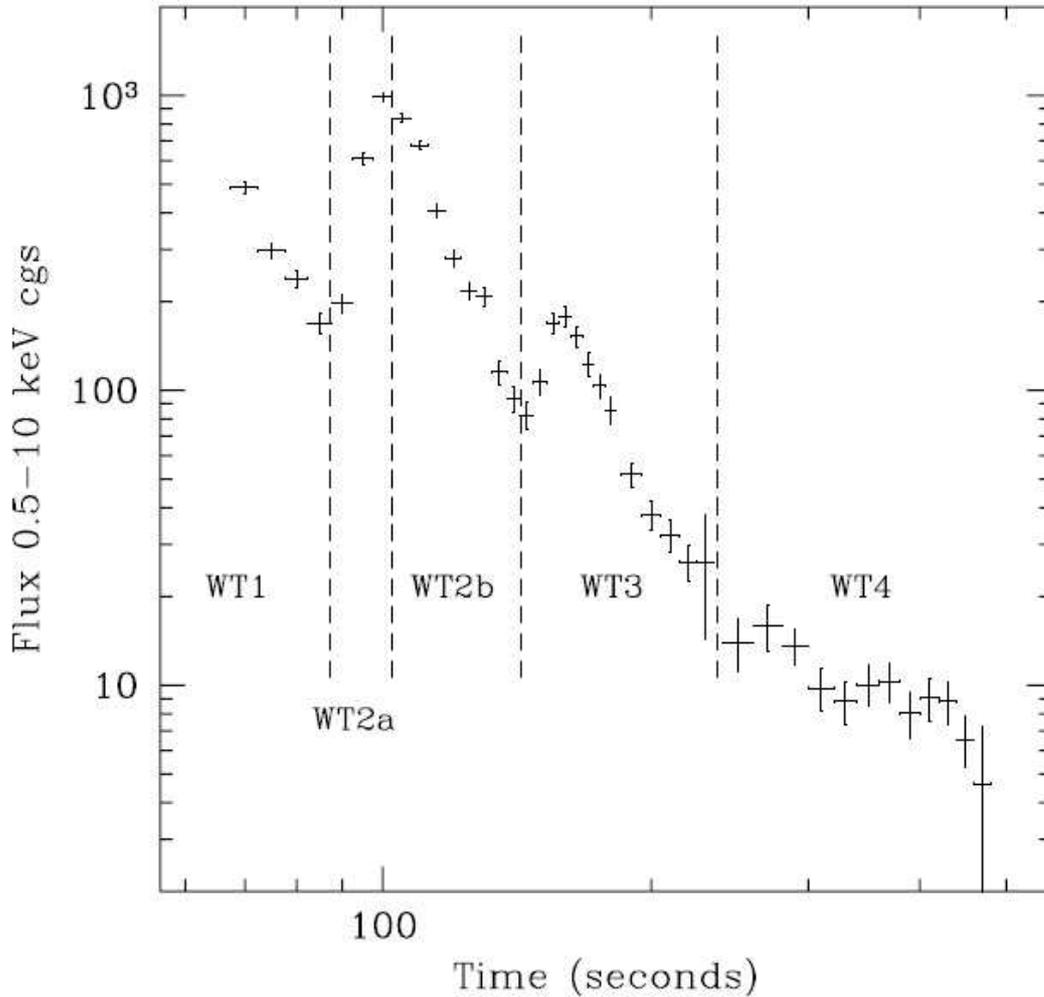
Figure 1.10 X-ray light curve of the afterglow of GRB 050713A showing several rebright-enings interpreted as the emission from refreshed shocks. From Guetta et al. (2007).

is much lower in the reverse shock region than in the forward shock region (Zhang and Mészáros, 2004). The peak frequency of the synchrotron emission in the reverse shock is therefore much lower than that in the forward shock, usually in the optical and infrared wavelengths (Meszaros and Rees, 1993a, 1997a; Sari and Piran, 1999a). Another distinctive feature of the reverse shock is the steep decay slope after the peak, with the temporal index $\alpha \gtrsim 2$ (Zhang et al., 2003; Kobayashi and Zhang, 2003a). A generic optical afterglow light curve involving a reverse shock is then a superposition of the emission from both shocks and includes two peaks, earlier one from the reverse shock, followed by the later one from the forward shock (Fig. 1.9).

1.2.2   Refreshed shocks

Apart from optical flashes, some light curves of the GRB afterglows show rebrightenings and bumps that are attributed to refreshed shocks (Rees and Meszaros, 1998; Panaitescu et al., 1998). In this scenario, the central engine is either long-lived and producing a post-injection of energy into the fireball during the afterglow phase, or short-lived like in the standard case but ejecting fireball shells with a range of Lorentz factors (i.e., variety of speeds). Whether the late arrival of the shell is due to its ejection at later time or due to its lower speed, when it catches up with the decelerated initial material, the kinetic energy in the late-arriving shell re-energizes or "refreshes" the external shock. The injection can be either continuous (Rees and Meszaros, 1998; Dai and Lu, 1998; Panaitescu et al., 1998; Sari and Mészáros, 2000; Zhang and Mészáros, 2001) or discrete (Kumar and Piran, 2000; Zhang and Mészáros, 2002b). The main characteristic of the refreshed shock is a generally achromatic (Kumar and Piran, 2000) increase of the flux level, which does not drop back to the pre-refreshed value but resumes the initial temporal decay slope after the rebrightening ends (Fig. 1.10). Such behavior has been seen for example in the afterglows of GRB 970508 (Panaitescu et al., 1998), GRB 030329 (Granot et al., 2003) and GRB 050713A (Guetta et al., 2007)

1.2.3   Density variations

While the duration of the energy injection into the fireball is determined by the characteristics of the central engine, the fireball deceleration time depends on the density profile of the ambient medium. This is usually expected to be either homogeneous ISM, where $n \propto r^0$, or a wind medium produced by the massive star progenitor, where $n \propto r^{-2}$. However, the density profile can change from one to another with the distance from the central engine or have irregularities on top of the otherwise smooth background. The most discussed scenario is the stellar wind from the GRB progenitor, which then transforms into ISM with the increasing distance from the GRB, leading to an external density jump (Ramirez-Ruiz et al., 2001; Dai and Lu, 2002) with a distinctive rebrightening seen for example in the afterglow light curve of GRB 030226 (Dai and Wu, 2003). The light curve humps can be also produced by the density clumps or fluctuations on top of the smooth ISM background (Wang and Loeb, 2000; Lazzati et al., 2002; Nakar et al., 2003; Heyl and Perna, 2003; Zhang et al., 2006; Ioka et al., 2005), or a wind termination shock, an abrupt increase in the radial density between wind environments of two evolutionary stages of the massive progenitor (Nakar and Granot, 2007; Panaitescu and Kumar, 2004a; Gendre et al., 2007; Lazzati et al., 2006; de Pasquale et al., 2006; van Marle et al., 2006). Any increase of the density in the ambient medium will enhance the transformation of the fireball kinetic energy into radiation and thus produce an increase in the afterglow light curve flux (Fig. 1.11). However, most recent simulations have shown that only smooth and low-amplitude bumps arise from variations in the density profile (Nakar and Granot, 2007; van Eerten et al., 2009).
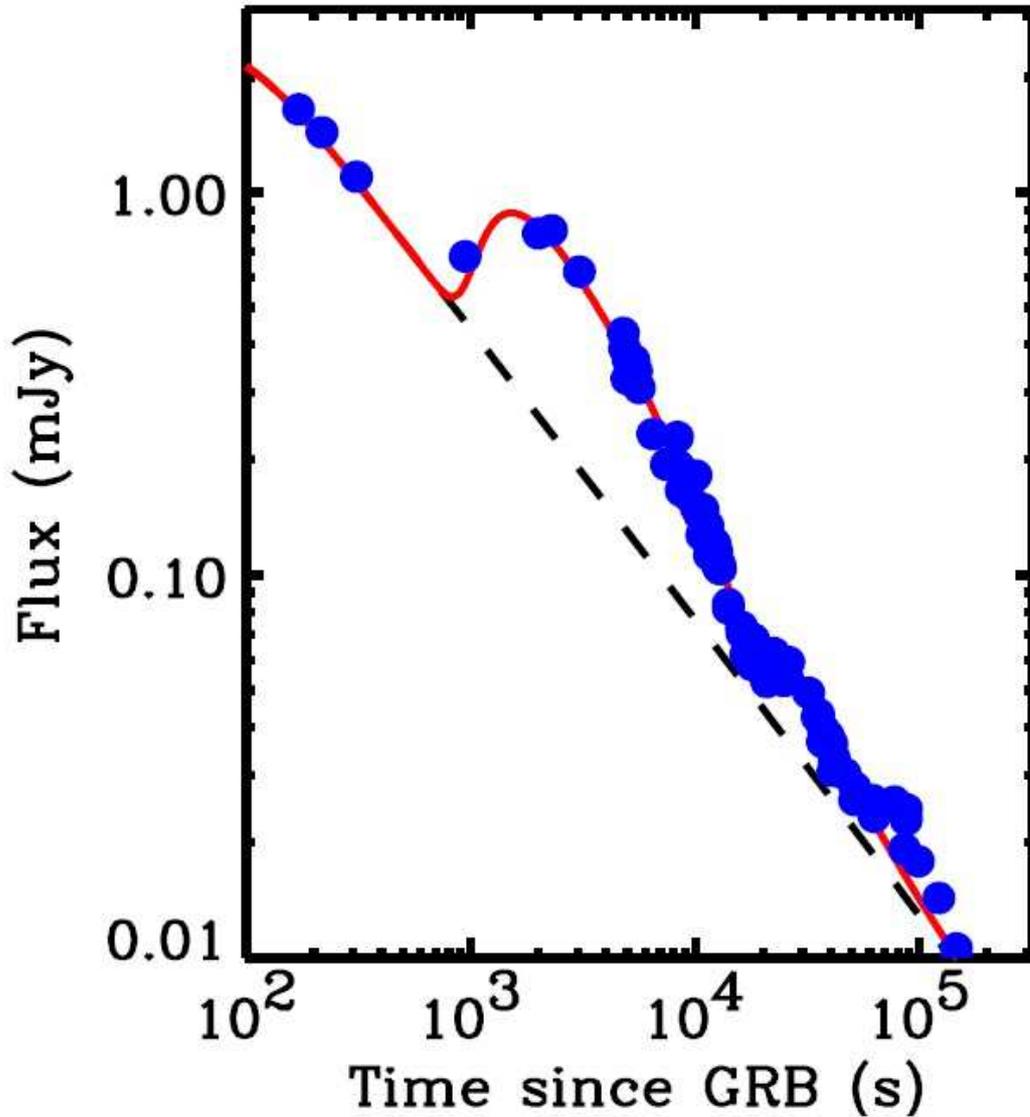
Figure 1.11 *R*-band light curve of the afterglow of GRB 021004. The solid line shows the model with density clumps on top of homogeneous ISM while the dashed line shows the evolution of the afterglow in a uniform ISM. From Lazzati et al. (2002).

1.2.4 Two-component jet

While there is a strong consensus that GRB fireballs are collimated in jets that are the cause of achromatic steepening breaks in the light curves of many GRB afterglows, the actual shape or distribution of energies per solid angle is still a matter of debate. One of the more complex models that gains popularity among theoreticians and observers

alike is a two-component jet model (Chapter 3, Huang et al., 2004; Peng et al., 2005; Sheth et al., 2003; Jin et al., 2007; Wu et al., 2005). The generic two-component jet model consists of a narrow and highly relativistic jet, responsible for the early afterglow emission, and of a wider and moderately relativistic jet, dominant in the later part of the light curve. In case of an on-axis geometry, the resulting afterglow light curve is a superposition of these two components, where the decelerating narrow jet creates the initial decay and the wide jet dominates the later emission that rises during the pre-deceleration phase, followed by the shallow decay and a possible jet break (Fig. 1.12). Such model has successfully explained complex light curves of the afterglows of GRB 030329 (Berger et al., 2003; Sheth et al., 2003), GRB 041223 (Burrows et al., 2005a), GRB 050315 (Granot et al., 2006), GRB 050401 (Kamble et al., 2009), GRB 050802 (Oates et al., 2007), GRB 051221A (Jin et al., 2007), GRB 070419A (Zheng and Deng, 2010), GRB080319B (Racusin et al., 2008), GRB 080413B (Chapter 3), GRB 090902B (Liu and Wang, 2011) and more.
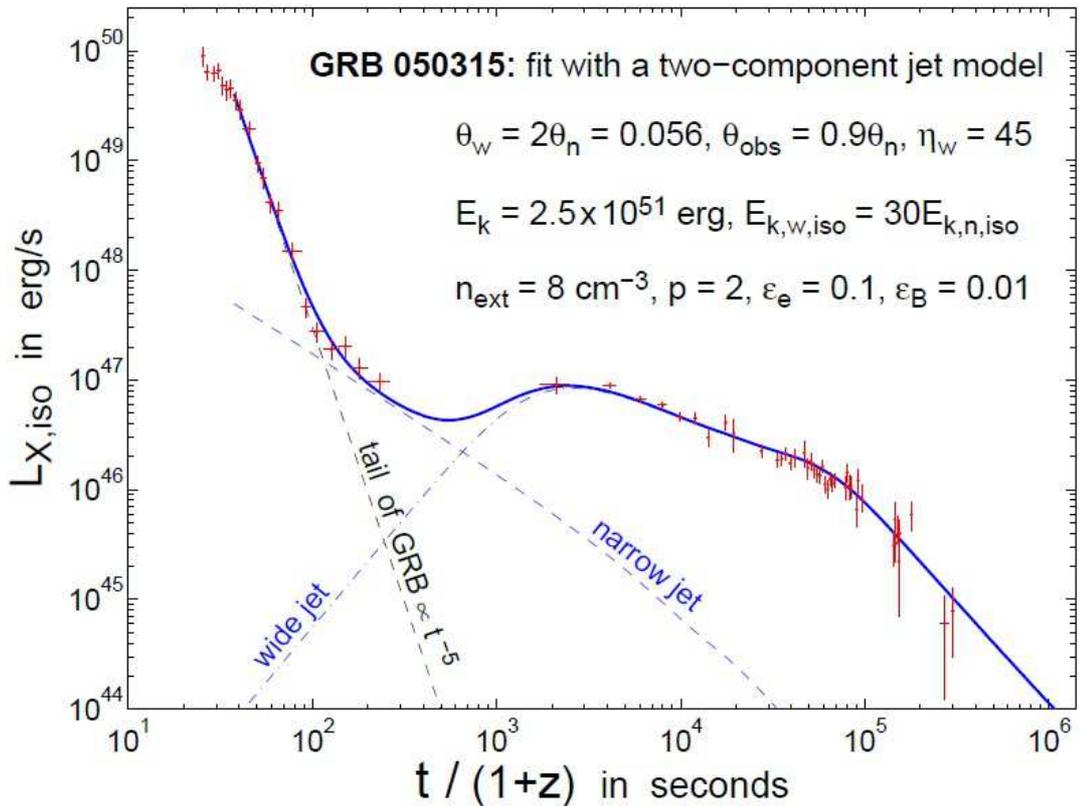
Figure 1.12 Two-component jet model fit to the X-ray light curve of GRB 050315 afterglow. The total light curve (solid line) is a superposition of contributions from the narrow and wide jets (dashed lines). From Granot et al. (2006).

Given that the two components of the jet can have different electron energy distribution index p, each component can dominate not only different temporal part of the light curve but also different wavelengths. It is not uncommon, that while the wider, less energetic jet dominates the later parts of the optical light curve of the afterglow, its evidence in the X-ray domain is negligible (see Chapter 3).

1.2.5 Microphysical parameters

Essentially almost all afterglow model fits to observed GRB data assumed all of the shock parameters $p, \epsilon_e, \epsilon_B$ not evolving in time. In principle, they may change but it is difficult to disentangle the effects of each parameter and quantify the evolution. Therefore, the microphysical parameters are usually treated separately, assuming non-evolution of the other two. The most speculated one is the fraction of the energy carried in the magnetic field ϵ_B. This is mainly because there is a growing number of studies which have modelled broad-band GRB light curves, and have yielded results for ϵ_B which span several orders of magnitude between different GRBs, with values from $\sim 10^{-5}$ to $\sim 10^{-1}$, while the values of p and ϵ_e are within an order of magnitude in different GRBs (see Fig. 1.13), suggesting that there is no standard value for ϵ_B as it probably evolves with time (Panaitescu and Kumar, 2001, 2002; Yost et al., 2003; Panaitescu and Kumar, 2004b). Lately, the idea of ϵ_B increasing in time as a power-law has been discussed and is receiving increasing support from observational data (e.g., Panaitescu et al., 2006a; Kong et al., 2010, Chapter 4). The easiest way to measure this evolution with the current instruments (see Chapter 2) is to measure the evolution of the spectral break ν_c. Assuming constant isotropic equivalent energy release E_{iso}, the temporal change of the cooling break frequency is only dependent on the evolution of ϵ_B (see Eq. 1.4). Given that the break frequency ν_c is mostly detected between X-ray and optical wavelengths, in which most of the afterglow observations are done, the measurements of the cooling break movement is a convenient way to test the hypothesis of the evolving ϵ_B parameter (see Chapter 4).

BEST-FIT PARAMETERS FOR A HOMOGENEOUS MEDIUM AND 90% CONFIDENCE LEVELS FOR 10 GRB AFTERGLOWS

GRB	E_0 ($\times 10^{50}$ ergs)	θ_0 (deg)	n (cm^{-3})	ε_e ($\times 10^{-2}$)	ε_B	p	χ^2 / dof	$n \propto r^{-2}$?
970508	20	18.3	0.75	11	4.5×10^{-2}	2.18	780 / 279	Yes
980519^a	$4.1^{+4.8}_{-1.4}$	$2.3^{+0.2}_{-0.2}$	$0.14^{+0.32}_{-0.03}$	11^{+4}_{-3}	$(3.5^{+32}_{-2.3}) \times 10^{-5}$	$2.78^{+0.07}_{-0.04}$	53 / 46	No
990123	$1.5^{+3.3}_{-0.4}$	$2.1^{+0.1}_{-0.9}$	$(1.9^{+0.5}_{-1.5}) \times 10^{-3}$	13^{+1}_{-4}	$(7.4^{+23}_{-5.9}) \times 10^{-4}$	$2.28^{+0.05}_{-0.03}$	55 / 56	No
990510	$1.4^{+4.9}_{-0.5}$	$3.1^{+0.1}_{-0.5}$	$0.29^{+0.11}_{-0.15}$	$2.5^{+3.1}_{-0.6}$	$(5.2^{+47}_{-4.7}) \times 10^{-3}$	$1.83^{+0.18}_{-0.01}$	36 / 69	No
991208	$2.4^{+2.8}_{-0.8}$	$12.8^{+1.5}_{-2.2}$	18^{+22}_{-6}	$5.6^{+2.1}_{-0.9}$	$(3.5^{+6.0}_{-2.1}) \times 10^{-2}$	$1.53^{+0.03}_{-0.03}$	112 / 97	Yes
991216	$1.1^{+1.0}_{-0.4}$	$2.7^{+0.4}_{-1.0}$	$4.7^{+6.8}_{-1.8}$	$1.4^{+0.4}_{-0.3}$	$(1.8^{+3.4}_{-0.7}) \times 10^{-2}$	$1.36^{+0.03}_{-0.03}$	42 / 41	Yes
000301c........	$3.3^{+0.3}_{-0.5}$	$13.7^{+0.6}_{-0.5}$	27^{+5}_{-5}	$6.2^{+1.4}_{-1.3}$	$(7.2^{+3.1}_{-1.5}) \times 10^{-2}$	$1.43^{+0.05}_{-0.07}$	119 / 96	Maybe
000418	32^{+120}_{-14}	50^{+30}_{-12}	27^{+250}_{-14}	$7.6^{+1.2}_{-3.2}$	$(6.6^{+48}_{-5.7}) \times 10^{-3}$	$2.04^{+0.07}_{-0.18}$	55 / 61	Yes
000926	$3.2^{+0.3}_{-0.3}$	$8.1^{+0.5}_{-0.6}$	22^{+5}_{-5}	10^{+2}_{-2}	$(6.5^{+1.5}_{-1.1}) \times 10^{-2}$	$2.40^{+0.01}_{-0.02}$	159 / 102	No
010222	5.1	4.6	1.7	0.43	6.7×10^{-5}	1.35	230 / 87	Yes

^{a} Redshift unknown; $z = 1$ was assumed.

Figure 1.13 Table with best-fit parameters for a sample of 10 GRBs showing large span of values of parameter ϵ_B. From Panaitescu and Kumar (2002).

All of the above additions to the fireball model show that scientists have an increasing problem explaining their observed GRB afterglows with the assumptions of the simplest shock model and needed to invent more and more complex models to fit their light curves. This thesis shows how complex and innovative models are used to model and explain light curves and SEDs of GRB afterglows observed with the newest generations of detectors (see Chapters 3 and 4). Given that some of the latest best-sampled afterglows are difficult to explain even with any of these complex fireball models (see Chapter 5), the question arises whether the fireball shock model needs to be further expanded or abandoned altogether.

Chapter 2

Instrumentation

2.1 Swift[1]

The *Swift* satellite (Gehrels et al., 2004) was launched in 2004 with a mission to quickly locate and observe GRBs and their afterglows in several wavelengths. It is part of NASA's medium explorer (MIDEX) program and was developed by an international team from the United States, the United Kingdom, and Italy, with additional scientific involvement in France, Japan, Germany, Denmark, Spain, and South Africa. The main scientific goals of the *Swift* GRB mission is to determine the origin of GRBs, classify them, study the environment around GRBs and their mutual interaction, use gamma-ray bursts as the probes of the earliest universe and perform a hard X-ray survey of the sky. *Swift* discovers around 100 bursts per year using its three instruments sensitive in γ-ray, X-ray and optical/ultraviolet wavebands. This is mainly thanks to its very rapid slewing capability (50 degrees in less than 75 seconds) and precise localization (0.5-5 arcsec positions for almost every GRB). Each burst is first detected in the γ-rays by the Burst Alert Telescope (BAT, Barthelmy et al., 2005) and the position is used to slew the satellite and detect the afterglow using the X-Ray Telescope (XRT, Burrows et al., 2005b) and the UltraViolet Optical Telescope (UVOT, Roming et al., 2005).

The BAT is a highly sensitive coded aperture imaging instrument with the energy range of 15-150 keV and a 1.4 steradian field of view (half coded). Within few seconds of detecting a burst, the BAT calculates an initial position with a 4 arcmin accuracy, decides whether the spacecraft needs to slew to the burst to position it in the field of view of the XRT and UVOT and, if so, sends the position to the spacecraft. For GRB detection, the BAT uses a two-dimensional 2.7 m^2 D-shaped coded aperture mask and a large area (5200 cm^2) solid state CdZnTe detector array. The burst trigger algorithm looks for excesses in the detector count rate above constant sources and 4-11 σ above background noise with a typical value of 8 σ. Thanks to the imaging capability of the BAT instrument, the on-board software can check that the trigger is a point source, eliminating fake triggers like flickering in bright galactic sources and magneto-spheric

---

[1]This section uses information from the User's manuals for *Swift* and from `http://www.nasa.gov/mission_pages/swift/main/index.html` and `http://heasarc.nasa.gov/docs/swift/`
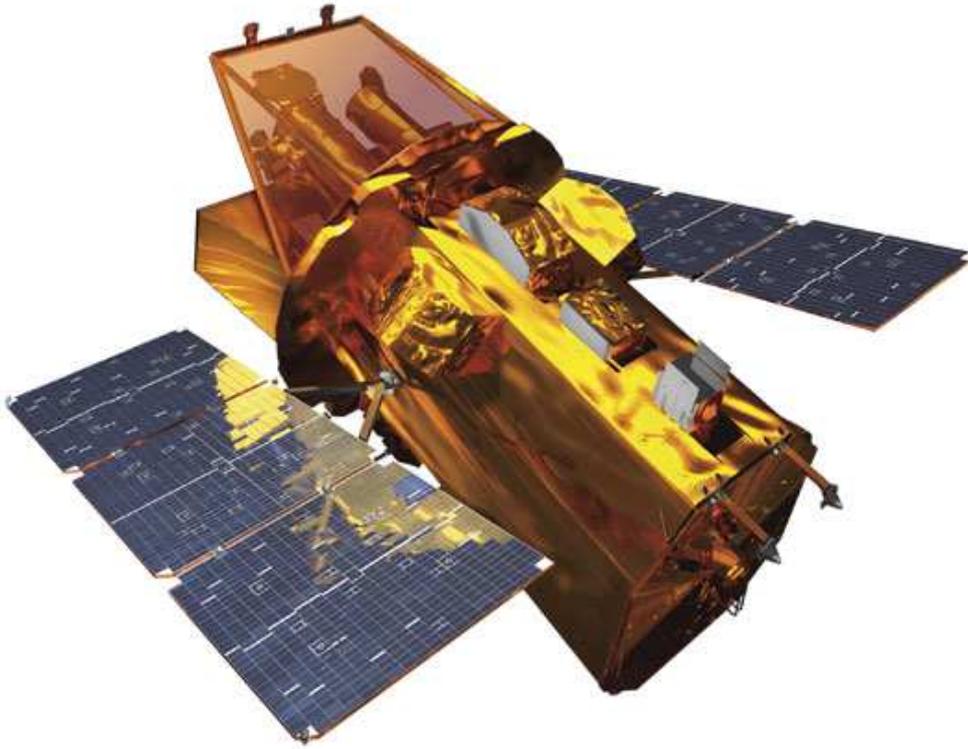
Figure 2.1 A computer-generated drawing of the Swift satellite. Credit: NASA E/PO, Sonoma State University, Aurore Simonnet

particle events. When the GRB is detected, the information about the burst intensity and position are immediately transfered to the ground and distributed to the community using the Gamma-Ray Burst Coordinates Network (GCN, Barthelmy et al., 2000).

The XRT is a focusing X-ray CCD imaging spectrometer designed to measure the fluxes, spectra, and light curves of GRB afterglows in the 0.2-10 keV energy range. It has a 110 cm^2 effective area and 23.6×23.6 arcmin field of view. Thanks to rapid slewing, the XRT can start observing 20-70 seconds from the burst discovery by the BAT and localize the GRB to 5 arcsec accuracy. This is precise enough for the ground-based telescopes to be able to locate the optical counterpart of the GRB afterglow. The XRT supports several science modes to enable it to cover the dynamic range and rapid variability expected from GRB afterglows, and autonomously determines which readout mode to use based on the source brightness. When observing a new GRB the XRT first takes an image in Image mode to calculate the on-board source position and after that runs in sequence the following modes: Photodiode, Windowed Timing and Photon Counting, switching automatically between modes according to the source intensity. The Photodiode mode is designed for very bright GRBs, it does not provide spatial information but produces a high resolution light curve and a spectrum. The
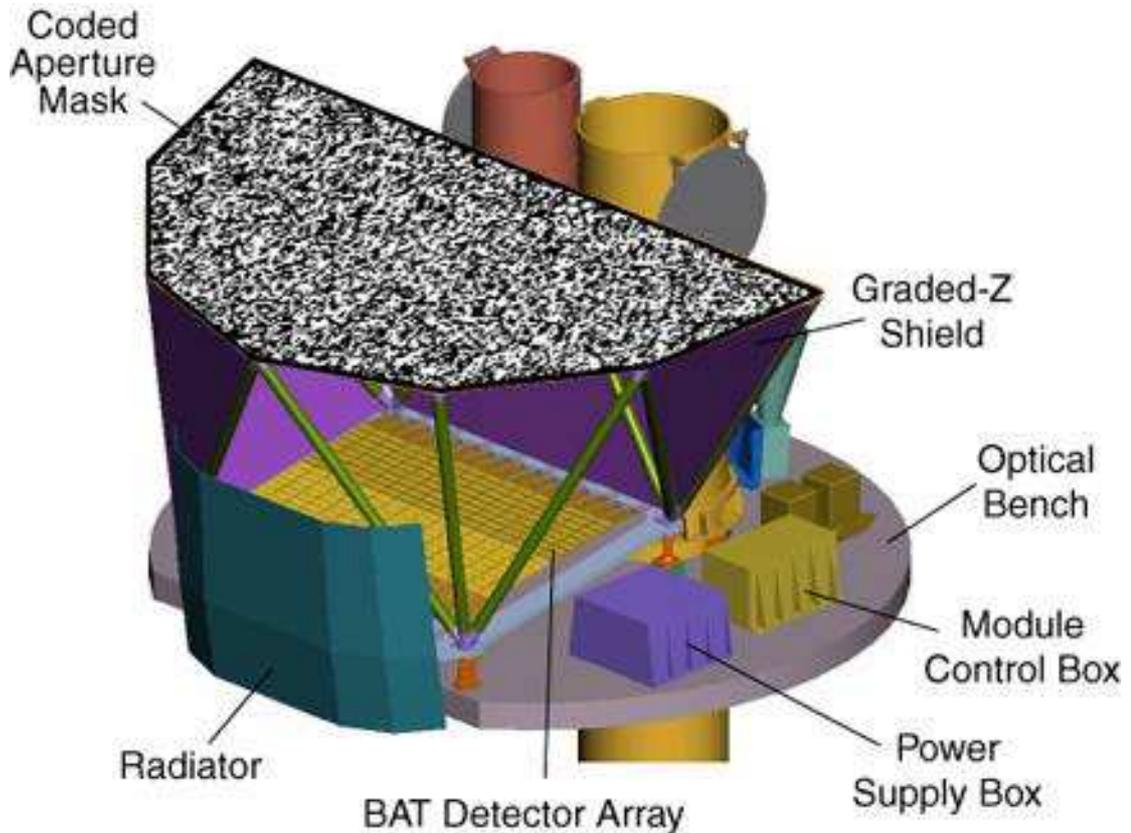
Figure 2.2 A schematic drawing of the Swift optical bench with the BAT instrument. The main BAT structures are the coded aperture mask and the detector array. Credit: NASA

Windowed Timing mode is obtained by compressing 10 rows into a single row, and then reading out only the central 200 columns of the CCD . It thus provides a one dimensional imaging and a time resolution of 1.7 ms. Most of the afterglow observation time is spent in the Photon Counting mode, which retains full imaging and spectroscopic resolution but the time resolution is limited to 2.5 seconds.

The UVOT is an ultraviolet/optical diffraction-limited 30 cm Ritchey-Chrétien reflector sensitive in $170 - 650$ nm wavelength range. It has a field of view of 17×17 arcmin, and can locate the afterglow with a 0.5 arcsecond accuracy. When a new GRB is acquired by the BAT and the Swift has slewed to the position, the UVOT acquires a 150 s white exposure of the target field and then continues through a predetermined program of exposure times and filter combinations. Thanks to its seven filters, low-resolution spectra can be taken for the brightest UV/optical afterglows, which can then be used to determine the redshift via the observed wavelength of the Lyman-alpha cut-off (Krühler et al., 2011b). The UVOT is well suited for afterglow studies, because of its ultraviolet capability which is not possible from the ground, and the absence of
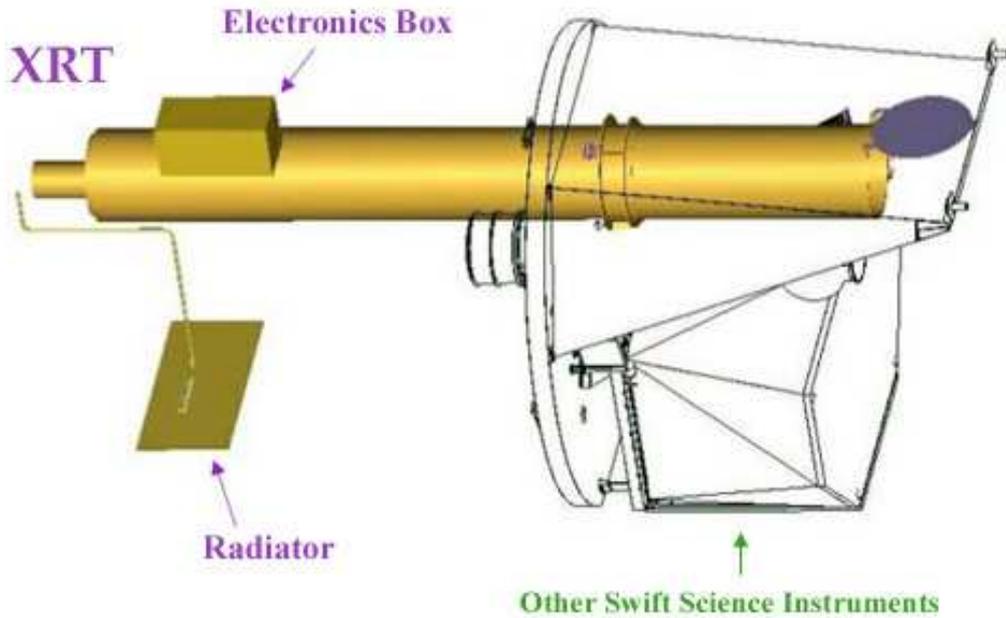
Figure 2.3 The schematic layout of the XRT instrument showing its grazing incidence Wolter 1 telescope. Credit: NASA

atmospheric extinction, diffraction, and background. On the other hand, the main constraints for the observation with the UVOT and other instruments onboard *Swift* are the Moon (e.g., D'Elia et al., 2011; Troja et al., 2009b) and Earth limb constrains (e.g., Perri et al., 2007; Page et al., 2005), together with the ~ 96 min orbital period around the Earth.

2.2 GROND

2.2.1 Instrument characteristics

The Gamma-Ray burst Optical Near-infrared Detector (GROND, Greiner et al., 2008, 2007) is a seven-channel imager with four optical and three near-infrared detectors, covering the wavelength range of 360-2300 nm. It was built at MPE Garching and mounted at the 2.2 m MPI/ESO telescope at La Silla observatory in Chile in April 2007 with a mission to perform follow-up observations of GRB afterglows discovered (primarily) by the *Swift* telescope. It has four optical CCD detectors, each with field of view of 5.4×5.4 arcmin and each equipped with one Sloan system filter g', r', i', z' (Fukugita et al., 1996). The three near-infrared (NIR) HAWAII-1 detectors have field of view of 10×10 arcmin each, which was the reported GRB localization accuracy of
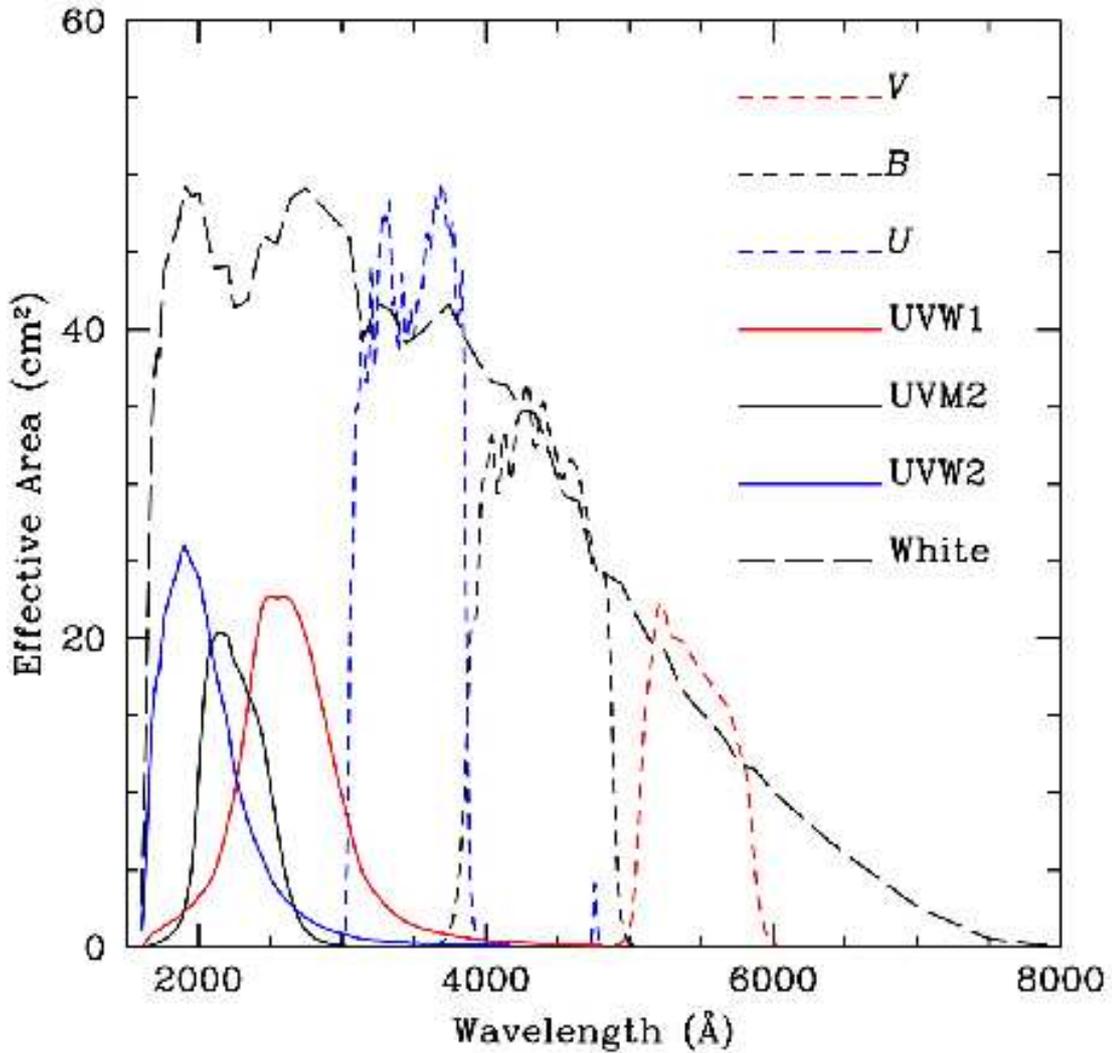
Figure 2.4 The image showing effective area curves for the seven broadband UVOT filters shown as square centimeters versus wavelength in Angstroms. Credit: NASA

the BAT at the time GROND was build. The NIR detectors have J, H and K_s filters of the extended Johnson system (Johnson and Morgan, 1953), used in the Two Micron All Sky Survey (2MASS) (Skrutskie et al., 2006). The unique property of the GROND instrument is the capability to observe in all these seven bands simultaneously. This is possible thanks to a system of dichroics, where the short wavelength part of the light is always reflected off the dichroic, while the long-wavelength part passes through it.

Simultaneous multi-band observation is required for a very quick photometric redshift determination based on the Lyman-alpha break (Lamb and Reichart, 2000), in
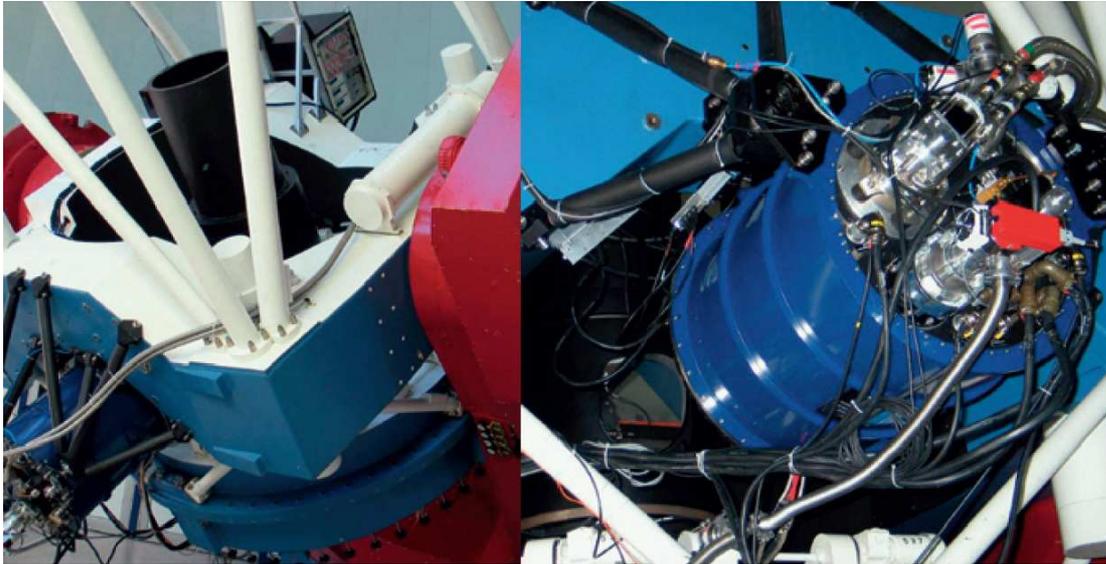
Figure 2.5 **Left**: The 2.2 m telescope with GROND mounted to it side (lower left corner). The black tube in the middle is the light baffle of the M3 mirror. The main electronics rack of GROND is visible in the upper right corner. **Right**: Detailed view of the GROND vessel with the Helium closed-cycle cooler and the vacuum pump visible. From Greiner et al. (2007)

which GROND excels with high accuracy (Krühler et al., 2011b). Given that GRB afterglows fade rapidly, high redshift value determined by GROND is then used as a trigger for more detailed follow-up observation with larger telescopes, while the afterglow is still bright enough for a high resolution spectroscopy for example, required to measure the physical conditions of the burst environment (Vreeswijk et al., 2007). While the UVOT onboard the *Swift* satellite measures redshift using the same principle, its range is limited to $z \sim 1.3 - 5$. Compared to that, GROND has a range of $z \sim 3.5 - 13$ and can therefore detect afterglows of the most distant GRBs, including the current record holder GRB 090429B with the redshift of ~ 9.4 (Cucchiara et al., 2011). While the GROND instrument was designed to be fully autonomous, the needed promptness in the GRB localization, redshift determination and solving of potential HW and SW problems, together with the slow internet connection to La Silla, requires that at least one member of the GROND observers team, composed mainly of PhD students and Post-docs, is present at La Silla observatory.

The GROND instrument can observe any object in the sky and is often used for a study of quasars (Morganson et al., 2011), supernovae (Olivares, subm.), blazars (Rau, in prep.), transiting exoplanets and others. However, it was mainly designed for a prompt automatic GRB follow-up observation. To be able to do this, GROND is running in the Rapid Response Mode (RRM), which ensures that it automatically stops all other ongoing observations and moves the telescope to the latest trigger position. The override

rule of the RRM applies not only for the ongoing observations with GROND but also for the other two instruments mounted on the 2.2 m telescope; the Wide Field Imager (WFI, Wisotzki et al., 2001) and the fiber-fed Echelle spectrograph FEROS (Kaufer et al., 1999). In order to produce the smallest possible impact on these two instruments, a movable M3 mirror was designed for the 2.2 m telescope. In the case of a GRB trigger, the M3 mirror is folded in 20 seconds and reflects the light from the source towards the side of the telescope (Coudé-like focus), where GROND is permanently mounted. In case GROND is not used, the M3 mirror moves away and the light goes directly in the Cassegrain focus of the telescope to the WFI or FEROS.

2.2.2 Observations with GROND

The GROND observations themselves are performed using the observation blocks (OBs, Chavan et al., 2000), which are combinations of different number and lengths of exposures of the seven detectors. Each OB contains set of parameters, the most important ones are the number of exposures in optical bands and their length, the number of K mirror dither positions (used due to a high sky brightness), the number of exposures in NIR bands during one K band mirror position and their length, and the number of telescope dither positions (TDs, used to determine the sky variations in NIR channels). In order to comply with the GROND science objectives and to best lay out the exposures, read-outs and transfers of all channels, different default OB types are defined for observations with GROND. These OBs are named after their total integration time in a single NIR channel in minutes and the number of the telescope ditherings during one OB. The most commonly used OBs for GRB afterglow observations are 4min4TD, 8min4TD and 20min4TD. In the case of highly crowded fields in the Galactic plane, OBs with higher number of TDs are used for better background subtracion, for example 12min6TD, 30min6TD, 10min8TD, etc. The number of K band mirror ditherings is always 6 per each telescope position, the only difference between OBs is then the number of NIR exposures per K band mirror position.

As apparent from the relatively long exposures (4 minute OB is the shortest one), GROND is designed for observation of fainter objects like GRB afterglows, which moreover fade rapidly. The layout of the 4min4TD OB is consisting of six K band mirror ditherings and 10 second exposure of NIR channels during each of them. The exposure in the optical channels takes ~ 35 seconds in the slow readout mode or 66 seconds in the fast readout mode, which introduces higher noise but reduces the read-out time from 46 s to 4.4 s. The readout of NIR channels takes only 2 seconds and enables GROND to expose in NIR channels even while optical channels are reading out. This pattern repeats another three times at four different telescope dither positions. The output of the 4min4TD OB are 4 images in each optical g', r', i', z' band in the form of the FITS datacubes and 24 individual images in each NIR J, H, K band in the form of the FITS files with all three bands next to each other. The longer OBs then simply increase the exposure length in the optical channels and number of exposures per each K band mirror position, while the exposure length in NIR channels remains
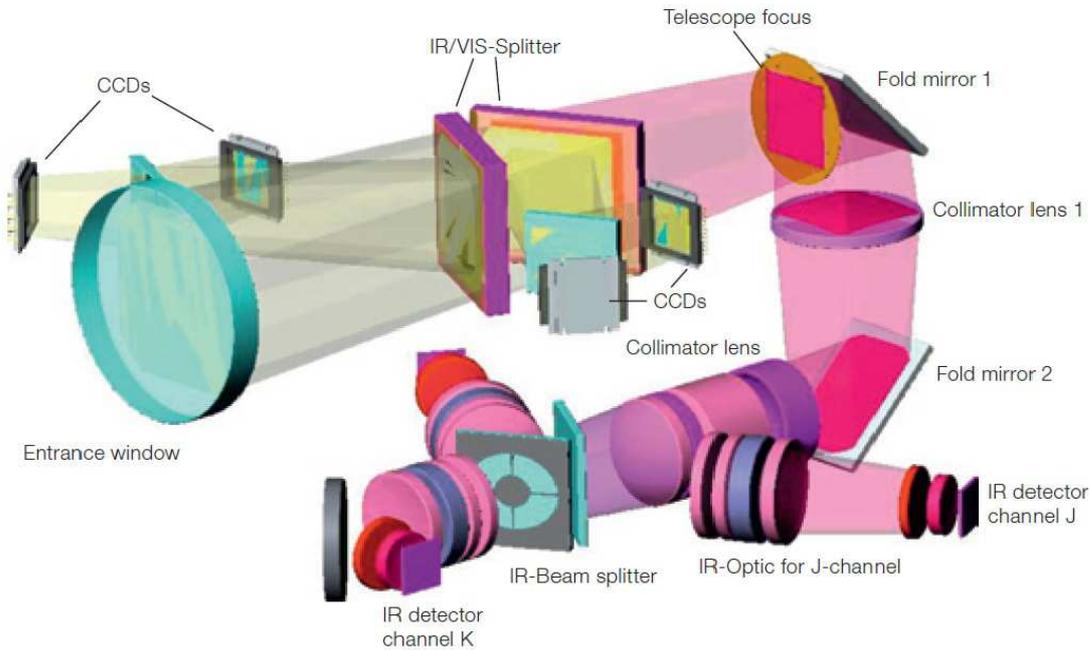
Figure 2.6 3D structure of the optical beam of GROND with most of the components labeled. From Greiner et al. (2007)

to be 10 seconds long in order to not saturate the sky. The obvious asynchronicity of the exposure mid-times of optical channels compared to NIR channels is discussed in the next section.

Non-RRM OBs can either be created and executed using ESO *p2pp* tool, used also for all ESO instruments, or using a GROND Pipeline (GP, Yoldaş et al., 2008), a software custom-designed for GROND. The GP is used for automatic scheduling of OBs in the RRM mode and has a web browser interface (`http://wgrpipe.ls.eso.org:9222/gp/app/`) so that it can be accessed by any member of the GROND team from any place in the world. The prime objective of the GP is to schedule prompt observations of GRB afterglows and determine their magnitudes and redshifts as quickly as possible. When a GRB alert comes in via the GCN socket connection, the GP extracts all information from the packet, decides whether it is a valid trigger for a new GRB and calculates the visibility of the target. If the target is observable and complies with other checks (e.g. Moon distance), the GP schedules a sequence of OBs with an increasing exposure length. This sequence can be anytime modified, added or deleted by the user via the web interface based on the other information on the target. When the start time of the observation comes and if the RRM is on, the GP ends any ongoing observation, presets the telescope to a new position, tilts the M3 mirror if needed and sets up GROND for observations. The pre-defined sequence of OBs is executed after the telescope preset is complete and the guiding started. When the sequence ends, the M3 is moved back

and the observation of the previous program can resume. Apart from choosing the guiding star, all the above steps are done autonomously without any interaction from the GROND observer, who mainly adjusts the OB sequence according to circumstances.

2.2.3 GP data analysis

The second independent layer of the GP system conducts the analysis of the observed data immediately after the OB finishes. The analysis includes pre-processing of the images, astrometric correction and photometric calibration. Details are described in the next section about data handling. Unless the precise position of the afterglow has been detected by the UVOT or other telescope and reported in the GCN, the main goal of the GROND observer is to identify the afterglow in the GROND images. This is done by looking for uncatalogued sources inside the area given by the gamma/X-ray/optical position error circles distributed by GCN packets. The GRB candidate is then confirmed by the variability in observed magnitudes and colors resembling other optical/NIR afterglows (Rhoads, 2001). If no suitable candidate is found in any of the seven bands, the observer increases the length of the OB or stacks several OBs together (see section Data handling). After finding the afterglow and obtaining all seven magnitudes of the afterglow, the photometric redshift is determined using customized version of the publicly available HyperZ code (Bolzonella et al., 2000). This script fits the seven magnitudes with the power law, possible host dust extinction and Lyman alpha break if it is covered by the data. With this method, the redshift can be determined in a range of $z \sim 3.5 - 13$ with an accuracy of $\Delta z \sim 0.3 - 0.5$.

In case of a high measured redshift, a spectrograph on some larger telescope can be triggered immediately and obtain a spectroscopic confirmation of the redshift, if an ESO proposal to do so was accepted. In any case, the observer together with another GROND team member who is currently on "home shift" writes a GCN reporting either upper limits if the afterglow is not seen in any band (Filgas et al., 2009b), or reporting the afterglow position and magnitudes if it is (Filgas et al., 2010). In order to obtain an afterglow light curve with high temporal resolution during the whole visibility of the GRB, follow-up observations are scheduled in the course of following days, weeks and even months. For calibration purposes, bias and dark images are taken daily and skyflats at least once a week. If the source is not in the field covered by the Sloan Digital Sky Survey (SDSS) catalog, the observation of the closest photometric Sloan standard star (Smith et al., 2002) or an SDSS field is performed during photometric conditions, with observation of the GRB field following shortly. After the observing shift of the GROND team member is finished, the data are copied to a USB disk and brought to Garching for analysis.
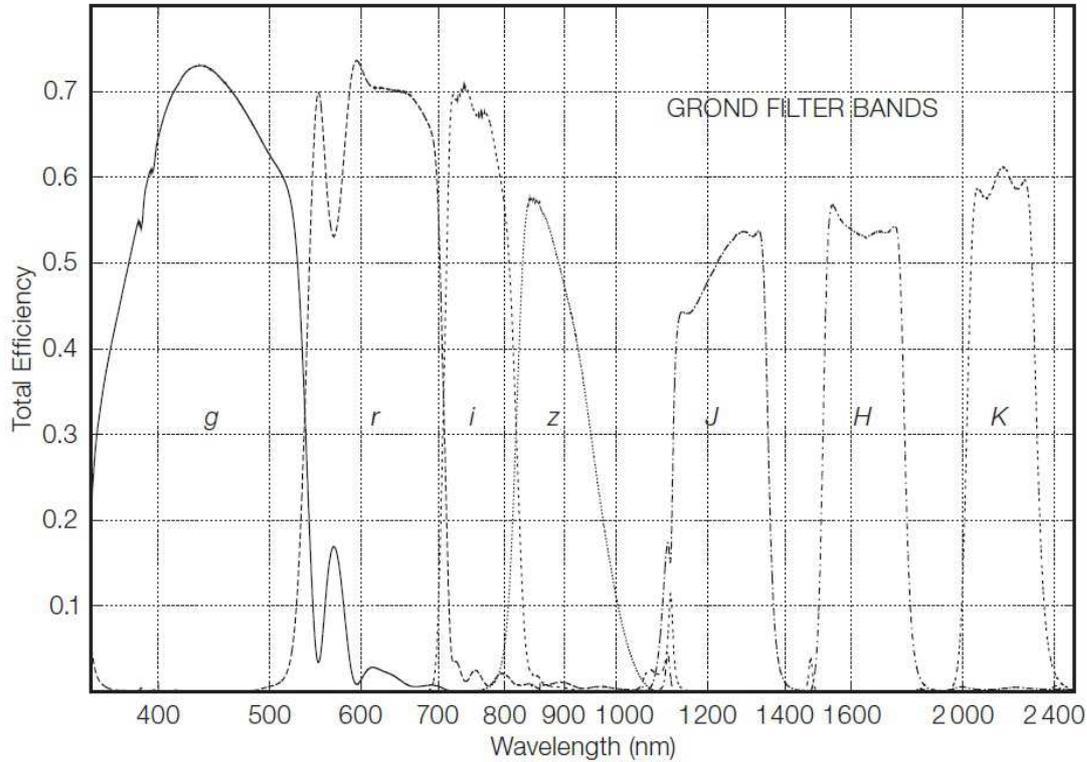
Figure 2.7 GROND filter curves showing the total efficiency of the instrument including the telescope mirrors, GROND optics and detectors. From Greiner et al. (2007)

2.3 Data handling

2.3.1 *Swift*/XRT data

All XRT light curves in this thesis were obtained from the *Swift*/XRT GRB light curve repository (Evans et al., 2007, 2009a) at `http://www.swift.ac.uk/xrt_curves/`. Data observed in the Windowed Timing mode and the Photon Counting mode were downloaded as ASCII tables containing mid-times of exposures, times errors, source count-rates and errors of source count-rates. These tables were then used for fitting with the script used for fitting the GROND light curves, described later. All XRT spectra in this thesis were obtained from the *Swift*/XRT GRB spectra repository at `http://www.swift.ac.uk/xrt_spectra/`. The repository automatically creates a time-average spectrum of any observed GRB but, more importantly, allows the user to create his own time-sliced spectra at any given time ranges. For each such spectrum, user defines a time range of XRT data used to build the spectrum and the repository provides him with a download link to those spectral data. The download includes files with an unbinned source spectrum for requested time interval and observing mode, a background spectrum for the time interval and mode, and an ancillary response file. The response matrices

were obtained from the most recent CALDB (*Swift* calibration database) release.

The spectral data are then grouped using the *grppha* task and fitted in XSPEC v12 using χ^2 statistics. The modelling is based on several parameters, which can be either fixed to a known value or left free to vary and then obtained from the best fit. Known parameters usually are the redshift of the GRB and the Galactic foreground absorbing column with a hydrogen column density N_H obtained from Kalberla et al. (2005). The parameters obtained from the straight power-law fit to the data are the photon index, defined as a spectral index $\beta + 1$ and characterizing the slope of the power-law, and the absorbing column local to the GRB host galaxy. The errors of the fits on any single parameter were obtained using the *uncert* task in XSPEC. This calculates the error on the parameter in question while allowing all the other non-frozen parameters in the model to vary. However, much more relevant than the fits of the XRT data alone are fits of the broad-band data together with GROND, which are discussed later in this section.

2.3.2   GROND data

After the GROND data are transferred to Garching, they are reduced and analyzed. All the analysis processes utilize Pyraf/IRAF (Tody, 1993) libraries[2] and are conducted using GROND analysis pipeline (see PhD thesis of Thomas Krühler, TUM for details), similar to the one used by the GP on La Silla. The main difference is that the GP is set to speed, therefore it skips some less important steps in the image pre-processing. The GROND analysis pipeline is slower but set for maximum precision of the obtained photometry. The first step is the pre-processing of the raw images. All images are corrected for the dark current and bias, introduced by the detector and electronics. Follows the correction of the multiplicative effects, i.e. the pixel-to-pixel sensitivity and the illumination variations across the image. Images in NIR bands are sky subtracted and corrected for the geometrical distortion introduced by the focal reducer lenses in front of the infrared detectors. Images of each telescope dither position (TDP) are then shifted and added to create one image in each band for one OB. However, in case the source is bright enough, the following astrometry and photometry can be done not only on the final image but also on each TDP image of the OB, obtaining for example 4 TDP magnitudes and 1 OB magnitude of each object in each band in case of a 4min4TD OB. For exceptionally bright GRBs ($J < 16$ mag), even the individual 10 s NIR images can be reduced and analyzed separately. In case of a very faint source, the images can be stacked together to produce an image with longer exposure, which is equal to the sum of exposures of stacked images. Whatever the combination of TDPs and OBs, astrometry and photometry is conducted on the resulting images.

Astrometry is done by matching the objects detected in the images to those that are in the optical or infrared catalogs, namely USNO A-2, USNO B1, SDSS, DENIS,

---

[2]IRAF (see `iraf.noao.edu`) is a data reduction and analysis software package of NOAO, and Pyraf (see `www.stsci.edu/resources/softwarehardware/pyraf`) is a Python wrapper for IRAF, provided by the Space Telescope Science Institute.

2MASS, NOMAD and GSC22 which are downloaded from `vizier.u-strasbg.fr/viz-bin/VizieR`. The resulting astrometric uncertainty is as good as ~ 0.3 arcsec. The photometry is performed by constructing a general model for the point-spread function (PSF) of each image using bright field stars and fitting it to the afterglow. In addition, aperture photometry is carried out, with the results consistent with the PSF photometry. Photometric calibration is performed relative to several secondary standards in the GRB field. In case of NIR bands, the secondary standards are covered by the 2MASS catalog and are used for calibration of the apparent magnitudes of the afterglow. The same method applies for optical bands in rare cases when the field is covered by the SDSS catalog. Otherwise the magnitudes of the nearest Sloan standard star or stars in the SDSS field, observed shortly before or after the GRB field, are transformed to the GROND filter system using their spectra and the GROND filter curves (Greiner et al., 2008). The obtained zero points are then corrected for atmospheric extinction differences and used to calibrate the secondary standards in the GRB field, used again for calibration of the apparent magnitudes of the afterglow. All data are then corrected for a Galactic foreground reddening $E_{\rm B-V}$ in the direction of the burst obtained from the NASA/IPAC Dust web-browser interface (`http://irsa.ipac.caltech.edu/applications/DUST/`) (Schlegel et al., 1998). At the end, NIR data are converted from Vega magnitudes to AB magnitudes for consistency with optical data, which are in AB magnitudes. The transformation factors for the GROND filter system are $\delta J = 0.91$ mag, $\delta H = 1.38$ mag, $\delta K_s = 1.80$ mag for older bursts observed before mid 2008 (Chapter 3), and $\delta J = 0.928$ mag, $\delta H = 1.404$ mag, $\delta K_s = 1.864$ mag for new observations (Chapters 4 and 5).

2.3.3 Light curve fitting

For fitting the light curves of GRB afterglows observed with GROND and *Swift*/XRT, a Python script was designed and coded (PhD thesis of Thomas Krühler, TUM), which allows the user to fit the observed datapoints with various models using χ^2 statistics. The models are combinations of straight power-laws, power-laws with one or two smooth breaks, host contributions, Gaussians and supernova emission bumps. The simplest model fits a straight power-law to the data with the temporal slope α and its 1σ error as the output. The broken power-law model connects two power-laws with a smooth break using formula (Beuermann et al., 1999)

$$F_t \propto \left[(t/t_{\rm break})^{-s\alpha_1} + (t/t_{\rm break})^{-s\alpha_2} \right]^{-1/s} , \tag{2.1}$$

where α_1 is the temporal slope before the break, α_2 the temporal slope after the break, $t_{\rm break}$ the time of the break and s the smoothness (or sharpness) of the break. The smaller the value of s, the smoother the break connecting the two power-laws and vice versa. Similarly, a model with three power-laws connected by two smooth breaks at two different times is available. The contribution from the host galaxy of the GRB is modelled as a constant flux. The Gaussians and SN components can be fit to the bumps in the light curve but are not used in this thesis.

All the above models can be combined, the resulting fit to the light curve is then a superposition of all the components used. The most complex light curve model currently in the script is the sum of a broken power-law, triple power-law with two breaks and a host contribution, coded specifically for GRB 080314B (Chapter 3), showing once more the increasing difficulty of modelling detailed light curves with the simple fireball shock model, which requires adding more and more components to it. The fitting can be done to seven GROND bands and XRT simultaneously (Fig. 3.2) or on any smaller combination of the eight bands down to a single band (Fig. 4.3). When fitting several bands simultaneously, to output is the best fit to all filters at once, the only parameter differing between bands is the normalization. The script also computes χ^2 statistics of the fit, 1σ errors of all free parameters and residuals of datapoints to the fitted model.

2.3.4 Broad-band SEDs

The construction of narrow-band SEDs were explained above, a modified version of HyperZ is used to fit GROND SEDs, and XSPEC v12 is used to fit XRT spectra. However, data from both instruments can be used together to create a broad-band SED, which allows us to study a large portion of the afterglow spectrum. To do this, time intervals of the light curve, in which the broad-band SEDs will be constructed, are first selected. The interval mid-times are selected based on the "interesting" parts of the light curve, usually covering every different segment of the temporal evolution of the afterglow flux. After obtaining XRT spectral data from the repository and GROND data from the analysis, both described above, the XRT data are re-normalized so that the mean photon arrival time for the XRT spectrum is equal to the mid-time of the GROND observation (TDP, OB or stacked image). In principle, only one XRT time-average spectrum can be used together with all GROND SEDs in case that XRT spectrum does not change in time, which can be easily verified by checking the hardness ratio of XRT data in the repository. This one XRT spectrum can then be re-normalized and used several times based on mid-times of GROND SEDs with which they are combined. However, in this thesis, XRT data with the closest possible mean photon arrival time to the mid-time of selected GROND mid-time are used to avoid any conclusions based on assumptions rather than on hard evidence represented by observed data. While mid-times of optical and NIR bands of GROND observations differ due to dissimilar readout times of the detectors, the differences are in order of seconds and are therefore neglected.

After re-normalizing each XRT spectrum to the mid-time of the GROND SED with which it should be combined, the GROND magnitudes are converted into the XSPEC format and fitted together with the XRT data. Only two types of models are used in this thesis: simple power-law and a broken power-law, both with the addition of the absorbing hydrogen column densities used for the X-ray part. The break in the broad-band SED between GROND and XRT data represents on of the typical synchrotron frequencies, namely ν_m in the fast cooling regime or ν_c in the more commonly observed slow cooling regime. When fitting the simple power-law to the broad-band data, the output of XSPEC is the same as in the case of the XRT fit alone but the spectral

slope β is much better defined thanks to larger wavelength range. In case of the broken power-law model, the value of the break frequency is obtained in addition to low- and high-energy spectral indices (Fig. 4.6). Only a sharply broken power-law model (Fig. 4.5) is available by default so for purposes of our research, we added a smoothly broken power-law model (Fig. 4.6) to XSPEC. The formula (Eq. 4.1) is similar to the one used in the light curve fitting but with frequency in place of the time parameter. Similar to light curve fit script, XSPEC calculates χ^2 statistics of the fit, 1σ errors of all free parameters and residuals of datapoints to the fitted model.
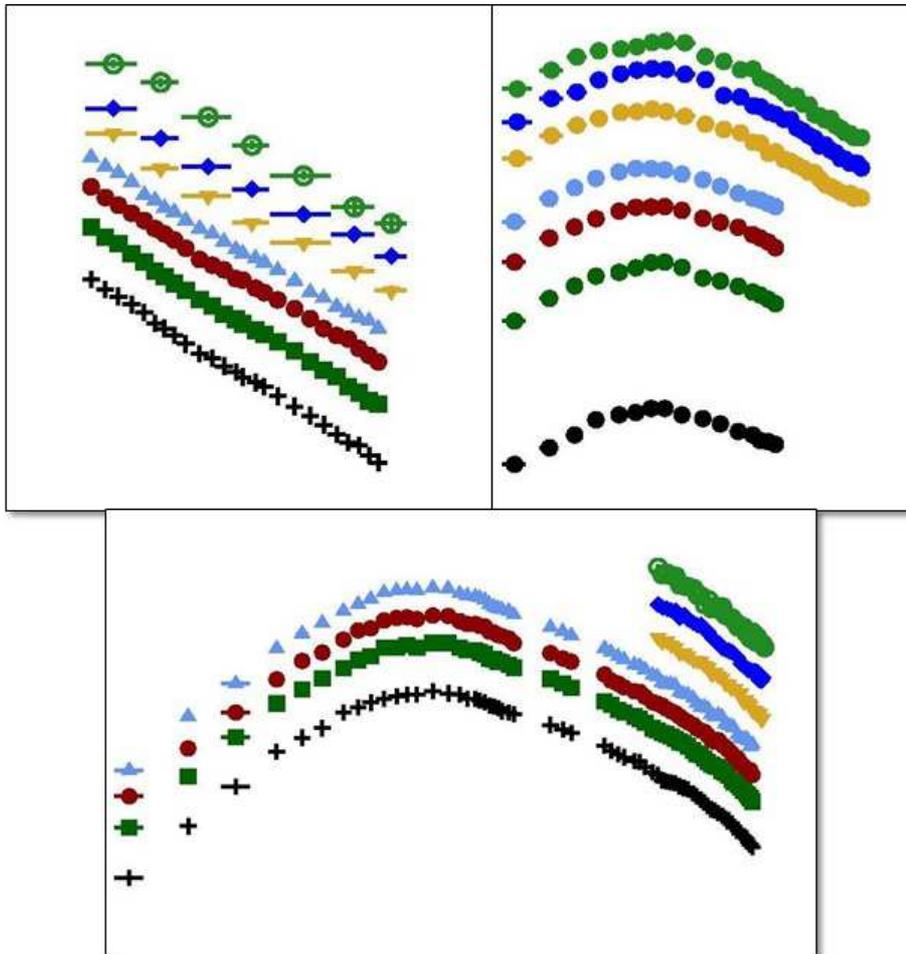
Figure 2.8 Image showing different types of difficulties in the automatic SED fitting. Top left are the GROND data with different exposure length in NIR channels (top three) and optical channels (lower four). Top right are the GROND data with NIR-only coverage at the end due to the dawn. Bottom image shows an opposite situation, where NIR channels were not working from the start due to HW fault.

2.3.5 Evolution of the spectral index

The study of the temporal evolution of the synchrotron frequencies yields an important role in the GRB afterglow research (see Chapter 4). However, while the modelling of broad-band SEDs provides accurate results, it is time-consuming and the temporal resolution is highly dependent on the X-ray count-rate of the source. In order to simplify a selection process of prime candidates for the broad-band fitting in the large GROND sample (> 100 detected bursts), a HyperZ wrapper was designed and coded, which fits every GROND SED present in the afterglow light curve. The light curves where NIR magnitudes are obtained from the images with different exposure length than optical images needed a special approach. It is for example quite common that NIR images are the result of analysis of whole OBs, while the optical images are just from individual TDPs (Chapter 3, 4 and 5). In such cases, the four magnitudes in each optical band were interpolated to a one value with the mid-time same as data in NIR (Fig. 2.8). In case magnitudes in one or more filters are missing, the spectral index is computed by fitting the remaining bands. This analysis allows the user to measure the optical/NIR spectral index as a function of time with high temporal resolution (Fig. 4.4). Given that the spectral index in X-rays almost never changes, the measurement of the changes in the optical/NIR spectral index can provide a reliable hint on the evolution of the synchrotron frequency between the two wavelengths.

Chapter 3

The two-component jet of GRB 080413B[1]

ABSTRACT

The quick and precise localization of GRBs by the *Swift* telescope allows the early evolution of the afterglow light curve to be captured by ground-based telescopes. With GROND measurements we can investigate the optical/near-infrared light curve of the afterglow of gamma-ray burst 080413B in the context of late rebrightening. Multi-wavelength follow-up observations were performed on the afterglow of GRB 080413B. X-ray emission was detected by the X-ray telescope onboard the *Swift* satellite and obtained from the public archive. Optical and near-infrared photometry was performed with the seven-channel imager GROND mounted at the MPG/ESO 2.2 m telescope and additionally with the REM telescope, both in La Silla, Chile. The light curve model was constructed using the obtained broad-band data. The broad-band light curve of the afterglow of GRB 080413B is well fitted with an on-axis two-component jet model. The narrow ultra-relativistic jet is responsible for the initial decay, while the rise of the moderately relativistic wider jet near its deceleration time is the cause of the rebrightening of the light curve. The later evolution of the optical/NIR light curve is then dominated by the wide component, the signature of which is almost negligible in the X-ray wavelengths. These components have opening angles of $\theta_n \sim 1.7°$ and $\theta_w \sim 9°$, and Lorentz factors of $\Gamma_n > 188$ and $\Gamma_w \sim 18.5$. We calculated the beaming-corrected energy release to be $E_\gamma = 7.9 \times 10^{48}$ erg.

3.1 Introduction

Gamma-ray burst (GRB) afterglows are commonly interpreted in the framework of the standard synchrotron shock model, in which an ultra-relativistic shock is expanding

into the ambient medium swept up by the blast wave (Mészáros, 2002; Zhang and Mészáros, 2004; Piran, 1999). For the simplified assumption that the shock front is spherical and homogeneous, a smooth afterglow light curve is expected. This smooth power-law decay with time was a common phenomenon in most of the pre-*Swift* GRBs (Laursen and Stanek, 2003), because the afterglow observations typically began ∼1 day after the burst compared to now when we can be on-target within minutes.

The *Swift* satellite (Gehrels et al., 2004) allows studies of the early afterglow phase thanks to its rapid slew, a precise localization of GRBs with its Burst Alert Telescope (BAT, Barthelmy et al., 2005), and the early follow-up with two telescopes sensitive at X-ray (XRT, Burrows et al., 2005b) and ultraviolet/optical (UVOT, Roming et al., 2005) wavelengths. Since its launch in 2004, *Swift*, together with ground-based follow-up telescopes, has provided many early and well-sampled afterglow light curves deviating from the smooth power-law decay (Panaitescu et al., 2006a; Nousek et al., 2006; Zhang et al., 2006; Panaitescu et al., 2006b). Such variability can shed light on the central engine and its surroundings.

Several major scenarios have been proposed for afterglow variability. The reverse shock emission might add to the emission from the forward shock (see §4.1, Sari and Piran, 1999b; Meszaros and Rees, 1993a; Zhang et al., 2003; Kobayashi and Zhang, 2003a), the shock might be refreshed by slower shells catching up with the decelerating front shells (see §4.2, Rees and Meszaros, 1998; Panaitescu, 2005; Sari and Mészáros, 2000; Panaitescu et al., 1998; Granot et al., 2003; Kumar and Piran, 2000), the ambient density profile into which the blast wave expands might not be homogeneous (see §4.3 Lazzati et al., 2002; Nakar et al., 2003; Zhang et al., 2006; Nakar and Piran, 2003; Ioka et al., 2005; Wang and Loeb, 2000; Dai and Lu, 2002; Nakar and Granot, 2007), or the jet may have an angular structure different from a top hat (see §4.4, Peng et al., 2005; Granot et al., 2006; Berger et al., 2003; Racusin et al., 2008).

Here we provide details of the *Swift*, GROND, and REM observations of the afterglow of GRB 080413B and test the above alternative scenarios for consistency with these data. Throughout the paper, we adopt the convention that the flux density of the GRB afterglow can be described as $F_\nu(t) \propto t^{-\alpha}\nu^{-\beta}$. Unless stated otherwise in the text, all reported errors are at 1σ confidence level.

3.2 Observations

3.2.1 Swift

The *Swift*/BAT triggered by the long GRB 080413B at $T_0 = 08{:}51{:}12$ UT started slewing to the burst after 70 seconds (Stamatikos et al., 2008). The mask-weighted light curve shows a single FRED-like peak starting at $T_0 - 1.1$ s, peaking at $T_0 + 0.2$ s, and returning to baseline at $\sim T_0 + 30$ s. The measured T_{90} (15-350 keV) is 8.0 ± 1.0 s (Barthelmy et al., 2008). The BAT prompt emission spectrum was fitted using the Band function with a photon index of $\alpha = -1.24 \pm 0.26$ and an $E_{\mathrm{peak}} = 67^{+13}_{-8}$ keV (Krimm et al., 2009). By integrating the GRB spectrum using the Band function, we estimate

the event fluence in the 15-150 keV energy range to be $3.1 \pm 0.12 \times 10^{-6}$ erg/cm^2 (Krimm et al., 2009). With a standard concordance cosmology ($H_0 = 71.0$ km/s/Mpc, $\Omega_M = 0.27$, $\Omega_\Lambda = 0.73$, (Komatsu et al., 2009)), and a redshift of $z = 1.1$ (Fynbo et al., 2009), the bolometric (1keV - 10MeV) energy release of GRB 080413B is $E_{\mathrm{iso}} = 1.8 \times 10^{52}$ erg, with a rest-frame E_{peak} of ~ 150 keV. The difference between this value and the value in Krimm et al. (2009) is only due to different set of cosmological parameters used.

The *Swift*/XRT started observations of the field of GRB 080413B 131.2 s after the trigger (Stamatikos et al., 2008; Troja and Stamatikos, 2008). XRT data were obtained from the public *Swift* archive and reduced in the standard manner using the xrtpipeline task from the HEAsoft package, with response matrices from the most recent CALDB release. The XRT light curve was obtained from the XRT light curve repository (Evans et al., 2007, 2009a). Spectra were grouped using the grppha task and fitted with the GROND data in XSPEC v12 using χ^2 statistics. The combined optical/X-ray spectral energy distributions were fitted with power-law and broken power-law models and two absorbing columns: one Galactic foreground with a hydrogen column of $N_H = 3.1 \times 10^{20}$ cm^{-2} (Kalberla et al., 2005) and another one that is local to the GRB host galaxy at $z = 1.1$. Only the latter was allowed to vary in the fits. To investigate the dust reddening in the GRB environment, the zdust model was used, which contains Large and Small Magellanic Clouds (LMC, SMC) and Milky Way (MW) extinction laws from Pei (1992).

3.2.2 REM

The Rapid Eye Mount (REM, Zerbi et al., 2001) 60 cm robotic telescope, located at the ESO La Silla observatory (Chile), reacted promptly and began observing GRB 080413B on April 13 08:52:13 UT, about 76 s after the GRB trigger time. A transient source was detected both in the R and H bands, and follow–up observations lasted for ~ 1 hr. The afterglow is well detected only up to about 300 s, then its brightness falls below the instrument detection limits in both filters.

Each single H-band observation was performed with a dithering sequence of five images shifted by a few arcsec. These images are automatically elaborated using the jitter script of the eclipse (Devillard, 1997) package. The script aligns the images and co-adds all the frames to obtain one average image for each sequence. The R-band images were reduced using standard procedures. A combination of the IRAF[2], and Sextractor packages (Bertin and Arnouts, 1996) were then used to perform aperture photometry.

The photometric calibration for the H band was accomplished by applying average magnitude shifts to the ones of bright, isolated, unsaturated stars in the field, as reported in the 2MASS catalog. The optical data were calibrated using instrumental zero points, checked with observations of standard stars in the SA96 Landolt field (Landolt, 1992).

---

[2]IRAF is the Image Reduction and Analysis Facility made available to the astronomical community by the National Optical Astronomy Observatories, which are operated by AURA, Inc., under contract with the U.S. National Science Foundation. It is available at `http://iraf.noao.edu/`

All data were then cross-calibrated using GROND photometry to obtain consistent results.
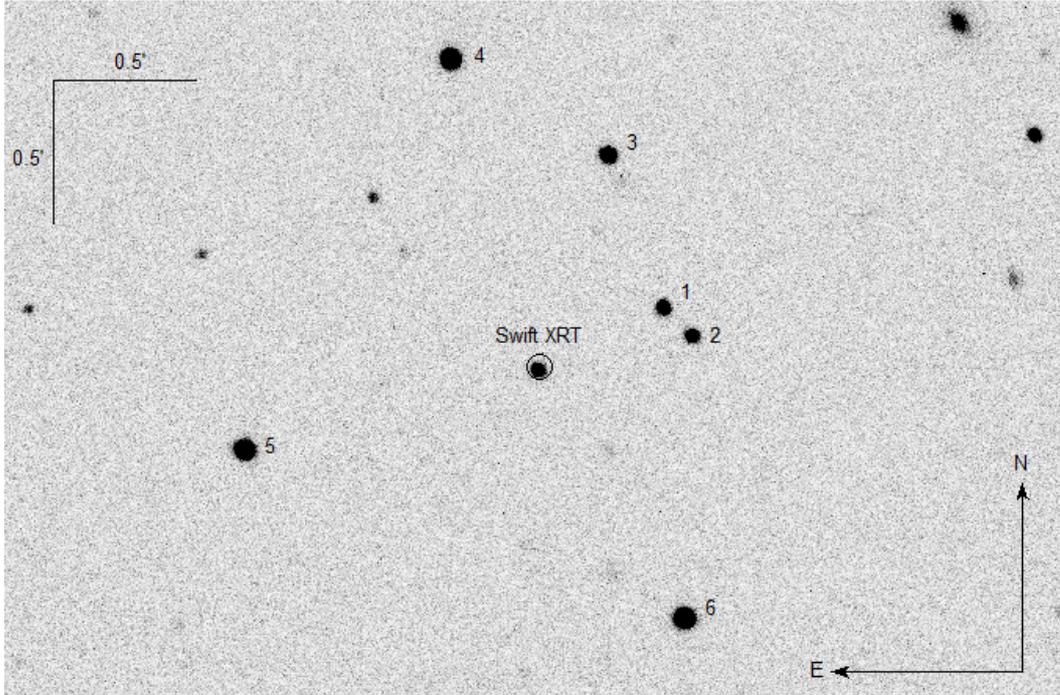
Figure 3.1 GROND r' band image of the field of GRB 080413B obtained 342 s after T_0. The optical afterglow is shown inside the *Swift* XRT error circle. The secondary standard stars are numbered from 1 to 6 and their magnitudes reported in Table 3.1.

3.2.3   GROND

The Gamma-Ray burst Optical Near-infrared Detector (GROND, Greiner et al., 2008, 2007) responded to the *Swift* GRB alert and initiated automated observations at 08:56 UT, 5 minutes after the trigger. A predefined sequence of observations with successively increasing exposure times was executed and images were acquired in the seven photometric bands ($g'r'i'z'JHK_s$) simultaneously. The observations continued for two months, and the last of ten epochs was acquired on June 11th, 2008. In total, 191 CCD optical individual frames in each $g'r'i'z'$ and 2718 NIR images of 10 s exposures in JHK_s were obtained. The CCD integration time scaled from 45 to 360 s according to the brightness of the optical afterglow.

A variable point source was detected in all bands (Kruehler et al., 2008) by the automated GROND pipeline (Yoldaş et al., 2008). The position of the transient was calculated to be R.A. (J2000) = 21:44:34.67 and Dec (J2000) = −19:58:52.4 compared to USNO-B reference field stars (Monet et al., 2003) with an astrometric uncertainty of $0.''3$. The afterglow was also observed and detected by the Faulkes Telescope South

Table 3.1 Secondary standards in the GRB 080413B field in the GROND filter bands used for the calibration

Star number	R.A., Dec [J2000]	g' (mag$_{AB}$)	r' (mag$_{AB}$)	i' (mag$_{AB}$)	z' (mag$_{AB}$)
1	21:44:32.81, −19:58:39.4	18.05 ± 0.03	17.14 ± 0.03	16.93 ± 0.03	16.70 ± 0.03
2	21:44:32.38, −19:58:45.1	18.90 ± 0.03	17.33 ± 0.03	16.08 ± 0.04	15.40 ± 0.03
3	21:44:33.65, −19:58:07.7	17.25 ± 0.03	16.59 ± 0.03	16.47 ± 0.03	16.29 ± 0.03
4	21:44:35.98, −19:57:47.9	16.41 ± 0.03	15.45 ± 0.03	15.15 ± 0.03	14.88 ± 0.03
5	21:44:38.98, −19:59:09.2	16.26 ± 0.03	15.49 ± 0.03	15.28 ± 0.03	15.08 ± 0.03
6	21:44:32.50, −19:59:44.2	16.10 ± 0.03	15.34 ± 0.03	15.19 ± 0.03	14.99 ± 0.03

Star number	R.A., Dec [J2000]	J (mag$_{Vega}$)	H (mag$_{Vega}$)	K_s (mag$_{Vega}$)
1	21:44:32.81, −19:58:39.4	15.75 ± 0.05	15.20 ± 0.05	15.03 ± 0.06
2	21:44:32.38, −19:58:45.1	14.11 ± 0.05	13.49 ± 0.05	13.23 ± 0.06
3	21:44:33.65, −19:58:07.7	15.46 ± 0.05	15.00 ± 0.05	14.82 ± 0.06
4	21:44:35.98, −19:57:47.9	13.87 ± 0.05	13.37 ± 0.05	13.15 ± 0.06
5	21:44:38.98, −19:59:09.2	14.13 ± 0.05	13.57 ± 0.05	13.42 ± 0.06
6	21:44:32.50, −19:59:44.2	14.19 ± 0.06	13.53 ± 0.05	13.52 ± 0.06

(Gomboc et al., 2008) and Skynet/PROMPT (Brennan et al., 2008), and spectroscopy was obtained with the GMOS spectrograph on Gemini-South (Cucchiara et al., 2008) and FORS1 on VLT (Vreeswijk et al., 2008), both determining a redshift of 1.10.

The optical and NIR image reduction and photometry were performed using standard IRAF tasks (Tody, 1993) similar to the procedure described in detail in Krühler et al. (2008). A general model for the point-spread function (PSF) of each image was constructed using bright field stars and fitted to the afterglow. In addition, aperture photometry was carried out, and the results were consistent with the reported PSF photometry. All data were corrected for a Galactic foreground reddening of $E_{B-V} = 0.04$ mag in the direction of the burst (Schlegel et al., 1998), corresponding to an extinction of $A_V = 0.11$ using $R_V = 3.1$, and in the case of JHK_s data, transformed to AB magnitudes.

Optical photometric calibration was performed relative to the magnitudes of six secondary standards in the GRB field, shown in Fig. 3.1 and Table 3.1. During photometric conditions, a spectrophotometric standard star, SA112-223, a primary SDSS standard (Smith et al., 2002), was observed within a few minutes of observations of the GRB field. The obtained zeropoints were corrected for atmospheric extinction and used to calibrate stars in the GRB field. The apparent magnitudes of the afterglow were measured with respect to the secondary standards reported in Table 3.1. The absolute calibration of JHK_s bands was obtained with respect to magnitudes of the Two Micron All Sky Survey (2MASS) stars within the GRB field obtained from the 2MASS catalog (Skrutskie et al., 2006).

Table 3.2 GRB 080413B afterglow light curve fit (χ^2/d.o.f. $= 462/429$) with smoothness, break-time, and power-law slope parameters for both components.

$F_\nu(t)$	α_1	$t_1[ks]$	s_1	α_2	$t_2[ks]$	s_2	α_3
DPL[a]	0.73 ± 0.01	3.9 ± 0.2	10	1.39 ± 0.05			
TPL[b]	-0.55 ± 0.05	37.0 ± 2.8	2	0.95 ± 0.02	332.4 ± 11.4	10	2.75 ± 0.16

[a] Smoothly connected double power-law

[b] Smoothly connected triple power-law

3.3   Results

3.3.1   Afterglow light curve

The optical/NIR light curve (Fig. 3.2) of the afterglow of GRB 080413B shows an initial decay with a temporal slope $\alpha = 0.73 \pm 0.01$, followed by a flattening starting at roughly 1 ks. Despite the lack of data between 5 and 90 ks, a comparable brightness at the beginning and at the end of the gap (chromatic fading from ~ 0.8 mag in the g' band to ~ 0.2 mag in the K_s band) suggests a plateau. The light curve then resumes the decay with a steeper temporal slope of $\alpha = 0.95 \pm 0.02$ until an achromatic break at roughly 330 ks. Owing the achromacity, time, and sharp steepening of the decay, we assume this to be a jet break. After this break the afterglow fades with a steep decay of $\alpha = 2.75 \pm 0.16$. The flattening at the end ($> T_0 + 1$ Ms) of the light curve suggests a faint host galaxy.

The X-ray light curve shows a different evolution. The initial decay has the same temporal slope as the optical/NIR light curve, but the later plateau phase is missing completely. The time of the break at ~ 330 ks and the decay index after this break is adopted from the optical/NIR data as the X-ray flux does not provide strong constraints in this part of the X- ray light curve.

Both light curves were jointly fitted with an empirical model consisting of three components (see Fig 3.3). The first component is composed of two smoothly connected power-laws. The second component was needed to model the later rebrightening and uses three smoothly connected power-laws. The flattening in the latest part was modeled with a constant flux. As a result of the high accuracy of the data and good sampling in the time domain, most parameters were left free to vary and are presented in Table 3.2.

The only fixed parameters were the smoothnesses s of all breaks connecting the power-laws and the flux of the host galaxy in filters without a detection in the latest flattening phase (i', z', J, H, and K_s). The smoothness was fixed to a value of $s = 10$ in two cases where the power-law decay was steepening in order to be consistent with the smoothness of a jet break (Zeh et al., 2006) and to a value of $s = 2$ in the place of the peak of the second component. The flux of the host was fixed to values that assume an achromatic afterglow evolution, though this is probably not quite correct, as the host is expected to have different colors than the afterglow.

The optical/NIR light curve (Fig. 3.2) of the afterglow of GRB 080413B can be
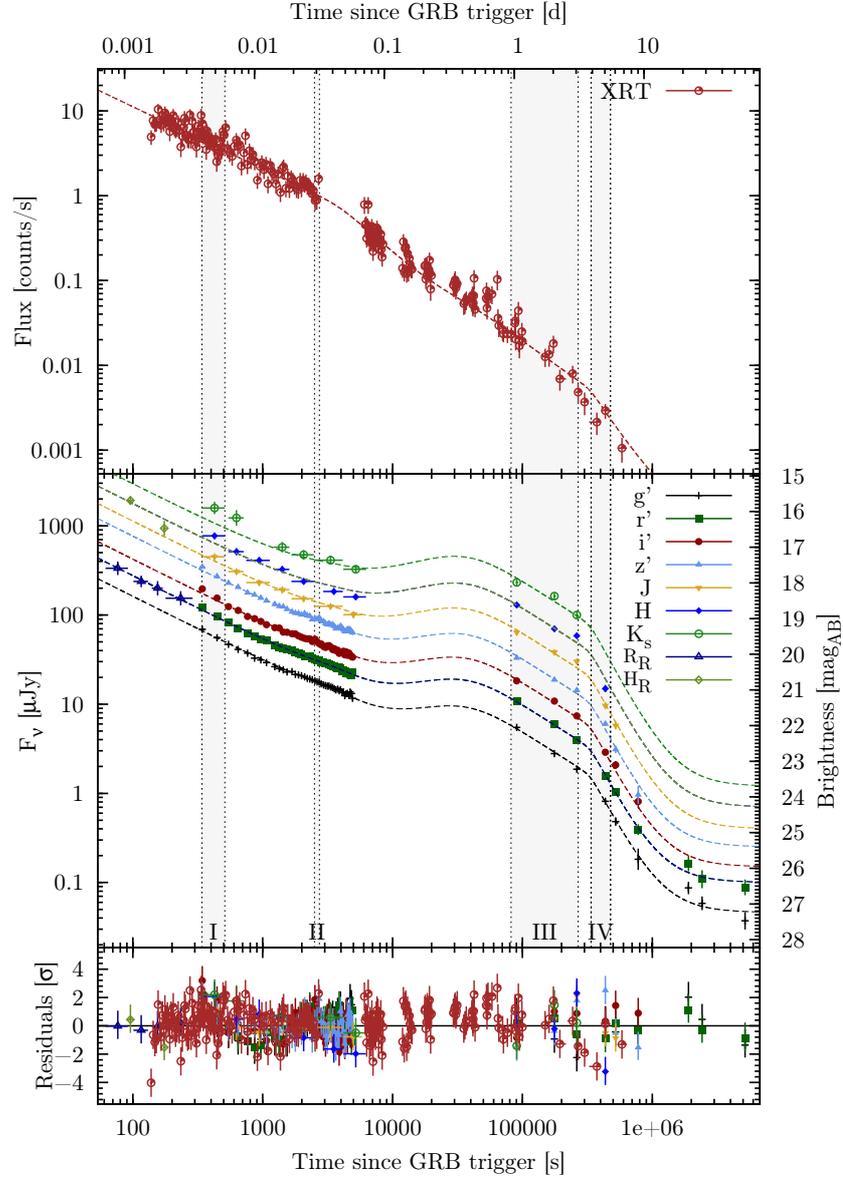
Figure 3.2 Light curve of the X-ray (top panel) and optical/NIR (middle panel) afterglow of GRB 080413B. Bands are offset by $g' + 2, r' + 1.5, i' + 1, z' + 0.5, H - 0.5, K_s - 1$ mag, and REM data R_R and H_R have offsets corresponding to GROND data. The bottom panel shows residuals to the combined light curve fit. Shown data are corrected for the Galactic foreground extinction and transformed into AB magnitudes. Upper limits are not shown for better clarity. Gray regions show the time intervals where SEDs are reported (Fig. 3.4).
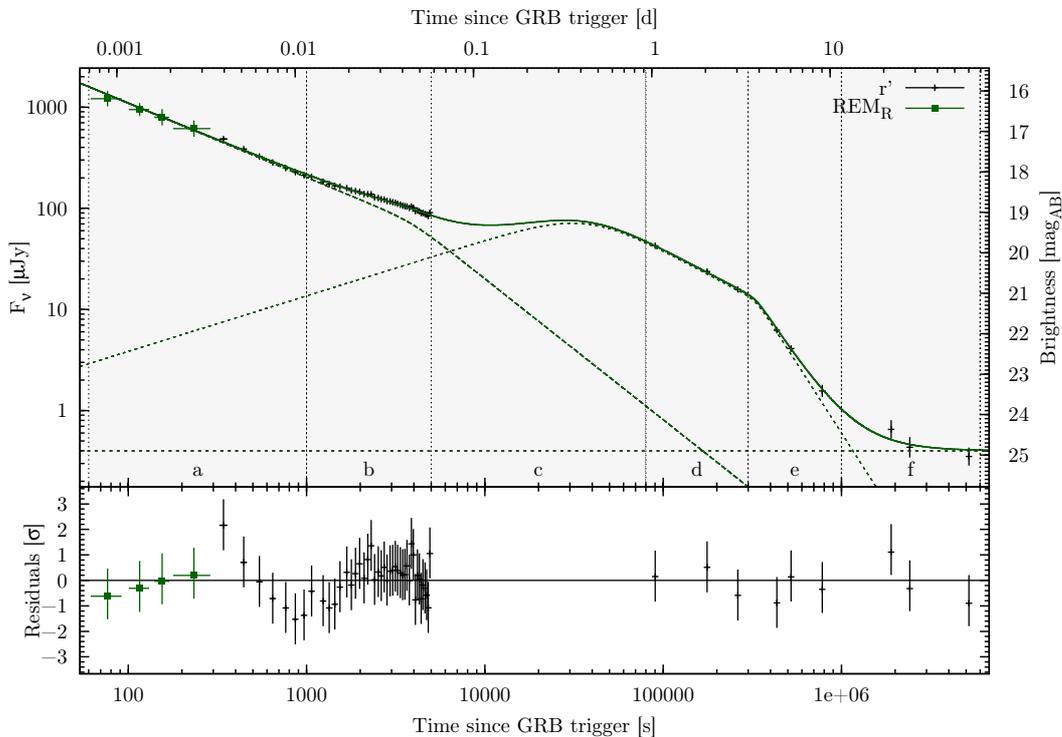
Figure 3.3 Three-component fit for GRB 080413B as the superposition of the afterglow emission from the two jets and the host. Shown are the GROND r' and REM R band data, with all other bands omitted to enhance clarity. The additional systematic structure in the residuals between 300 s and 5000 s could be additional small-scale variability, which we ignore here.

divided into six segments a, b, c, d, e, and f, based on the temporal indices shown in Fig. 3.3. We assign segment a to the first, and segments c, d, e to the second component. Segment a is the prompt decay dominated by the first component. In segment b we see the rising influence of the second component, which then dominates the rest of the later optical light curve and peaks in the third segment c. The best fit in the segment c is a plateau-like evolution without any sharp flares. Though we have no data points in this segment, magnitudes from Gomboc et al. (2008) are in good agreement with this interpretation. Segments d and e are fully dominated by the second component with segments e and f showing the rising influence of the constant flux, which we interpret as the host galaxy. This host galaxy was detected in the g' and r' bands, but the stellar mass is not constrained by the optical identification obtained by GROND because observations probe the rest-frame wavelengths below the 4000 Åbreak, where the mass-to-light ratio can vary by a factor of more than 100. The X-ray light curve shows a significantly different evolution, mainly due to a much lower contribution from the second component to the total flux. The absence of the rebrightening part gives evidence of the flux from the second component being stronger in optical wavelengths and nearly

negligible in X-rays. This suggests a different physical origin for each component.
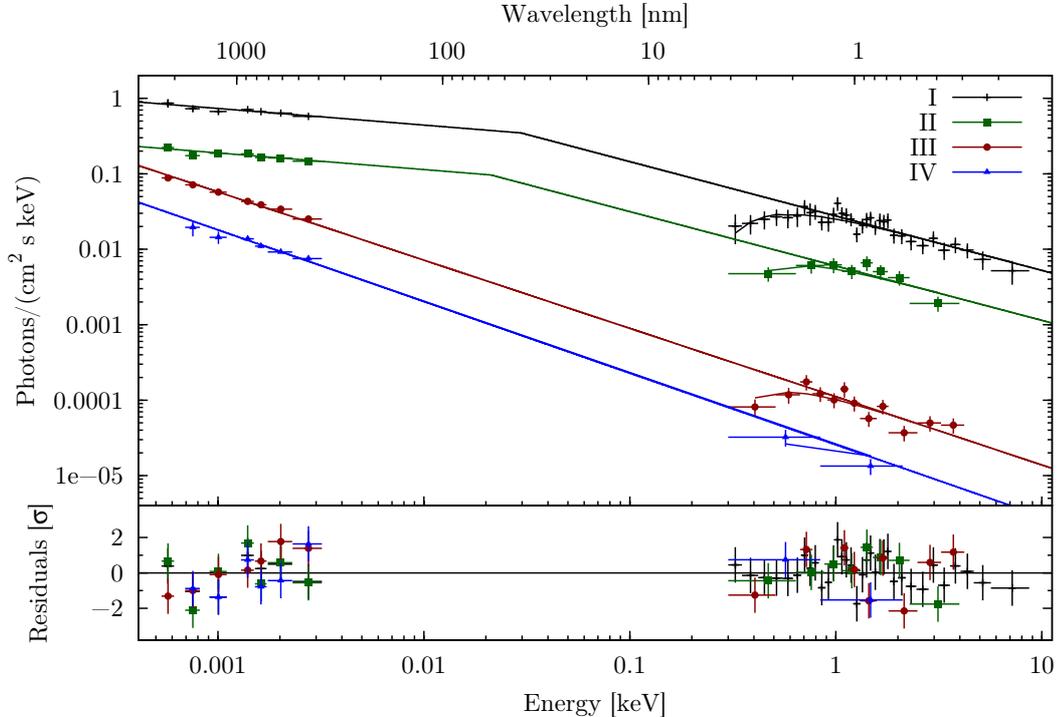
Figure 3.4 Broad-band spectral energy distribution using the X-ray and optical/NIR data at four epochs indicated in Fig. 3.2. The data were fitted using a power-law, modified by a Galactic and intrinsic hydrogen column.

3.3.2   Broad-band spectrum

The afterglow spectrum can be parameterized over a broad wavelength range using X-ray, optical, and NIR data. Broad-band spectral energy distributions (SED, Fig. 3.4) were constructed at four different time intervals, which are indicated in the light curve (Fig. 3.2). Fit parameters of these SEDs are presented in Table 3.3.

As already evident from the lack of the plateau phase in the X-ray light curve, there is a spectral evolution between data from the time intervals II and III. The two last optical/NIR SEDs (III and IV) are consistent with a power-law with a spectral index consistent with the X-ray spectral index without strong signatures of any curvature. There is also no evidence of any spectral evolution between SEDs before and after the break at 330 ks, providing more evidence of an achromatic jet break. Both the optical/NIR and X-ray emission in these two latest phases probe the same segment of the afterglow synchrotron spectrum with a spectral slope $\beta \sim 0.92$.

SEDs of phases I and II show evidence of a synchrotron cooling break between the X-ray and optical/NIR frequencies. We fixed the difference in values between optical/NIR

Table 3.3 GRB 080413B SED fits of four epochs using X-ray and optical/NIR data

Epoch	Optical/NIR β	X-ray β	ν_c [eV]	N$_H^{(a)}$ [10^{22} cm^{-2}]	χ^2/d.o.f
I	0.22 ± 0.08	0.72 ± 0.08	$29.6^{+10.4}_{-24.2}$	0.16 ± 0.12	24/36
II	0.22 ± 0.04	0.72 ± 0.04	$21.1^{+26.7}_{-12.0}$	0.16 (frozen)	16/12
III	0.90 ± 0.05			0.16 (frozen)	23/17
IV	0.95 ± 0.05			0.16 (frozen)	10/6

[a]   Intrinsic hydrogen column density, in excess of the frozen Galactic foreground of $N_{\mathrm{H}} = 3.1 \times 10^{20}$ cm^{-2}.

and X-ray spectral indices to 0.5 (as predicted by the standard fireball model; Sari et al. (1998)) but the values come from the fitting. This produced a cooling break that showed a slight drift to lower frequencies with time. However, the error on the cooling break frequency is too large to claim any trend, and the cooling break is therefore consistent with being constant as well. We note that this possible cooling break passage through the optical/NIR bands cannot be the cause of rebrightening as it would have the opposite effect, i.e. a steepening of the decay (Sari et al., 1998).

3.3.3   Closure relations

The optical/NIR temporal index $\alpha = 0.73 \pm 0.01$ of the segment a is consistent within 3σ errors with the closure relations (Granot and Sari, 2002; Dai and Cheng, 2001; Zhang and Mészáros, 2004; Racusin et al., 2009) for a normal decay in the $\nu_m < \nu < \nu_c$ regime, where the jet is interacting with a homogeneous ISM and is in the slow cooling phase. The corresponding power-law index of electron energy distribution $p = 1.44 \pm 0.16$ is very hard. The X-ray temporal and spectral slopes in the segment a are inconsistent with any closure relations. While the spectral slope is different from that in the optical/NIR wavelengths, the temporal slopes are similar.

The temporal index $\alpha = 1.39 \pm 0.05$ of the second power-law of the first component after the break is within 1σ consistent with the closure relations for a post-jet break decay in the $\nu_m < \nu < \nu_c$ regime, where the jet is interacting with a homogeneous ISM and does not spread. The X-ray slopes are again inconsistent with any closure relations.

The initial decay of the second component in segment d with an index of 0.95 ± 0.02 is consistent (within 1σ) with the closure relations for the normal (pre-jet break) decay in the $\nu > \nu_c$ regime for a homogeneous ISM and slow cooling case. The corresponding electron energy distribution index $p = 1.84 \pm 0.32$ is still rather hard but closer to the values typical of GRBs. The late temporal decay is not constrained well by the data, but it is relatively steep and consistent with being achromatic. Fixing the break to be rather sharp (Zeh et al., 2006) results in a decay with a temporal index of $\alpha \sim 2.8$, indicative of a post jet break evolution and a break time of roughly 330 ks. This light curve slope, however, is not consistent with any closure relation, which might be, at

least partially, the result of the parameter fixing in the light curve fitting.

3.4   Discussion

Rebrightenings of the afterglow light curves are generally associated with density inhomogeneities in the circumburst medium or with different forms of late energy injections. In this section we discuss various possible models for interpreting the optical/NIR rebrightening and conclude that the data require the two-component jet model to explain all the light curve features.

3.4.1   Reverse shock emission

When the relativistic shell of the fireball ejecta encounters the interstellar medium, the reverse shock propagates back into the shocked material and can produce a bright optical flash (Sari and Piran, 1999b; Meszaros and Rees, 1993a). This emission peaks very early, before the emission from the forward shock, and has a steep temporal decay index $\alpha \sim 2$ (Zhang et al., 2003; Kobayashi and Zhang, 2003a). The reverse shock is therefore inconsistent with being the source of the late emission during the plateau phase in segment c since this emission peaks at several hours after the burst. A second scenario would be that the initial light curve emission in segment a was the reverse shock component decay and the later plateau was the result of the forward shock emission reaching a peak followed by its slow decay, which would then dominate the later light curve (segments c, d, e). However, the shallow temporal index during the initial decay in segment a is incompatible with emission from a reverse shock. The light curve of the afterglow is therefore incompatible with emission from reverse shocks.

3.4.2   Refreshed shock emission

Refreshed shocks are produced when slower shells with a lower Lorentz factor catch up with the afterglow shock at late times (Rees and Meszaros, 1998; Panaitescu, 2005; Sari and Mészáros, 2000; Panaitescu et al., 1998). Each collision then causes a rebrightening in the afterglow light curve. After the rebrightening, the afterglow resumes its original decay slope (Granot et al., 2003). However, these rebrightenings are generally achromatic (Kumar and Piran, 2000) as the slow shell reenergizes the forward shock, which is responsible for both X-ray and optical emission. Therefore, a refreshed shock could not create the chromatic rebrightening in the light curve of the afterglow after the initial decay. Different temporal indices before and after this event moreover exclude refreshed shocks as a feasible explanation for the evolution of the light curve.

3.4.3   Inhomogeneous density profile of the ISM

Variations in the external density provide a possible explanation for the temporal variability of the GRB afterglow light curves within the external shock framework (Lazzati et al., 2002; Nakar et al., 2003; Zhang et al., 2006; Nakar and Piran, 2003;

Ioka et al., 2005; Wang and Loeb, 2000; Dai and Lu, 2002). Such variations might be the result of the interstellar medium turbulence or variability in the winds from the progenitor. The first case might be characterized by either an abrupt change in the radial density or density clumps on top of a smooth background. The latter can be a case of the wind termination shock, which is an abrupt increase in the radial density between wind environments of two evolutionary stages of the massive progenitor. Models suggest that these inhomogeneities will have a clear observational signature in the form of the optical afterglow light curve rebrightening.

The initial decay of the light curve of GRB 080413B is a smooth power-law with $\alpha \sim 0.7$. At $T \sim 0.12$ d α becomes negative over a factor $\sim 2 - 3$ in time. According to Nakar and Granot (2007) and van Eerten et al. (2009), such a large $\delta\alpha$ over a relatively small factor in time is not expected from variations in the external density. Even though our temporal index during the rebrightening is based on the fit alone, real data before and after this gap show that a smooth power law connected with very sharp breaks and with a temporal index very near zero would be needed to connect these data points without a rebrightening with a peak. While the wind termination shock could explain the lack of the rebrightening feature in X-ray band, the expected decrease in temporal index above the cooling frequency is too small to be compatible with our optical light curve.

3.4.4 Two-component jet

The generic two-component jet model consists of a narrow and highly relativistic jet, responsible for the prompt afterglow emission, and of a wider and moderately relativistic jet, dominant in the later afterglow emission (Peng et al., 2005; Granot et al., 2006; Berger et al., 2003; Racusin et al., 2008). For an on-axis geometry, the resulting afterglow light curve is a superposition of these two components, where the decelerating narrow jet creates the initial decay and the wide jet dominates the later emission that rises during the pre-deceleration phase, followed by the shallow decay with a possible jet break. The relative energies and jet structure then define the light curve morphology.

The light curve is well-fitted (red. $\chi^2 = 1.08$) with the sum of the two components that we relate to the two afterglow jets, where both are viewed on-axis and are coaxial. The initial shallow decay phase of segment a could be the result of the emission of the decelerating narrow jet. Given that we do not see any rising part in the early light curve and that even the very early data from the REM telescope have the same decay slope as the later GROND data, we can safely assume that we see the narrow jet on-axis. From the time of the jet break at around 3.9 ks, we can calculate the opening angle (Sari et al., 1999) of the narrow jet as $\theta_n \sim 1.7°$, substituting the measured quantities and normalizing to the typical values $n = 1$ cm^{-3} and $\eta = 0.2$ (Bloom et al., 2003). Assuming the time of the first R' band data point to be upper limit on the time of the emission peak, we calculate the initial Lorentz factor (Molinari et al., 2007) to be $\Gamma_n > 188$. These values lead to the beaming factor and the true gamma-ray energy release (Frail et al., 2001; Bloom et al., 2003) of $f_b = (1 - \cos\theta_{jet}) = 4.4 \times 10^{-4}$ and

$E_{\gamma,n} = 7.9 \times 10^{48}$ erg.

The wide-jet component might be responsible for the rebrightening starting at around 10 ks. However, this second component is visible even earlier in the initial decay phase, where the light curve gets shallower (segment *b*). The initial rising of the flux is compatible with the jet decelerating in the circumburst medium. The wide jet is therefore seen on-axis as well, and both jets can be considered coaxial. The jet break at roughly 330 ks indicates an opening angle of the wide jet of $\theta_w \sim 9°$. The initial Lorentz factor, corresponding to the peak of the second jet at 37 ks, is then $\Gamma_w \sim 18.5$.

3.5 Conclusions

In this paper we study the optical/NIR light curve produced by the afterglow of GRB 080413B. The possibility that the jet of this GRB might have a narrow ultra-relativistic core and a wider, mildly relativistic outer component has been indicated by the observation of the afterglow emission. An on-axis coaxial two-component jet model provides a consistent description of the properties of GRB 080413B, and can additionally explain the wide range of light curve evolutions, the difference between optical/NIR and X-ray light curves, and the chromatic evolution of the optical light curve itself.

The comparison with the two most prominent light curves modeled by the two-component jet to date - GRB 050315 and GRB 080319B - reveal consistency with the GRB 080413B afterglow light curve. The X-ray light curve of the afterglow of GRB 050315 (Granot et al., 2006; Nousek et al., 2006) shows a remarkable resemblance to the optical/NIR light curve evolution of the afterglow of GRB 080413B. If we neglect the very steep tail of the prompt GRB emission, the initial XRT light curve of GRB 050315 is dominated by the narrow jet, followed by a slight rebrightening at around 1.5 ks caused by the wide jet in its pre-deceleration phase. After the peak, the light curve decay is dominated by the emission from the wide jet. Times of jet breaks of narrow (~ 9 ks) and wide (~ 200 ks) components, as well as their opening angles $\theta_w = 2\theta_n = 3.2°$ (Granot et al., 2006), are within an order comparable with those of GRB 080413B.

The X-ray light curve of the naked-eye GRB 080319B (Racusin et al., 2008) shows similar evolution. The narrow jet dominates the first ~ 40 ks of the afterglow. After the narrow jet decays, the wide jet dominates the late afterglow. There is no rising part of the wide jet and thus no sharp rebrightening or plateau, so the wide jet merely makes the decay flatter. The optical light curve is missing the emission from the narrow jet, suggesting that the optical flux from the wide jet must be much stronger than that of the narrow jet. The jet break of the narrow jet at ~ 2.8 ks, which corresponds to an extremely narrow opening angle of $0.2°$, is the earliest of these three bursts. The jet break of the wide component with opening angle $\sim 4°$ is, on the other hand, the latest at roughly 1 Ms. In general, the X-ray light curves of GRBs 050315, 080319B and the optical light curve of GRB 080413B are very similar. However, the afterglow of GRB 080413B is the only one showing both components in the optical/NIR wavelengths,

while the emission from the wide jet in the X-rays is negligible. The X-ray flux from the wide jet must then be much less prominent than for the narrow jet.

Following this line of reasoning the relative fluxes in optical/NIR and X-ray of the narrow and wide jets can be explained in the following way. The SED of the narrow jet (intervals I and II) shows a break, while that of the wider jet does not. For both jets we have argued that we cover the slow cooling regime. The spectral slope of the wide component implies that the cooling break is at frequencies below the near-infrared bands. Both the cooling frequency and the maximum power depend on the product of Lorentz factor Γ of the shocked fluid and the magnetic field strength. It is generally assumed that the narrow jet comes with a larger Lorentz factor than the wide one, and a similar assumption can be reasonably made about the (self-created) magnetic field. The SEDs of the two jets show us that the product $\Gamma * B$ of the wide jet, and consequently also the emission at X-ray energies, are at least a factor 100 less than for the narrow one. Therefore, the wide jet does not contribute to the X-ray emission in any significant way. The situation is different in the optical/NIR since cooling break of the narrow jet leads to a reduced flux by a factor of ≈ 10 relative to a spectrum with no cooling break between the optical/NIR and X-rays. Consequently, the optical/NIR emission of the wide jet is much more prominent than for the narrow jet.

The values derived from the modeling of GRB 080413B afterglow are fairly consistent with the collapsar jet breakout model of Zhang et al. (2004), where the numerical simulations predict $\theta_n = 3 - 5°$, $\Gamma_n \gtrsim 100$ for the narrow component and $\theta_w \sim 10°$, $\Gamma_w \sim 15$ for the wide component (Peng et al., 2005). The characteristic Lorentz factors are very similar to those of the hydromagnetically accelerated, initially neutron-rich jet model of Vlahakis et al. (2003), where $\Gamma_n \sim 200$ and $\Gamma_w \sim 15$. These two models are distinguished by the ratio of the kinetic energy injected into the two components. For values typical of the collapsar model ($E_w/E_n \sim 0.1$), Peng et al. (2005) predict that the contribution of the narrow component dominates at all times. However, for $E_w \gtrsim 2E_n$ (as in the neutron-rich hydromagnetic model), the narrow component dominates at early times but the contribution of the wide jet becomes dominant around the deceleration time of the wide jet. If $E_w > E_n$, the jet break of the narrow jet could be masked by the rise (and subsequent dominance) of the flux from the wide jet as the deceleration time of the wide component is approached. That the only visible jet break in the optical light curve is the one of the wide jet may lead to overestimating the emitted gamma-ray energy if the opening angle of the wide jet is used in converting the measured energy into the beaming-corrected energy (see Peng et al. (2005) for detailed discussion). Because the deceleration time of the wide component is much longer than for the narrow component, a bump is expected to show up in the decaying light curve of the narrow component owing the emission of the wide component at its deceleration time. These predictions are in perfect agreement with our data, suggesting that the two-component jet model can be placed among models that explain the variability in the early light curves of the GRB afterglows.

Chapter 4

GRB 091127: The cooling break race on magnetic fuel[1]

ABSTRACT

Using high-quality, broad-band afterglow data for GRB 091127, we investigate the validity of the synchrotron fireball model for gamma-ray bursts, and infer physical parameters of the ultra-relativistic outflow. We used multi-wavelength (NIR to X-ray) follow-up observations obtained with GROND simultaneously in the $g'r'i'z'JH$ filters and the XRT onboard the *Swift* satellite in the 0.3 to 10 keV energy range. The resulting afterglow light curve is of excellent accuracy with relative photometric errors as low as 1%, and the spectral energy distribution is well-sampled over 5 decades in energy. These data present one of the most comprehensive observing campaigns for a single GRB afterglow and allow us to test several proposed emission models and outflow characteristics in unprecedented detail. Both the multi-color light curve and the broad-band SED of the afterglow of GRB 091127 show evidence of a cooling break moving from high to lower energies. The early light curve is well described by a broken power-law, where the initial decay in the optical/NIR wavelength range is considerably flatter than at X-rays. Detailed fitting of the time-resolved SED shows that the break is very smooth with a sharpness index of 2.2 ± 0.2, and evolves towards lower frequencies as a power-law with index -1.23 ± 0.06. These are the first accurate and contemporaneous measurements of both the sharpness of the spectral break and its time evolution. The measured evolution of the cooling break ($\nu_c \propto t^{\sim -1.2}$) is not consistent with the predictions of the standard model, wherein $\nu_c \propto t^{-0.5}$ is expected. A possible explanation for the observed behavior is a time dependence of the microphysical parameters, in particular the fraction of the total energy in the magnetic field ϵ_B. This conclusion provides further evidence that the standard fireball model is too simplistic, and time-dependent micro-physical parameters may be required to model the growing number of well-sampled afterglow light curves.

4.1 Introduction

Gamma-ray bursts (GRBs) are among the most energetic explosions in the universe. The leading model for their afterglows is the synchrotron fireball (Meszaros and Rees, 1997a; Piran, 1999; Mészáros, 2002; Zhang and Mészáros, 2004). In this model, the afterglow arises from the synchrotron emission of shock-accelerated electrons in a fireball interacting with the circum-burst medium. The spectral energy distribution (SED) of such emission is well modeled by several broken power-laws connected at characteristic break frequencies (Sari et al., 1998). The model predicts a break in the light curve when the cooling frequency (ν_c, the frequency of electrons whose radiative cooling time-scale equals the dynamical time of the system) or the characteristic synchrotron frequency (ν_m, peak frequency for the minimal energy of the radiating electrons) passes through the observed bands. Such breaks in the light curve have been, however, difficult to identify reliably as the passage of the above frequencies.

With the development of rapid-response telescopes and multi-wavelength instruments, we expected to detect the movement of the break frequencies. However, this movement has only possibly been observed directly in the afterglow of GRB 080319B (Racusin et al., 2008). Detections of the spectral-break movements in other GRBs were mostly based on the evolution of the GRB afterglow light curves in just one or few filters, where the subtle steepening is visible and is attributed to the passage of the cooling frequency, for example GRB 990510 (Kumar and Panaitescu, 2000), GRB 030329 (Sato et al., 2004; Uemura et al., 2003), GRB 040924 (Huang et al., 2005), GRB 041218 (Torii et al., 2005), GRB 050408 (Kann et al., 2010), GRB 050502A (Yost et al., 2006), GRB 060729 (Grupe et al., 2010), etc. In some cases, this claim is supported by measured spectral evolution. Lipkin et al. (2004) measured the $B - R$ color change in the afterglow of GRB 030329, supporting the theory of the cooling break passage derived from the light-curve steepening. Only very few GRBs had coverage in several bands good enough to model the evolution of the afterglow spectrum. In one such rare case, de Ugarte Postigo et al. (2005) modelled the broad-band SED of the afterglow of GRB 021004 at three distinct epochs, though only the low frequency part of the spectrum shows any evolution. In order to study such spectral evolutions in detail, continuous coverage with high signal-to-noise ratio in several bands simultaneously is required.

The *Swift* satellite (Gehrels et al., 2004) makes it possible to study the afterglow emission starting at very early times thanks to its rapid slewing capability, a precise localization of GRBs with its Burst Alert Telescope (BAT, Barthelmy et al., 2005), and early follow-up with onboard telescopes sensitive at X-ray (XRT, Burrows et al., 2005b) and ultraviolet/optical (UVOT, Roming et al., 2005) wavelengths. Since its launch in 2004, *Swift* has provided many early and well-sampled afterglow light curves and X-ray spectra. Blustin et al. (2006) for example fitted broad-band SEDs of the afterglow of GRB 050525A with a cooling break between early optical and X-ray data and with a simple power-law through later epochs, suggesting a spectral evolution. However, such sudden spectral change can sometimes be also attributed to another component with a

different electron distribution present in the emission at later times (Chapter 3).

The most convincing measurement of the cooling break movement to this date is the case of the naked-eye burst GRB 080319B (supplementary information in Racusin et al. (2008); Schady et al. in prep.). Due to the enormous brightness of this event, these authors were able to fit broad-band SEDs at several epochs using *Swift* UVOT and XRT data, as well as a multitude of optical and NIR ground-based data, showing a clear temporal evolution of a break that may be attributed to the cooling break. The previously mentioned examples show that in case of regularly bright GRB afterglows small telescopes cannot provide the accuracy needed for such detailed study.

The Gamma-Ray burst Optical Near-infrared Detector (GROND, Greiner et al., 2008, 2007) at the 2.2 m MPI/ESO telescope at La Silla observatory is capable of providing high-quality, very well-sampled data in seven bands simultaneously and therefore opening a new region with respect to data quality and quantity. Such high-precision data allow not only for a detailed study of afterglow light curves (Greiner et al., 2009b; Nardini et al., 2011) but also jets of GRBs (Krühler et al., 2009), the dust in their host galaxies (Krühler et al., 2008; Küpcü Yoldaş et al., 2010; Greiner et al., 2011; Krühler et al., 2011a), their redshifts (Greiner et al., 2009a; Krühler et al., 2011b) and much more.

Here we provide details of the *Swift* and GROND observations of the afterglow of GRB 091127 and discuss the light curves and SEDs in the context of the fireball model thanks to very good energy coverage and sampling of our high-quality data. Throughout the paper, we adopt the convention that the flux density of the GRB afterglow can be described as $F_\nu(t) \propto t^{-\alpha}\nu^{-\beta}$, where α is the temporal and β the spectral index. Unless stated otherwise in the text, all reported errors are at 1σ confidence level.

4.2 Observations

4.2.1 Prompt emission

At $T_0 = 23:25:45$ UT, the *Swift*/BAT was triggered by the long GRB 091127 (Troja et al., 2009a). Due to an Earth-limb observing constraint, *Swift* could not slew to the target until 53 min after the trigger (Immler and Troja, 2009). The mask-weighted light curve shows three main peaks from $T_0 - 0.3$ to $T_0 + 10$ s, peaking at $\sim T_0$, $T_0 + 1.1$ s and at $T_0 + 7$ s. The measured T_{90} (15-350 keV) is 7.1 ± 0.2 s (Stamatikos et al., 2009). The BAT prompt emission spectrum from $T_0 - 0.4$ to $T_0 + 7.5$ s is best fitted using a simple power-law model with photon index 2.05 ± 0.07 and the total fluence in the 15-150 keV energy range is $(9.0 \pm 0.3) \times 10^{-6}$ erg/cm^2 (Stamatikos et al., 2009). We can get a better picture of the prompt emission from the instruments with larger energy coverage. Konus-Wind observed the burst in the 20 keV - 2 MeV energy range and measured a fluence of $(1.22 \pm 0.06) \times 10^{-5}$ erg/cm^2. The time-integrated spectrum of the burst (from T_0 to $T_0+8.4$ s) is well fitted by a power-law with exponential cutoff model with $\alpha = -1.95 \pm 0.10$, and $E_{\text{peak}} = 21.3^{+4}_{-3}$ keV (Golenetskii et al., 2009). Using a standard concordance cosmology ($H_0 = 71.0$ km/s/Mpc, $\Omega_M = 0.27$, $\Omega_\Lambda = 0.73$,

Komatsu et al. (2009)), and a redshift of $z = 0.49$ (Cucchiara et al., 2009; Thoene et al., 2009), we calculate the bolometric (1 keV - 10 MeV) energy release of GRB 091127 to be $E_{\rm iso} = 1.4 \times 10^{52}$ erg. Fermi GBM provides even better energy coverage and the obtained time-averaged spectrum from $T_0 + 0.002$ s to $T_0 + 9.984$ s is adequately fit by a Band function (Band et al., 1993) with $E_{\rm peak} = 35.5 \pm 1.5$ keV, $\alpha_{\rm prompt} = -1.26 \pm 0.07$, and $\beta_{\rm prompt} = -2.22 \pm 0.02$. The event fluence in the 8 - 1000 keV energy range in this time interval is $(1.92 \pm 0.02) \times 10^{-5}$ erg/cm^2 (Goldstein et al., in prep.). This results in the bolometric energy release of $E_{\rm iso} = 1.6 \times 10^{52}$ erg, making GRB 091127 consistent within 2σ with the most updated Amati $E_{\rm peak}$ - $E_{\rm iso}$ relation (Amati et al., 2002).

4.2.2 Swift XRT

The *Swift*/XRT started observations of the field of GRB 091127 53 min after the trigger (Evans et al., 2009b). The XRT light curve and spectra were obtained from the XRT repository (Evans et al., 2007, 2009a). Spectra were grouped using the grppha task and fitted with the GROND data in XSPEC v12 using χ^2 statistics. The combined optical/X-ray spectral energy distributions were fitted with power-law and broken power-law models and two absorbing columns: one Galactic foreground with a hydrogen column density of $N_H = 2.8 \times 10^{20}$ cm^{-2} (Kalberla et al., 2005) and another one that is local to the GRB host galaxy at $z = 0.49$ (Cucchiara et al., 2009; Thoene et al., 2009). Only the latter was allowed to vary in the fits. To investigate the dust reddening in the GRB environment, the zdust model was used, which contains Large and Small Magellanic Clouds (LMC, SMC) and Milky Way (MW) extinction laws from Pei (1992). The errors of the broad-band SED fits on any single parameter were obtained using the *uncert* command in XSPEC. This calculates the error on the parameter in question while allowing all the other non-frozen parameters in the model to vary.

4.2.3 GROND

GROND responded to the *Swift* GRB alert and initiated automated observations at 00:24 UT, 58 m after the trigger (Updike et al., 2009). GROND imaging of the field of GRB 091127 continued for ten further epochs, the last being acquired on October 31st, 2010. Due to the broken chip of the NIR K-band detector, there are no data available for this filter. A variable point source was detected in all other bands by the automated GROND pipeline (Yoldaş et al., 2008). The position of the transient was calculated to be R.A. (J2000) = 02:26:19.87 and Dec. (J2000) = -18:57:08.6 compared to USNO-B reference field stars (Monet et al., 2003) with an astrometric uncertainty of $0.''3$.

The optical and NIR image reduction and photometry were performed using standard IRAF tasks (Tody, 1993) similar to the procedure described in detail in Krühler et al. (2008). A general model for the point-spread function (PSF) of each image was constructed using bright field stars and fitted to the afterglow. In addition, aperture photometry was carried out, and the results were consistent with the reported PSF photometry. All data were corrected for a Galactic foreground reddening of $E_{\rm B-V} = 0.04$
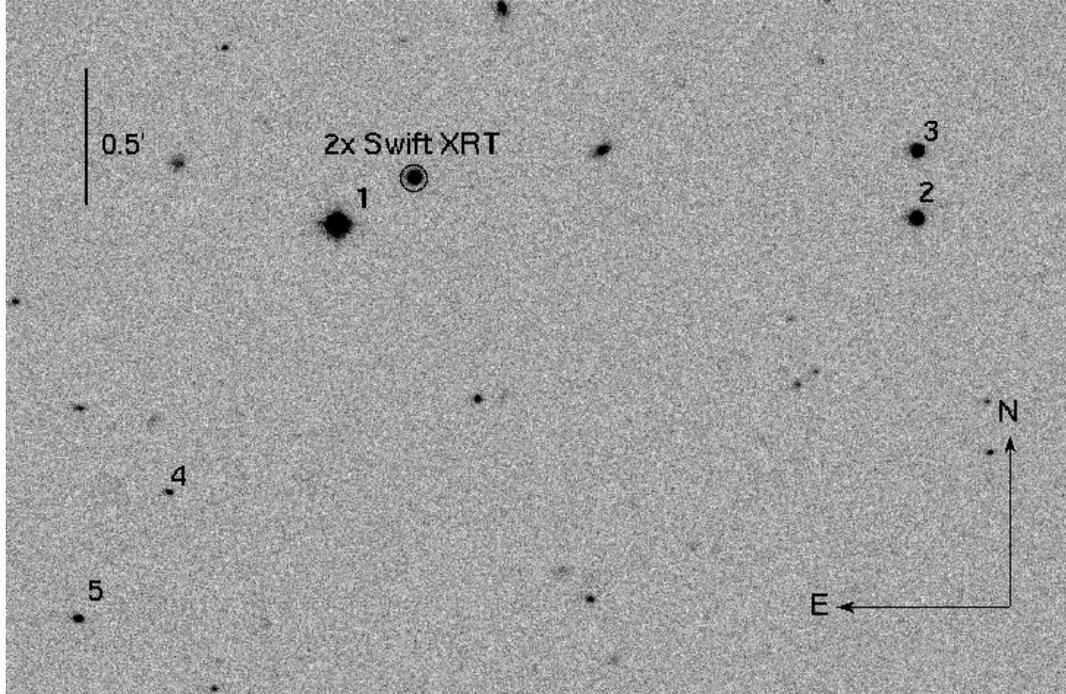
Figure 4.1 GROND r' band image of the field of GRB 091127 obtained 4.3 ks after T_0. The optical afterglow is visible inside the *Swift* XRT error circle with double diameter for better clarity. The secondary standard stars are numbered from 1 to 5 and their magnitudes reported in Table 4.1.

mag in the direction of the burst (Schlegel et al., 1998), corresponding to an extinction of $A_V = 0.12$ using $R_V = 3.1$, and in the case of JH data, transformed to AB magnitudes.

Optical photometric calibration was performed relative to the magnitudes of five secondary standards in the GRB field, shown in Fig. 4.1 and Table 4.1. During photometric conditions, a spectrophotometric standard star SA94-242, a primary SDSS standard (Smith et al., 2002), was observed within a few minutes of observations of the GRB field. The obtained zeropoints were corrected for atmospheric extinction and used to calibrate stars in the GRB field. The apparent magnitudes of the afterglow were measured with respect to the secondary standards reported in Table 4.1. The absolute calibration of JH bands was obtained with respect to magnitudes of the Two Micron All Sky Survey (2MASS) stars within the GRB field obtained from the 2MASS catalog (Skrutskie et al., 2006). All data are listed in Tables 6.3 and 6.4.

Table 4.1 Secondary standards in the GRB field in the GROND filter bands used for the calibration

Star number	R.A., Dec [J2000]	g' (mag$_{AB}$)	r' (mag$_{AB}$)	i' (mag$_{AB}$)
1	02:26:21.05, −18:57:19.1	15.18 ± 0.03	14.49 ± 0.03	14.22 ± 0.03
2	02:26:12.17, −18:57:17.6	17.48 ± 0.03	16.64 ± 0.03	16.26 ± 0.03
3	02:26:12.14, −18:57:02.9	17.74 ± 0.03	16.96 ± 0.03	16.80 ± 0.03
4	02:26:23.64, −18:58:17.8	22.17 ± 0.03	20.43 ± 0.03	19.34 ± 0.03
5	02:26:25.03, −18:58:45.5	20.59 ± 0.03	19.05 ± 0.03	18.16 ± 0.03

Star number	R.A., Dec [J2000]	z' (mag$_{AB}$)	J (mag$_{Vega}$)	H (mag$_{Vega}$)
1	02:26:21.05, −18:57:19.1	14.07 ± 0.03	13.03 ± 0.05	12.57 ± 0.05
2	02:26:12.17, −18:57:17.6	16.06 ± 0.03	14.47 ± 0.05	14.38 ± 0.05
3	02:26:12.14, −18:57:02.9	16.71 ± 0.03	14.93 ± 0.05	15.35 ± 0.05
4	02:26:23.64, −18:58:17.8	18.80 ± 0.03	-	-
5	02:26:25.03, −18:58:45.5	17.71 ± 0.03	-	-

4.3 Results

4.3.1 Afterglow Light Curve

The X-ray light curve (Fig. 4.2) of the afterglow of GRB 091127 is best fitted with a smoothly broken power-law model (Beuermann et al., 1999) with an initial decay slope $\alpha_X = 1.02 \pm 0.04$, a time of the break at around 33 ks and a post-break temporal slope of 1.61 ± 0.04 (Fig 4.3, red. $\chi^2 = 1.03$, straight power-law has red. $\chi^2 = 1.80$, sharply broken power-law has red. $\chi^2 = 1.04$). The optical/NIR light curve follows the same model but with a much flatter initial temporal slope, which further flattens with increasing wavelength of GROND filters. Table 4.2 shows results of the fitting of a smoothly broken power-law model to each band separately. The sharply broken power-law model provides a much worse fit with red. $\chi^2 > 10$ in the optical bands. This initial temporal slope is however difficult to measure because the pre-break optical/NIR data show a smooth curvature without a straight power-law segment. The reported temporal slope parameters fitted to these data should therefore be considered as estimates of power-law slopes of the earliest optical/NIR data.

The difference in the early decay between X-ray and optical/NIR wavelengths and among optical/NIR bands themselves suggest a strong color evolution, which we discuss in detail in the next section. The time of the X-ray break and the later decay index of the X-ray fit is within 1σ errors of the fit to the optical bands and within 3σ errors of the fit to the NIR bands. The optical/NIR data after 500 ks are not fitted as they show contribution from the SN 2009nz bump described by Cobb et al. (2010), Berger et al. (2011) and Vergani et al. (2011). We did not subtract the SN magnitudes from the afterglow because this work is based mostly on the early data where the afterglow is dominant. Moreover, at even later times, the GROND decay after the break is consistent with the X-ray temporal slope, and the GROND SEDs are well-fitted with a straight
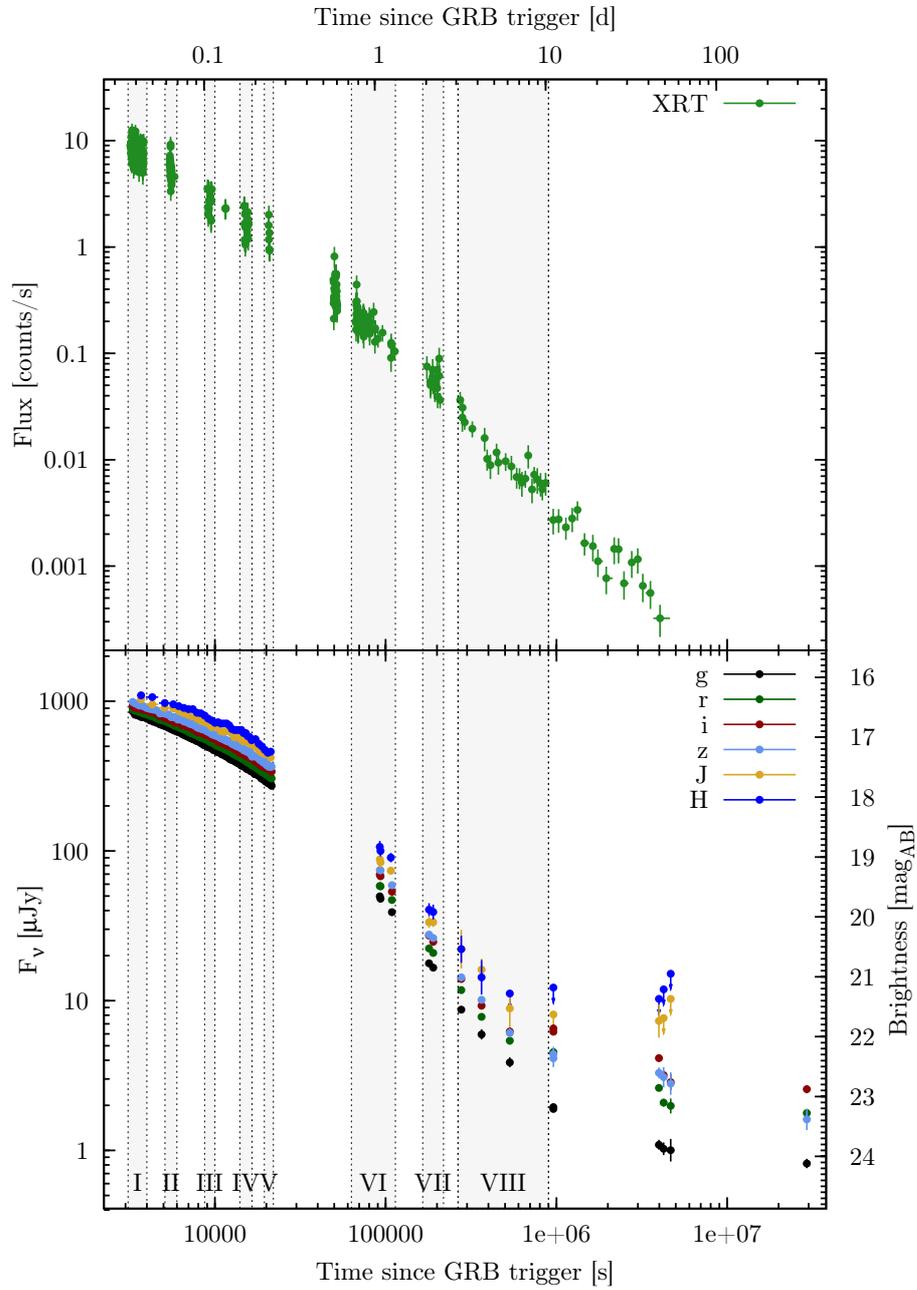
Figure 4.2 Light curve of the X-ray (top panel) and GROND optical/NIR (bottom panel) afterglow of GRB 091127. Shown data are corrected for Galactic foreground extinction and are in AB magnitudes. Gray regions show the time intervals where broad-band SEDs were created (Figs. 4.5 and 4.6).
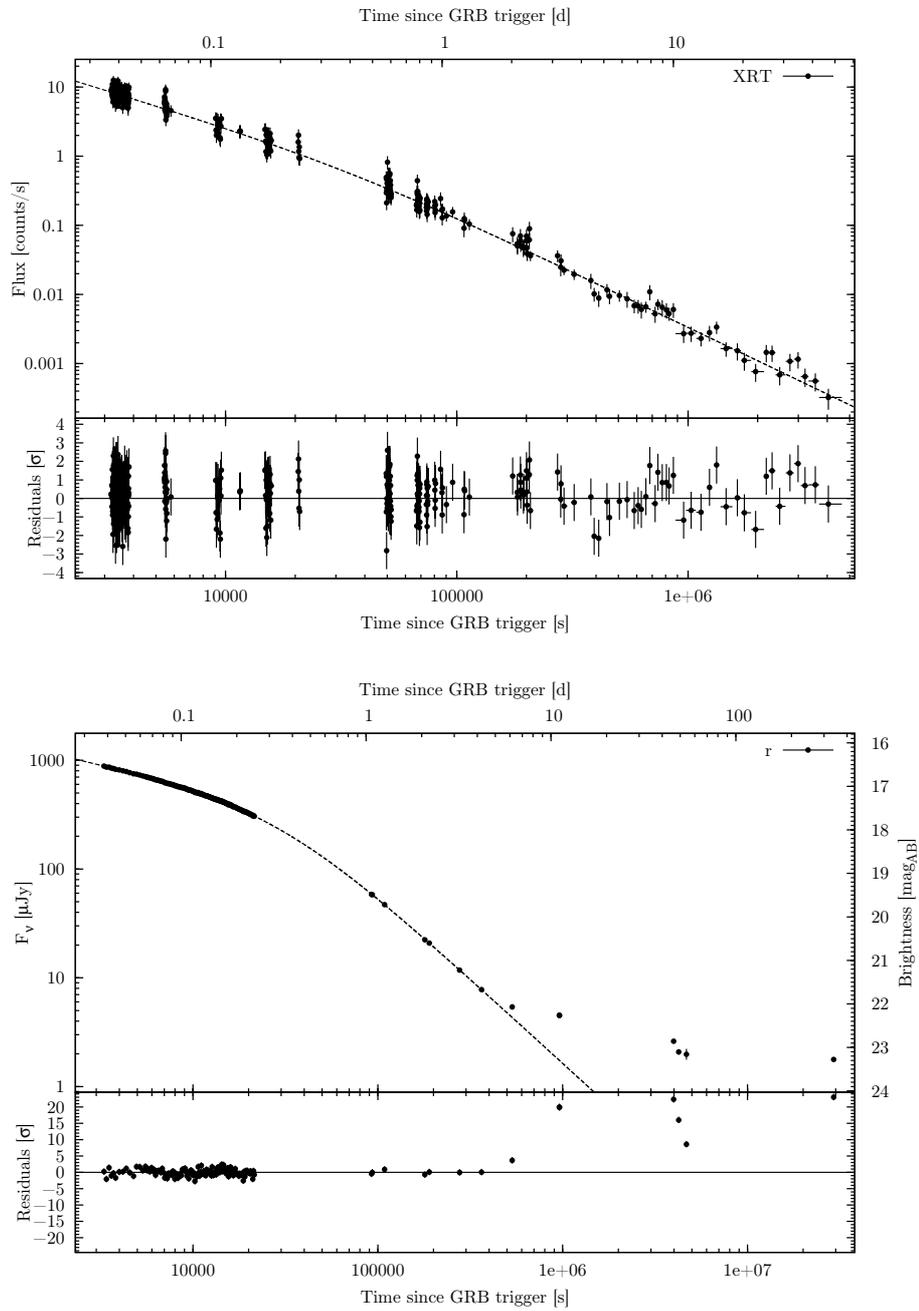
Figure 4.3 The smoothly broken power-law fit to the X-ray light curve (top) and the GROND r' band data (bottom), the parameters of the fit are listed in Table 4.2. Residuals from the best-fit to the r' band data show the SN bump.

power-law. We therefore argue that the influence of the emission not coming from the GRB itself is negligible throughout the time interval used for this study.

Table 4.2 Light curve fit parameters for the afterglow of GRB 091127. The temporal slopes have inaccuracies caused by a very smooth break, which reduces the number of datapoints used in the power-law slopes fitting. The fitting of the NIR bands is affected by the somewhat lower signal-to-noise ratio of the NIR data as compared to the optical bands.

Band	α_1	$t_{\mathrm{break}}[s]$	s	α_2	χ^2/d.o.f.
XRT	1.019 ± 0.039	33472 ± 3349	2.367 ± 0.986	1.605 ± 0.038	373 / 363
g'	0.427 ± 0.011	33917 ± 2047	1.210 ± 0.125	1.687 ± 0.050	125 / 144
r'	0.376 ± 0.009	29287 ± 1195	1.274 ± 0.100	1.557 ± 0.033	143 / 144
i'	0.359 ± 0.014	30288 ± 1671	1.293 ± 0.141	1.532 ± 0.042	133 / 144
z'	0.321 ± 0.016	32368 ± 2295	1.054 ± 0.124	1.609 ± 0.056	131 / 144
J	0.300 ± 0.077	24462 ± 4453	1.483 ± 0.728	1.396 ± 0.147	26 / 37
H	0.164 ± 0.057	21677 ± 4310	1.005 ± 0.106	1.417 ± 0.068	34 / 37

4.3.2 Afterglow SEDs

As already evident from the afterglow light curves, there is a strong spectral evolution in the optical/NIR wavelengths before the break. Thanks to the simultaneous multi-band observing capabilities of GROND, it is possible to measure the optical/NIR spectral slope as a function of time with high accuracy. Fig. 4.4 shows that the optical/NIR spectral index rises from 0.23 ± 0.04 to 0.80 ± 0.08 between 3 and 300 ks. In addition, broad-band optical/NIR to X-ray SEDs were constructed at eight different time intervals within this period, which are indicated in the light curve (Fig. 4.2). Fits of optical/NIR data alone as well as the broad-band fits resulted in a host dust extinction that was consistent with zero, therefore in all the models we assumed no host dust extinction for simplicity.

Fitting the XRT-only spectrum using the full dataset we obtain the host absorbing column density $N_H = (1.3 \pm 0.5) \times 10^{21}$ cm^{-2}. Because the broad-band SEDs proved to be inconsistent with a simple power-law model, we used models that include a break between the X-ray and optical/NIR data. We initially fitted all eight epochs of broad-band SEDs simultaneously with a sharp broken power-law model, where the host-intrinsic absorbing column density and the X-ray spectral index are tied between each SED but left free to vary. The low energy spectral indices and energy of the break were left untied between SEDs and free to vary. The best fit (red. $\chi^2 = 1.11$) gives values of the host-equivalent neutral hydrogen density $N_H = (3.2 \pm 0.6) \times 10^{20}$ cm^{-2} and the high-energy spectral index $\beta_X = 0.748 \pm 0.004$. The value of N_H is smaller than what we get using just the XRT data alone but is consistent within 2σ with the one resulting from the XRT-only spectral fitting.

The best-fit optical parameters are listed in Table 4.3. This fit shows that the break evolves to larger wavelengths in time, through and beyond the optical/NIR bands (Fig. 4.5). The last two SEDs are consistent with a simple power-law continuum without
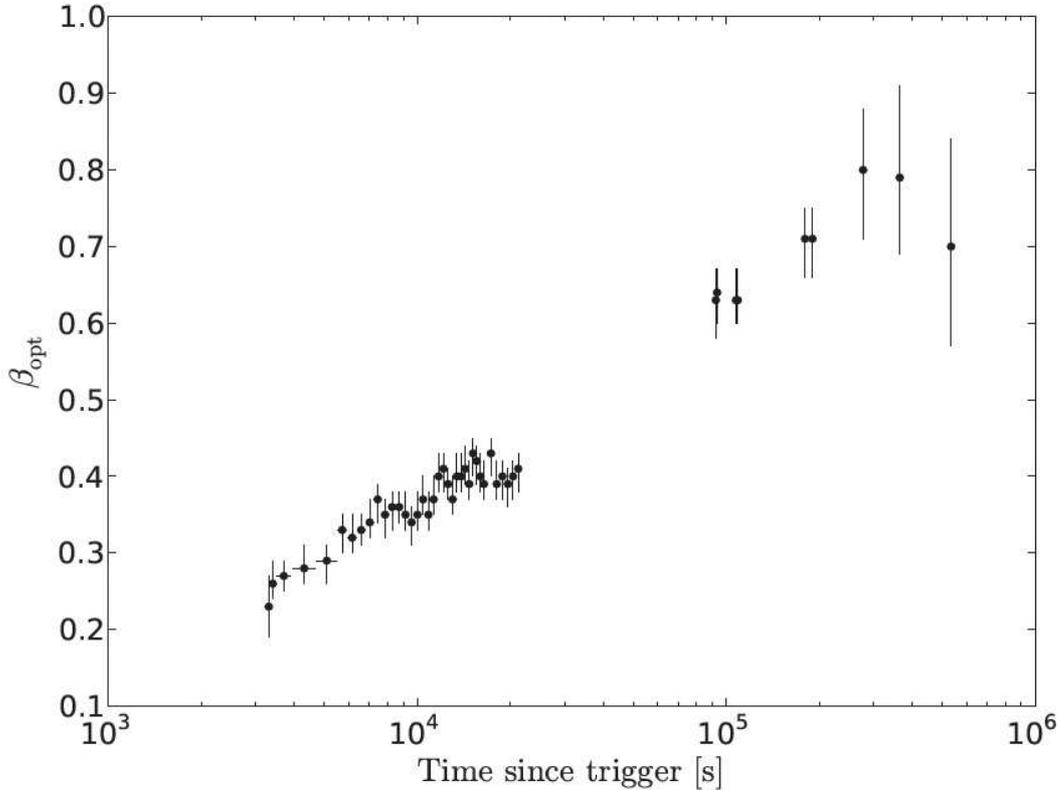
Figure 4.4 The optical/NIR spectral slope as a function of time.

any break. This is in agreement with the X-ray spectral index being within 1σ errors consistent with optical/NIR-only spectral indices 0.71 ± 0.04 (at time of SED VII) and 0.80 ± 0.08 (at time of SED VIII). The temporal evolution of the break was fitted with a power-law $\nu_c \propto t^x$ and the best-fit index was $x = -0.69 \pm 0.10$ (Fig. 4.5).

Because the fit using the sharp break requires the low-energy spectral index β_{opt} to be time-dependent, we needed a model that would be consistent with constant spectral indices that the theory expects. We therefore also fitted all eight broad-band SEDs simultaneously with two power-laws connected by a smooth break with flux density following

$$F_\nu \propto \left[(\nu/\nu_{\mathrm{break}})^{-s\beta_1} + (\nu/\nu_{\mathrm{break}})^{-s\beta_2} \right]^{-1/s}, \tag{4.1}$$

where s is a parameter that describes the sharpness of the break. Given that the break is far from the X-ray bands, we do not expect the change in the model from a sharp to a smooth break to change the best-fit values of the host absorbing column density N_H nor the high-energy spectral index β_X. We therefore froze N_H and β_X to the best-fit value from the sharp broken power-law fit in order to reduce the number of free parameters in this more complicated model. We fixed the difference in values between low and high energy spectral indices to 0.5 (as predicted for the cooling break by the standard
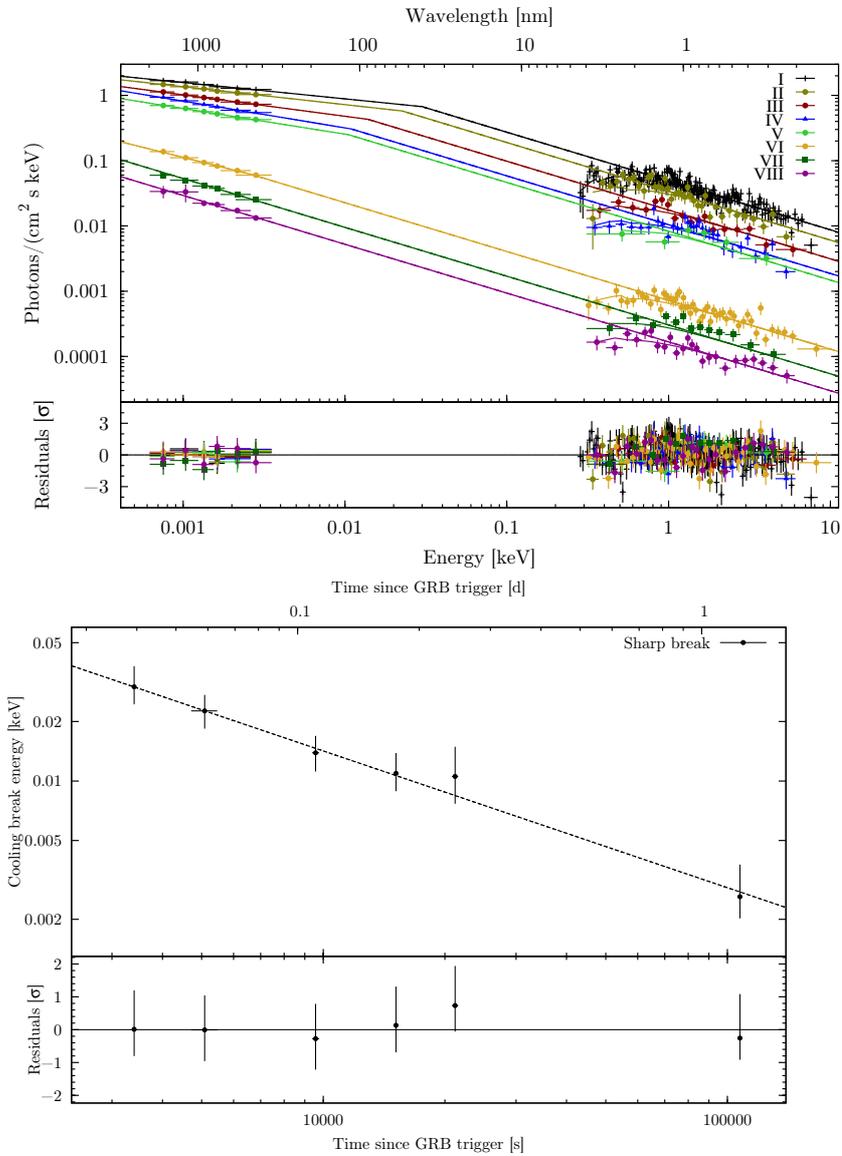
Figure 4.5 Broad-band optical/NIR to X-ray SEDs fitted with a broken power-law with the sharp break (top). Best-fit power-law fit to the temporal evolution of the cooling-break energy (bottom).

fireball model; Sari et al. (1998)). The smoothness of the break was tied between each SED but left free to vary and the break energy was left free to vary completely. The fit (Fig. 4.6) again shows the break moving towards the lower energies but in this case the movement is faster than with the sharp break and the fit of the energy over time gives a power-law slope of -1.23 ± 0.06.
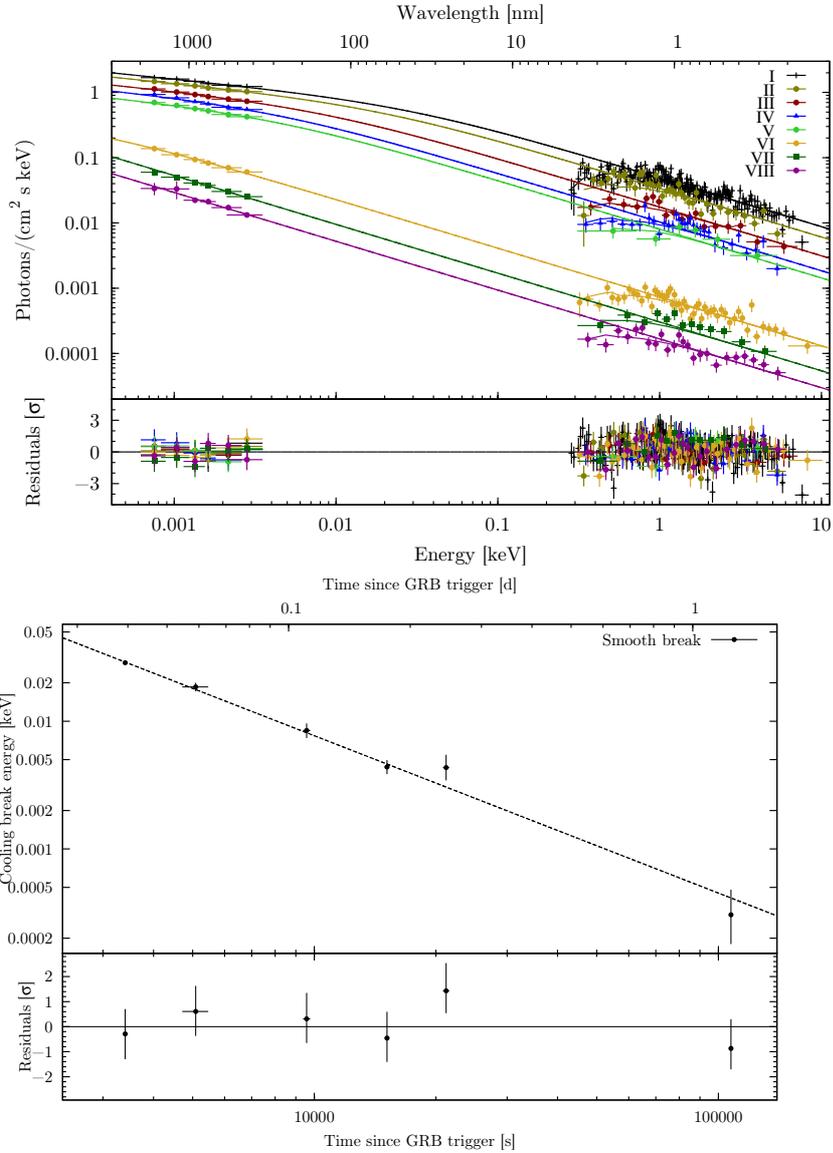
Figure 4.6 Broad-band optical/NIR to X-ray SEDs fitted with a broken power-law with the smooth break (top). Best-fit power-law fit to the temporal evolution of the cooling-break energy (bottom).

4.3.3   Closure relations

Using the X-ray light-curve fit and the results from the broad-band SEDs, we can test the closure relations (Granot and Sari, 2002; Dai and Cheng, 2001; Zhang and Mészáros, 2004; Racusin et al., 2009) between temporal and spectral indices. The fit-derived X-ray spectral index $\beta_X = 0.75$ results in a fairly hard power-law index of the

electron energy distribution $p = 1.50 \pm 0.01$. In the X-rays, the equation (Racusin et al., 2009) for $1 < p < 2$ and a constant decay in the $\nu_X > \nu_c$ regime, where the jet is interacting with a homogeneous interstellar medium (ISM) and is in the slow cooling phase, gives value of $\alpha_X = 0.91$ for the spectral index $\beta_X = 0.75$ derived from the fits. This value is within 3σ of the X-ray light curve pre-break decay slope of 1.02 ± 0.04. However, the fast cooling phase in the $\nu_X > \nu_m$ regime gives the same value, therefore we cannot distinguish between fast and slow cooling.

The light curve break at X-rays around 33 ks must obviously be due to a different phenomenon than the cooling break, as the latter started already below the X-ray band at ~ 3 ks, and then moved to longer wavelengths. The post-break evolution of the X-ray light curve is best fitted with the equation describing a non-spreading uniform jet in the ISM, which gives $\alpha_X = 1.66$, a value consistent within 2σ of the fit-derived 1.61 ± 0.04. This suggests that, despite the X-ray decay slopes being shallower than the canonical values (Zhang et al., 2006; Nousek et al., 2006), the break in the light curve at around 33 ks represents a jet break (Sari et al., 1999). Such shallow (< 2 with high confidence) post-break decay slopes have been seen in multiple well-sampled optical light curves (Zeh et al., 2006). From the time of the break we can estimate the opening angle of the jet to be $\theta \sim 4°$ (Burrows and Racusin, 2006), substituting the measured quantities and normalizing to the typical values $n = 1$ cm^{-3} and $\eta = 0.2$. These values lead to the beaming factor and the true gamma-ray energy release (Frail et al., 2001; Bloom et al., 2003) of $f_b = (1 - \cos\theta_{jet}) = 2.4 \times 10^{-3}$ and $E_\gamma = 3.9 \times 10^{49}$ erg. For a value of $n = 3$ cm^{-3}, which is the standard value used for the Ghirlanda relation (Ghirlanda et al., 2007), we get a jet opening angle $\theta \sim 4.9°$ and $E_\gamma = 5.9 \times 10^{49}$ erg. With these values, GRB 091127 lies within the 1σ scatter of the Ghirlanda relation.

Table 4.3 Best-fit parameters resulting from the sharp and smooth broken power-law fits to the broad-band SEDs. The smoothness of the break in the fit using the smooth break between the low- and high-energy spectral index is 2.2 ± 0.2.

SED number	Midtime [s] of SED	Low energy spectral index using sharp break	Cooling break [eV] using sharp break	Cooling break [eV] using smooth break
I	3404	$0.25^{+0.02}_{-0.04}$	$29.9^{+8.1}_{-5.5}$	$28.7^{+1.1}_{-1.1}$
II	5088	0.28 ± 0.04	$22.6^{+4.6}_{-4.2}$	$18.5^{+1.5}_{-1.4}$
III	9576	$0.33^{+0.03}_{-0.04}$	$13.9^{+3.0}_{-2.7}$	$8.5^{+1.2}_{-1.1}$
IV	15135	$0.41^{+0.03}_{-0.03}$	$10.9^{+2.9}_{-2.0}$	$4.4^{+0.6}_{-0.5}$
V	21193	$0.39^{+0.04}_{-0.03}$	$10.5^{+4.4}_{-2.9}$	$4.3^{+1.1}_{-0.9}$
VI	107401	$0.62^{+0.04}_{-0.05}$	$2.6^{+1.2}_{-0.6}$	$0.3^{+0.2}_{-0.1}$
VII	189939	-	< 0.7	< 0.7
VIII	277071	-	< 0.7	< 0.7

4.4 Discussion

The high quality of the data allows us to discuss whether any characteristic synchrotron spectral break could be responsible for the break in the afterglow SED of GRB 091127, and to constrain the sharpness of the break.

4.4.1 Injection break

The shape of our broad-band SEDs suggests that the only plausible scenario for the break to be ν_m is the fast-cooling case (Sari et al., 1998). According to the equations in Dai and Cheng (2001), in the case of an ISM medium and for $p = 1.5$, the characteristic synchrotron frequency ν_m moves towards lower frequencies as $t^{-2.6}$. That is too fast to be consistent with our measurements of the break evolution both for the sharp and the smooth break. The predicted light curve slope of $\alpha = 0.25$ before the passage of the injection break is slightly flatter than our early optical slope. But as previously stated, this slope determination is difficult due to the smooth curvature of the early optical/NIR light curve.

However, it is the low-energy spectral slope that is least consistent with the injection break scenario. The SED below ν_m is expected to be a power-law with index 0.5, completely independent of the electron energy distribution p. This is not consistent with either the sharp break, where the initial slope is a factor 2 flatter and moreover evolving in time, or the smooth break, where the low-energy slope is 0.25 throughout the observation. While this value was fixed in the smooth-break fit, any steeper low-energy slope makes the fit considerably worse and the initial flat optical/NIR only SEDs impossible to explain. Therefore we argue that the moving break in the afterglow of GRB 091127 cannot be interpreted as the characteristic synchrotron frequency ν_m.

4.4.2 Cooling break

Theoretical expectations

According to theory (Sari et al., 1998; Dai and Cheng, 2001), in case of an ISM circum-burst environment, the cooling break moves towards lower frequencies with time as a power-law with index -0.5. This is within 2σ of the sharp break fits (Fig. 4.5), where the break moves with index -0.69 ± 0.10. However, the sharp-break fit requires temporal change of the low-energy spectral index. This is inconsistent with the fireball model, where the difference between low- and high-energy spectral indices below and above the cooling frequency is constant and $\Delta\beta = 0.5$.

To satisfy the condition of a constant $\Delta\beta$, we fitted the SEDs with a smooth break, that can gradually change the spectral index of the data, which occupies a sufficiently narrow portion of the spectra (in this case optical/NIR wavelengths) to not show evidence for inherent curvature. The smooth-break fit therefore allows both low- and high-energy indices to remain constant, while changing the spectral index fit to GROND data with time, as the break crosses the optical bands (Fig. 4.4). Before any further

discussion, we need to address the question of the physical plausibility of the smooth break.

When we examined the SEDs from studies of large GRB samples (Greiner et al., 2011; Schady et al., 2007; Nardini et al., 2006; Schady et al., 2010; Starling et al., 2007), we see that they are well fitted with a sharp cooling break (where the break is plausible). This simplistic choice works well for sample studies where it is difficult to distinguish between a sharp and a smooth shape of the break either because the break is far enough from the measured data or because the data lack sufficient quality to constrain the smoothness parameter, but can fail in cases like GRB 091127, where extremely large multi-color data sets are available. Although previous studies did not require more complex models, Granot and Sari (2002) calculated that the power-laws in the afterglow spectra are indeed connected by smooth breaks. The theoretical smoothness of the cooling break is $1.15 - 0.06p = 1.06$ for $p = 2 \times \beta_X = 1.5$. This is roughly a factor of 2 less (i.e., smoother) than our fit-derived smoothness of 2.2 ± 0.2.

The significant inconsistency, however, is related to the speed of the cooling break, which in the smooth fit moves with an index -1.23 ± 0.06, a value much higher than the expected -0.5. Similar to the value of -1.00 ± 0.14 derived for the cooling break movement reported by Racusin et al. (2009), it would require that we abandon some simplifications often assumed in the simplest formulations of the fireball model. The flux evolution for adiabatic slow cooling in this synchrotron emission theory is described by Eq. (8) in Sari et al. (1998) and for convenience we report it here as

$$
F_\nu = \begin{cases} (\nu/\nu_m)^{-(p-1)/2} F_{\nu,\max}, & \nu_c > \nu > \nu_m, \\ (\nu_c/\nu_m)^{-(p-1)/2}(\nu/\nu_c)^{-p/2} F_{\nu,\max}, & \nu > \nu_c, \end{cases} \tag{4.2}
$$

where the break frequencies for the case of $p < 2$ can be calculated from Dai and Cheng (2001) and Chevalier and Li (2000) to be

$$
\begin{aligned}
\nu_c &\propto \epsilon_B^{-3/2} E_{\mathrm{iso}}^{-1/2} t^{-1/2}, \\
\nu_m &\propto \epsilon_B^{1/2(p-1)} \epsilon_e^{2/(p-1)} E_{\mathrm{iso}}^{p+2/8(p-1)} t^{-3(p+2)/8(p-1)}, \\
F_{\nu,\max} &\propto \epsilon_B^{1/2} E_{\mathrm{iso}},
\end{aligned} \tag{4.3}
$$

where t is the time since the GRB trigger, E_{iso} is the isotropic energy of the GRB, ϵ_B is the fraction of the energy carried by the magnetic field and ϵ_e the fraction of the energy in electrons. In the standard fireball model, all parameters are constant in time and the density in the ISM is homogeneous. For the cooling break speed to be consistent with our measurements, one of the parameters ϵ_B and E_{iso} (or a combination of them) must evolve with time. Using Eq. 4.2 and 4.3, we can easily examine cases where each of these parameters evolves separately and model the impact of such an evolution on the resulting afterglow flux.

Theoretical implications

To obtain the measured cooling break speed of $t^{-1.23\pm0.06}$ we need one of the parameters (we treat them separately for simplicity) to add $t^{-0.73\pm0.06}$ to the theoretical speed of $t^{-0.5}$. As we can see from the Eq. 4.2, the change of the flux evolution before and after the cooling break passage is proportional to the cooling break frequency evolution as $\nu_c^{0.5}$. This means that the cooling break that is faster by a factor of $t^{-0.73\pm0.06}$ would add $\Delta\alpha = 0.37\pm0.03$ to the standard change of the temporal index of $\Delta\alpha = 0.25$ (Sari et al., 1998) caused by the cooling brake passage.

As we already stated, the early optical/NIR slope is difficult to obtain. However, we can estimate it by calculating the weighted mean of the values of the optical/NIR parameter α_1 in Table 4.2. This results in a decay index of $\alpha = 0.38$ before the jet break at around 33 ks. If we assume this to be the decay index before the cooling break passage, and we take the X-ray pre-jet-break temporal slope of $\alpha = 1.02\pm0.04$ to be the one after the cooling break passage, we get a very good (within 1σ) consistency with our calculated $\Delta\alpha = 0.62\pm0.03$. While the amount by which the light-curve steepens is only dependent on the speed of the cooling break and not on which parameter causes it, the flux evolution and therefore the decay index itself before and after the cooling break passage depends strongly on which parameter we let evolve in time. Using Eq. 4.2 and 4.3, we can calculate how the time evolution of the flux density depends on these parameters for $p < 2$ (for $p > 2$ see Eq. B7 and B8 in Panaitescu and Kumar (2000)). We calculate

$$
F_\nu \propto \begin{cases} E^{(p+18)/16}\epsilon_B^{3/4}t^{-3(p+2)/16}, & \nu_c > \nu > \nu_m, \\[2mm] E^{(p+14)/16}t^{-(3p+10)/16}, & \nu > \nu_c. \end{cases} \tag{4.4}
$$

Letting the isotropic energy vary in time results in $F_\nu \propto E^{(p+18)/16}$ for $\nu < \nu_c$ and $F_\nu \propto E^{(p+14)/16}$ for $\nu > \nu_c$. In this case the increased speed of the cooling break is the result of the isotropic energy which increases in time as $t^{1.46}$. This dependence using the fit-derived $p = 1.5$ decreases the temporal index before and after the cooling break passage by 1.78 and 1.41 respectively. Such extreme flattening of the light curve would mean that without the energy injection the decay slope before the jet break would be $\alpha_1 = 1.02 + 1.41 = 2.4$ and the late temporal slope after the jet break $\alpha_2 = 1.61 + 1.41 = 3.0$, values which are unusually steep for a GRB afterglow (Racusin et al., 2009). The energy E_{iso} is directly dependent on the energy injection and indirectly on the density profile around the burst and we can examine the influence of the time evolution of these parameters on the energy using equations from Sari and Mészáros (2000).

The density profile of the medium can be calculated from the cooling-break temporal exponent using equations in Table 1 of Sari and Mészáros (2000). There $\nu_c \propto t^{(3g-4)/2(4-g)}$, where g is the power-law index of the external density profile $n \propto r^{-g}$. The same approach was used by Racusin et al. (2009) for GRB 080319B where the cooling break speed of t^{-1} results in the steep density profile $n \propto r^4$, which requires

the existence of a complex medium with a density enhancement. However, our cooling break speed of $t^{-1.23}$ implies an implausibly steep density profile of $n \propto r^{11}$, which would be very difficult to defend physically and support observationally.

Using Eq. 11 in Sari et al. (1998) for the cooling break frequency and assuming typical values of $n_1 = 1$ and $\epsilon_B = 0.01$, we can calculate the isotropic energy of the burst at times corresponding to the first (SED I) and the last (SED VI) point where we measure the position of the cooling break using the smooth break fit. The best-fit parameters in Table 4.3 give $E_{52} \sim 3.8$ at $t = 3.4$ ks and $E_{52} \sim 1080$ at $t = 107.4$ ks. The increasing energy of GRBs can possibly be explained by refreshed shocks, where the central engine ejects shells with a range of Lorentz factors. When the slower material catches up with the decelerating ejecta, it re-energizes it (Sari and Mészáros, 2000). However, assuming a constant density profile, this scenario requires extreme energy injection, leading to an injection parameter $s = 8.6$ (see Table 1 in Sari and Mészáros (2000)). Such a scenario is very unlikely, as it would require the initial low-energy ejecta to be re-energized by a very large amount of energy stored in slowly moving material. It would also require a gradual and continuous energy injection over the time of our light curve coverage, i.e. $\sim 10^6$ sec, a scenario which so far has never been advocated. We therefore also consider a change of energy input an unlikely explanation for the temporal behavior of GRB 091127.

The last option is to let the microphysical parameter ϵ_B vary in time. To be consistent with our measurement of the cooling break speed, the fraction of energy in the magnetic field would have to rise in time as $\epsilon_B \propto t^{0.49}$. Such an evolution would influence the flux as $F_\nu \propto \epsilon_B^{3/4}$ for $\nu < \nu_c$ while the flux density is independent of ϵ_B for $\nu > \nu_c$. Therefore the temporal index before the cooling break passage would decrease by 0.37 on top of the theoretical flux density evolution. This flattening of the temporal index in the $\nu < \nu_c$ regime would explain the early shallow optical/NIR decay, while the late data after the jet break would not be influenced by an evolving ϵ_B. We can again use Eq. 11 in Sari et al. (1998) to estimate the value of ϵ_B, assuming $E_{52} = 1.6$ and $n_1 = 1$. The calculation results in $\epsilon_B = 0.013$ at $t = 3.4$ ks, a value consistent with standard models, and $\epsilon_B = 0.088$ at $t = 107.4$ ks.

There is a growing number of studies which have modelled broad-band GRB light curves, and these have yielded results for ϵ_B which span several orders of magnitude between different GRBs, with values from $\sim 10^{-5}$ to $\sim 10^{-1}$ (Panaitescu and Kumar, 2001, 2002; Yost et al., 2003), raising questions whether the assumption of ϵ_B being constant in the simplest fireball model is consistent with the observations. Lately, the idea of ϵ_B increasing in time as a power-law has been discussed and is receiving increasing support from observational data (e.g., Panaitescu et al., 2006a; Kong et al., 2010). There is also the possibility that all the parameters that influence the cooling frequency vary in time simultaneously. However, it would require more sophisticated theoretical work to derive some estimates or constraints on the ratios between them; our data cannot provide such constraints.

The discussion so far was based on the assumption that the environment around the burst is the undisturbed ISM, i.e. the radial density profile is constant. While this

assumption is supported by the closure relations and the direction of the spectral break, we must consider also the possibility that the circum-burst density has a wind profile. In that case we would expect from the theory the cooling break to move towards shorter wavelengths as $\nu_c \propto t^{0.5}$. To be consistent with our measurement of $t^{-1.23}$, the parameters in Eq. 4.3 would have to increase in time so rapidly, that they would effectively reverse the direction of the cooling break movement. Given that we concluded that the time evolution of parameter E is too dramatic in the ISM scenario, the even more rapid increase required here is more unlikely. To reverse the cooling break movement, ϵ_B would have to increase its time evolution to $t^{1.15}$. While we cannot completely rule out this option due to the inability to compute the exact values of ϵ_B in evolving density, we believe that such rapid time evolution would be difficult to defend against the ISM scenario.

4.5 Conclusions

Since the launch of the *Swift* satellite, there is growing evidence that the radiative mechanism responsible for the optical to X-ray GRB emission is not as simple and well understood as previously believed. The growing number of well-sampled data sets (Chapter 3, Covino et al., 2010; Guidorzi et al., 2009; Thöne et al., 2010) is beginning to place strong constraints on the fireball model and possible alternatives (e.g., Dar and De Rujula, 2000; Dado et al., 2009). Most GRBs have complex light curves, for which the optical and X-ray emission are seemingly decoupled, thus providing an indication that they are produced by different mechanisms. The afterglow of GRB 091127 is one of the few examples in which the light-curve evolution in the optical/NIR and X-ray wavelengths is well represented by a broken power-law and, in addition, both light curves show a break at roughly the same time and similar decay slopes after that break. This observational evidence, together with the fact that the optical/NIR to X-ray SED at late times is well represented by a single component, leads us to an assumption that the emission in both energy bands has been produced by the same radiative mechanism and that this mechanism could be the standard external shock synchrotron radiation.

We observe a clear break in the light curve at around 33 ks, which we interpret as a jet break, based on the fact that it is achromatic and the post-break evolution of all bands is similar. The GROND SEDs show a strong color evolution with the optical/NIR spectral index rising from roughly 0.25 to 0.75, while the X-ray spectral slope stays constant. The broad-band NIR to X-ray SEDs were fitted with a broken power-law with the break moving in time towards larger wavelengths. Because the difference between the low- and high-energy spectral index reaches 0.5 asymptotically, we interpret the spectral break as the cooling break, decreasing in energy with time, as the forward shock moves into an ISM-like circumburst medium. Since it takes almost all the follow-up time for the optical/NIR spectral slope to gradually steepen from the initial value to the value consistent with the X-ray spectral index, we conclude that the cooling break is very smooth in frequency space.

The measured cooling break speed of $\nu_c \propto t^{-1.23\pm0.06}$ is faster than expected for a

shock evolving in a constant density medium and requires that one of the parameters that influence the afterglow flux density evolves with time. We conclude that the required changes in the energy release E_{iso} alone would be too dramatic to be physically plausible and that the most feasible explanation is the evolution of microphysical parameters. Assuming ϵ_B (the fraction of the energy carried by the magnetic field) to be the only varying parameter, then during the time interval that we measure the position of the cooling break, between 3 and 107 ks, it would rise in time as $\epsilon_B \propto t^{0.49}$, and would reach values of 0.01 and 0.09 at those times, respectively.

Currently, a complete understanding of the microphysical processes is still lacking. Nonetheless, data from instruments like *Swift* and GROND can shed some light on the shock physics. A larger study of the observational data of bursts similar to GRB 091127 is necessary to investigate how commonly such changes in ϵ_B occur in GRB afterglows. Theoretical studies would be warranted to investigate effects which would change ϵ_B as the fireball expands into its surrounding environment.

Chapter 5

GRB 091029: At the limit of the fireball scenario

ABSTRACT

Using high-quality, broad-band afterglow data for GRB 091029, we investigate the light curve and broad-band spectra evolution of this afterglow and test the validity of the synchrotron fireball model for gamma-ray bursts. We used multi-wavelength (NIR to X-ray) follow-up observations obtained with GROND simultaneously in the $g'r'i'z'JHK_s$ filters, Bootes-3 and Stardome optical telescopes based in New Zealand, and the XRT onboard the *Swift* satellite in the 0.3 to 10 keV energy range. The resulting data of excellent accuracy allow to construct multi-wavelength light curve with relative photometric errors as low as 1% as well as the spectral energy distribution well-sampled over 5 decades in energy. The optical/NIR and the X-ray light curves of the afterglow of GRB 091029 are nearly totally decoupled. The X-ray light curve shows a shallow rise with a peak at ~ 7.4 ks and a decay slope of 1.20 ± 0.04 afterwards, while the optical/NIR light curve shows an early rise with a peak around 400 ks, followed by a shallow decay with temporal index of $\alpha = 0.58 \pm 0.01$, a bump between $5 - 20$ ks and a decay with slope of $\alpha = 1.12 \pm 0.02$ afterwards. The optical/NIR spectral index decreases gradually from 0.57 ± 0.04 to 0.26 ± 0.03 between 0.4 and 9 ks, and then slowly increases again to a value of 0.49 ± 0.12 at around 100 ks, while the X-ray spectral index remains constant throughout the observations. To explain decoupled light curves in X-ray and optical/NIR domains, a two-component outflow is proposed. Several models are tested, including continuous energy injection, components with different electron energy indices and components in two different stages of the spectral evolution. Only the last model can explain both the decoupled light curves with asynchronous peaks and the peculiar SED evolution. However, this model has so many unknown free parameters that we are unable to reliably confirm or disprove its validity, making the afterglow of GRB 091029 difficult to explain in the frame of the fireball shock model. This conclusion provides further evidence that the standard fireball model with its simplistic assumptions may not be able to model the growing number of well-sampled afterglow light curves.

5.1 Introduction

Since the first GRB was discovered in the late 1960's (Klebesadel et al., 1973), the GRB field has evolved rapidly. This was mainly thanks to three generations of satellites. The Compton Gamma-Ray Observatory was launched in 1991 and with its instrument BATSE showed that GRBs are isotropically distributed in the sky, suggesting they might have a cosmological origin (Meegan et al., 1992). This claim was confirmed in 1997 by Beppo-SAX, an Italian-Dutch satellite that detected and localized GRBs in the X-ray wavelengths (Costa et al., 1997) and enabled the ground-based telescopes to perform follow-up observations (van Paradijs et al., 1997), including redshift measurements that confirmed the cosmological distances of these events (Metzger et al., 1997; Kulkarni et al., 1998). Until the launch of the *Swift* satellite (Gehrels et al., 2004), the early evolutionary stages of GRB afterglows remained unknown.

The *Swift* satellite allows for a study of the afterglow emission starting very early after it is detected by its Burst Alert Telescope (BAT, Barthelmy et al., 2005), thanks to the rapid slewing capability of the vessel and a precise localization of the afterglow by onboard telescopes sensitive at X-ray (XRT, Burrows et al., 2005b) and ultraviolet/optical (UVOT, Roming et al., 2005) wavelengths. Since its launch in 2004, *Swift* has performed many follow-up observations and provided many early and well-sampled afterglow light curves and X-ray spectra.

The Gamma-Ray burst Optical Near-infrared Detector (GROND, Greiner et al., 2008, 2007) provides high-quality, very well-sampled data in seven bands simultaneously since 2007, when it was mounted at the 2.2 m MPI/ESO telescope at La Silla observatory in Chile. The high-precision data obtained by GROND allow for a detailed study of afterglow data as well as time evolution of the spectral energy distribution (SED), thus providing tools to test the standard fireball scenario and its modifications.

Here we provide details of the *Swift*/XRT, GROND, Bootes-3 and Stardome observations of the afterglow of GRB 091029 and discuss the light curves and SEDs in the context of the fireball model thanks to very good energy coverage and sampling of our high-quality data. Throughout the paper, we adopt the convention that the flux density of the GRB afterglow can be described as $F_\nu(t) \propto t^{-\alpha}\nu^{-\beta}$, where α is the temporal and β the spectral index. Unless stated otherwise in the text, all reported errors are at 1σ confidence level.

5.2 Observations

5.2.1 Swift

The *Swift*/BAT was triggered by the long GRB 091029 at $T_0 = 03:53:22$ UT and started immediately slewing to the burst (Grupe et al., 2009). The mask-weighted light curve shows three overlapping peaks, starting at $T_0 - 10$ s and ending at $T_0 + 70$ s, with peaks at $T_0 + 2$, $+20$, and $+26$ s. The measured T_{90} (15-350 keV) is 39.2 ± 5 s (Barthelmy et al., 2009). The BAT prompt emission spectrum from $T_0 - 1.8$ to $T_0 + 60.2$ s is best

fitted using a power-law with an exponential cutoff. This fit gives a photon index of 1.46 ± 0.27 and an $E_{peak} = 61.4 \pm 17.5$ keV. For this model the total fluence in the 15-150 keV energy range is $2.4 \pm 0.1 \times 10^{-6}$ erg/cm^2 (Barthelmy et al., 2009). Using standard concordance cosmology ($H_0 = 71.0$ km/s/Mpc, $\Omega_M = 0.27$, $\Omega_\Lambda = 0.73$, Komatsu et al. (2009)), and a redshift of $z = 2.752$ (Chornock et al., 2009), the bolometric (1keV - 10MeV) energy release of GRB 091029 is $E_{iso} = 8.33 \times 10^{52}$ erg, with a rest-frame E_{peak} of ~ 150 keV.

The *Swift*/XRT started observations of the field of GRB 091029 79.3 s after the trigger (Grupe et al., 2009). XRT data were obtained from the public *Swift* archive and reduced in the standard manner using the xrtpipeline task from the HEAsoft package, with response matrices from the most recent CALDB release. The XRT light curve was obtained from the XRT light curve repository (Evans et al., 2007, 2009a). Spectra were grouped using the grppha task and fitted with the GROND data in XSPEC v12 using χ^2 statistics. The combined optical/X-ray spectral energy distributions (SEDs) were fitted with power-law and broken power-law models and two absorbing columns: one Galactic foreground with a hydrogen column of $N_H = 1.14 \times 10^{20}$ cm^{-2} (Kalberla et al., 2005) and another one that is local to the GRB host galaxy at $z = 2.75$. Only the latter was allowed to vary in the fits. To investigate the dust reddening in the GRB environment, the zdust model was used, which contains Large and Small Magellanic Clouds (LMC, SMC) and Milky Way (MW) extinction laws from Pei (1992).

5.2.2 GROND

The Gamma-Ray burst Optical Near-infrared Detector (GROND, Greiner et al., 2008, 2007) at the 2.2 m MPI/ESO telescope at LaSilla observatory responded to the *Swift* GRB alert and initiated automated observations at 03:57 UT, 4.5 m after the trigger (Filgas et al., 2009a), and imaged the field of GRB 091029 at seven later epochs. A variable point source was detected in all bands by the automated GROND pipeline (Yoldaş et al., 2008). The position of the transient was calculated to be R.A. (J2000) = 04:00:42.62 and Dec (J2000) = −55:57:20.0 compared to USNO-B reference field stars (Monet et al., 2003) with an astrometric uncertainty of $0\rlap{.}''3$.

The optical and NIR image reduction and photometry were performed using standard IRAF tasks (Tody, 1993) similar to the procedure described in detail in Krühler et al. (2008). A general model for the point-spread function (PSF) of each image was constructed using bright field stars and fitted to the afterglow. In addition, aperture photometry was carried out, and the results were consistent with the reported PSF photometry. All data were corrected for a Galactic foreground reddening of $E_{B-V} = 0.016$ mag in the direction of the burst (Schlegel et al., 1998), corresponding to an extinction of $A_V = 0.05$ using $R_V = 3.1$, and in the case of JHK_s data, transformed to AB magnitudes. Optical photometric calibration was performed relative to the magnitudes of four secondary standards in the GRB field, shown in Fig. 5.1 and Table 5.1. During photometric conditions, an SDSS field (Smith et al., 2002) at R.A. (J2000) = 03:50:03.25, Dec (J2000) = −00:00:37.9 was observed within a few minutes of observations of the
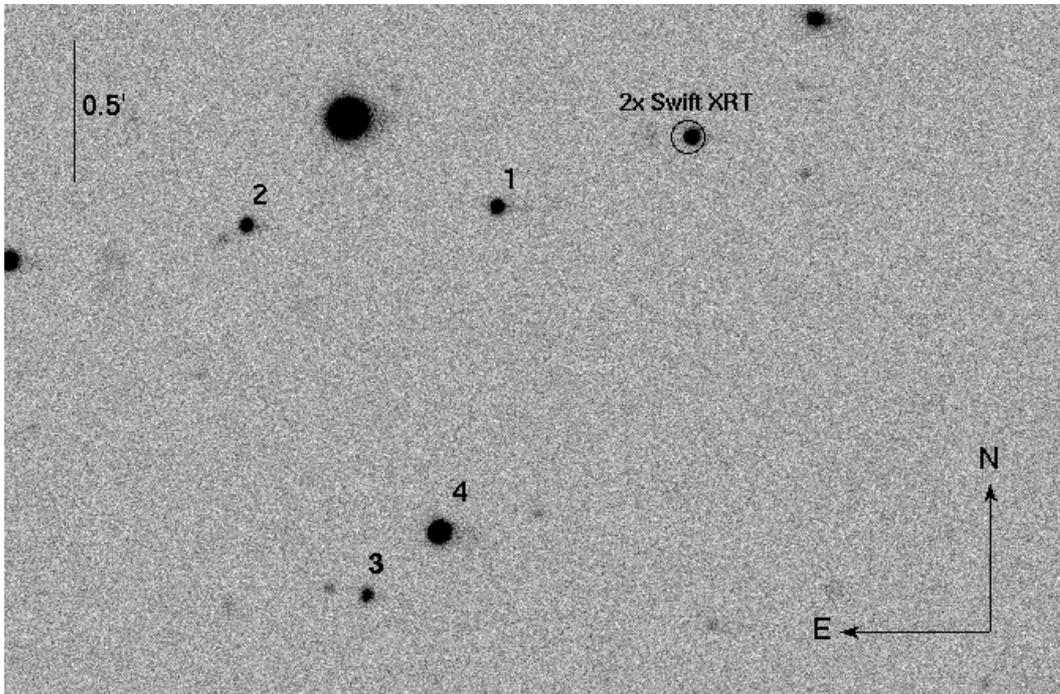
Figure 5.1 GROND g' band image of the field of GRB 091029 obtained 463 s after T_0. The optical afterglow is shown inside the *Swift* XRT error circle with double diameter for better clarity. The secondary standard stars are numbered from 1 to 4 and their magnitudes reported in Table 5.1.

GRB field. The obtained zeropoints were corrected for atmospheric extinction and used to calibrate stars in the GRB field. The apparent magnitudes of the afterglow were measured with respect to the secondary standards reported in Table 5.1. The absolute calibration of JHK_s bands was obtained with respect to magnitudes of the Two Micron All Sky Survey (2MASS) stars within the GRB field obtained from the 2MASS catalog (Skrutskie et al., 2006). All data are listed in Tables 6.5 and 6.6.

5.2.3 Stardome and Bootes-3

The afterglow was observed with the Stardome 0.4 m telescope, located in Auckland (New Zealand, Northern Island), using a SBIG ST-L-6303E CCD. Images were obtained through a SG530 filter that transmits wavelengths above 5300 Angstroms. The observations consisted of 600 s exposures that were combined in sets of 3 to improve the S/N ratio. Image reduction was done using standard techniques in IRAF and we performed aperture photometry using an aperture equivalent to the seeing of the image using PHOT.

Further observations were obtained with the Yock-Allen robotic telescope BOOTES-3, a fast slewing 0.6 m Ritchey-Chrétien telescope equipped with an iXon-889 EMCCD

Table 5.1 Secondary standards in the GRB 091029 field in the GROND filter bands used for the calibration

Star number	R.A., Dec [J2000]	g' (mag$_{AB}$)	r' (mag$_{AB}$)	i' (mag$_{AB}$)	z' (mag$_{AB}$)
1	04:00:47.46, −55:57:35.1	18.50 ± 0.04	17.03 ± 0.03	16.31 ± 0.06	15.92 ± 0.04
2	04:00:53.70, −55:57:39.2	18.63 ± 0.04	18.14 ± 0.03	17.98 ± 0.06	17.85 ± 0.05
3	04:00:50.68, −55:58:57.3	19.25 ± 0.04	18.95 ± 0.03	18.92 ± 0.07	18.89 ± 0.06
4	04:00:48.90, −55:58:43.8	16.28 ± 0.04	15.75 ± 0.03	15.66 ± 0.06	15.55 ± 0.04

Star number	R.A., Dec [J2000]	J (mag$_{Vega}$)	H (mag$_{Vega}$)	K_s (mag$_{Vega}$)
1	04:00:37.34, −56:01:20.6	13.03 ± 0.03	12.67 ± 0.03	12.62 ± 0.03
2	04:00:39.43, −55:56:02.0	12.95 ± 0.03	12.65 ± 0.03	12.58 ± 0.03
3	04:00:45.75, −55:55:34.7	13.35 ± 0.03	13.07 ± 0.03	12.96 ± 0.03
4	04:00:47.49, −55:57:35.0	14.66 ± 0.03	13.98 ± 0.03	13.80 ± 0.03

camera located in Blenheim (New Zealand, Southern Island). The observations consisted of a series of 60 s unfiltered exposures, which were combined in groups to improve the S/N ratio. Image reduction was done using standard techniques in IRAF and we performed aperture photometry using an aperture equivalent to the seeing of the image using PHOT. All data were then cross-calibrated using GROND photometry to obtain consistent results.

5.3 Results

5.3.1 Afterglow light curve

The X-ray light curve of the afterglow of GRB 091029 (Fig. 5.2) shows a very steep decay ($\alpha = 3.69 \pm 0.10$) until ~ 200 s, consistent with being a tail of the GRB emission, connecting the prompt phase of GRB and its afterglow (see Fig. 1.6). After the decay follows a steep X-ray flash, which declines rapidly with $\alpha = 3.91 \pm 0.39$. Given that temporal decay indices before the flash and after its peak are within 1σ consistent, the possible scenario for this rapid rebrightening might involve a refreshed shock (Rees and Meszaros, 1998; Panaitescu et al., 1998; Sari and Mészáros, 2000; Kumar and Piran, 2000; Zhang and Mészáros, 2002b). This early part of the X-ray light curve is of no interest for this work and is therefore excluded from all fittings. The X-ray light curve after ~ 700 s (Fig. 5.3) is best fitted with a broken power-law with a smooth break (Beuermann et al., 1999). The best-fit (red. $\chi^2 = 0.89$) values of this model are $\alpha_{X1} = -0.12 \pm 0.10$, $t_{break} = 7.4 \pm 1.8$ ks and $\alpha_{X2} = 1.20 \pm 0.04$. The smoothness s iterated to a value of 1, which was set as a lower limit for the fit to better constrain the values of temporal decay indices before and after the break.

The optical/NIR light curve of the GRB 091029 afterglow shows an initial rise from the start of the observations until the peak at around 400 s. The temporal slope of the rising, obtained from a simultaneous fit of all optical/NIR bands, is $\alpha = -0.54 \pm 0.07$ but there is a systematic error of non-quantifiable size due to the short coverage of this rising
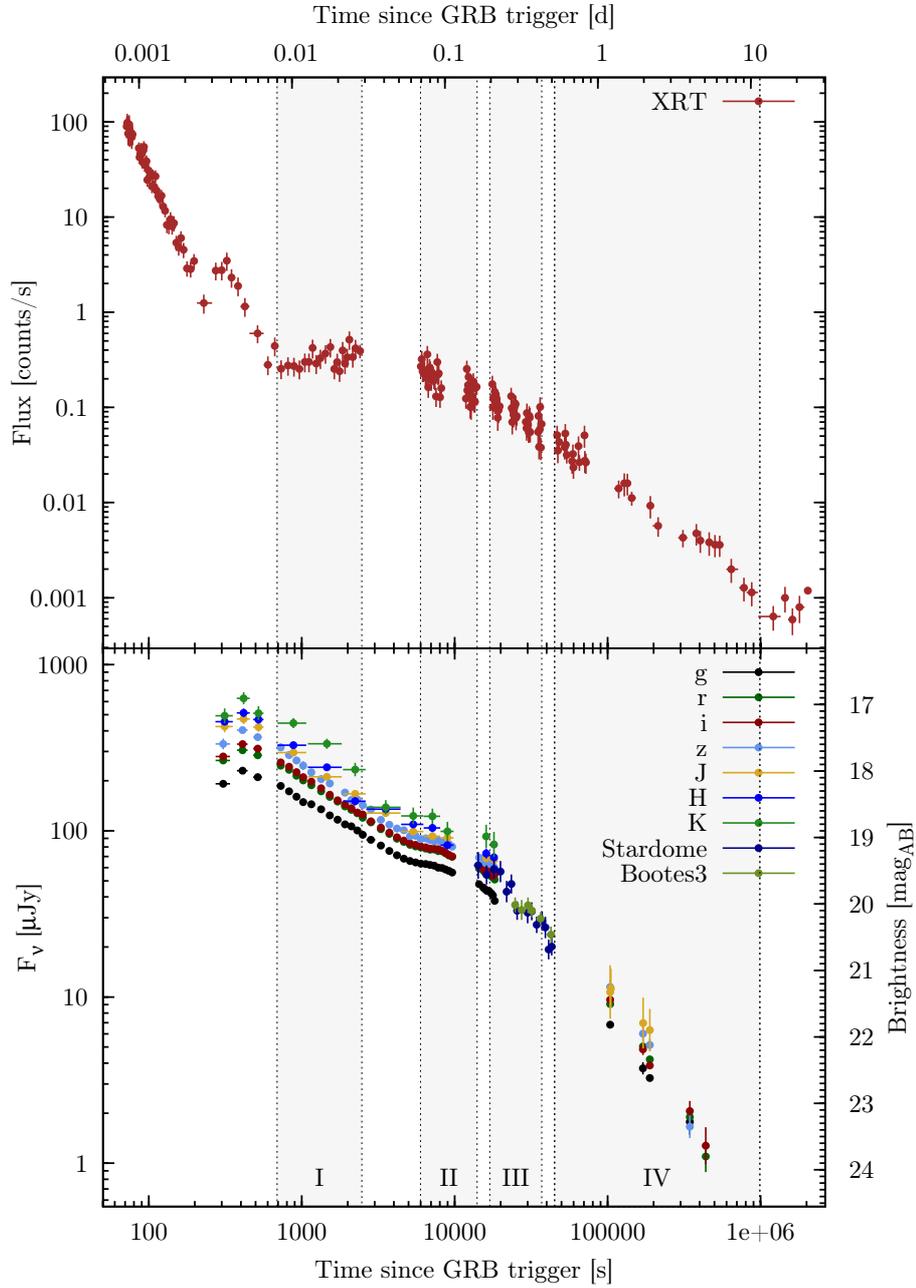
Figure 5.2 Light curve of the X-ray (top panel) and GROND, Bootes-3 and Stardome optical/NIR (bottom panel) afterglow of GRB 091029. Shown data are corrected for Galactic foreground extinction and are in AB magnitudes. Upper limits are not shown for better clarity. Gray regions show the time intervals where XRT data were obtained for the broad-band SEDs (Fig. 5.6).
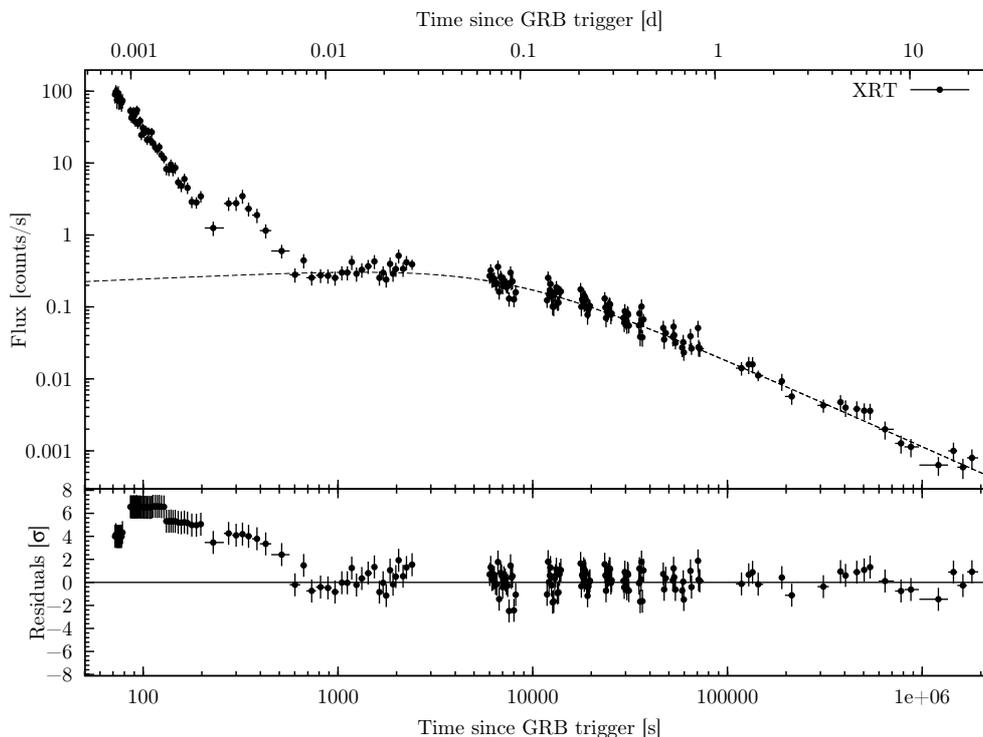
Figure 5.3 The smoothly broken power-law fit to the X-ray light curve of the GRB 091029 afterglow. The fitting was done to datapoints after 700 ks in order to exclude early steep transition phase and flaring.

part. The early peak in the optical/NIR light curve is probably not the counterpart of the X-ray flare due to the time shift of both peaks. The following decay from the initial peak until the bump starting at around 5 ks has a slope of $\alpha = 0.58 \pm 0.01$, obtained from the joint fit of datapoints between $0.6 - 5$ ks in all bands simultaneously. However, fitting this shallow decay phase in each optical/NIR band separately shows a steepening of the temporal index with the increasing wavelength of GROND filters (see Table 5.2), suggesting a color evolution. To fit the data after the hump at around 10 ks, we used just the r' band data together with the Stardome and Bootes-3 data, which were cross-calibrated to be consistent with the r' band, and fill the daytime gap in the GROND data. The best fit (red. $\chi^2 = 1.43$) to data after 20 ks with a straight power-law results in a decay index of $\alpha = 1.12 \pm 0.02$, consistent within 2σ with the decay of the X-ray afterglow at his time.

To fit the whole complex optical/NIR light curve from the beginning to the end of observations, a two-component model is needed. The first component is composed of three smoothly connected power-laws. The second component was needed to model the later hump and steep decay and uses two smoothly connected power-laws. The obtained parameters of this fit (red. $\chi^2 = 0.91$) are listed in the Table 5.3 and discussed later.
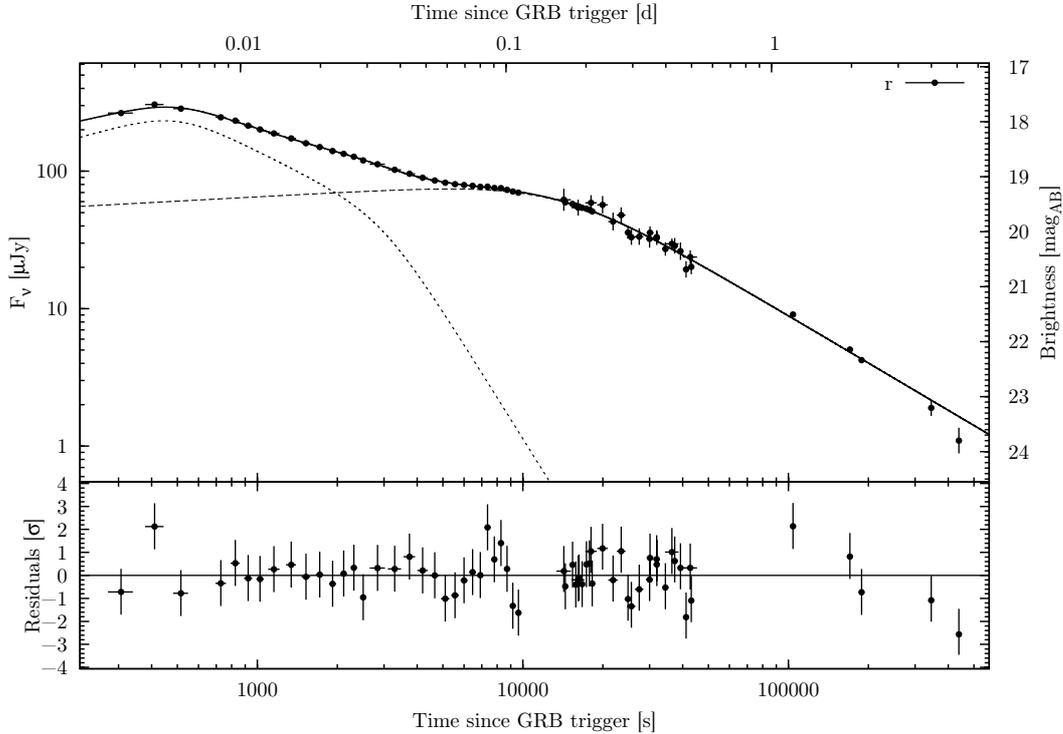
Figure 5.4 The two-component fit to the r' band data obtained by GROND, Stardome and Bootes-3. The parameters of the fit for both components (dotted lines) are listed in Table 5.3. The solid line represents the superposition of the two components and the best fit to the data.

Table 5.2 Light curve fit parameters for the afterglow of GRB 091029 in the time interval of $0.6 - 5$ ks. The fitting of the NIR bands is affected by the somewhat lower signal-to-noise ratio of the NIR data as compared to the optical bands.

Bands	α	χ^2/d.o.f.
g'r'i'z'JHK	0.576 ± 0.004	68 / 71
g'	0.542 ± 0.009	2.9 / 15
r'	0.574 ± 0.006	5.1 / 15
i'	0.593 ± 0.010	3.2 / 15
z'	0.622 ± 0.018	6.1 / 14
J	0.601 ± 0.028	0.8 / 2
H	0.672 ± 0.047	9.6 / 2
K	0.815 ± 0.075	2.9 / 2

5.3.2   Afterglow SEDs

Given that the difference in decay slopes for each GROND filter point to a color evolution, we need to study the SEDs of the afterglow. Thanks to the simultaneous

Table 5.3 Light curve fit parameters for the whole set of r' band data obtained by GROND, Stardome and Bootes-3.

$F_\nu(t)$	α_1	$t_1[ks]$	s_1	α_2	$t_2[ks]$	s_2	α_3
TPL[a]	-0.54 (fixed)	0.49 ± 0.02	3.7 ± 0.9	0.97 ± 0.06	2.96 ± 0.32	2.4 ± 1.0	3.10 ± 0.56
DPL[b]	-0.10 ± 0.01	13.80 ± 0.48	2.0 ± 0.1	1.14 ± 0.02			

[a] Smoothly connected triple power-law

[b] Smoothly connected double power-law
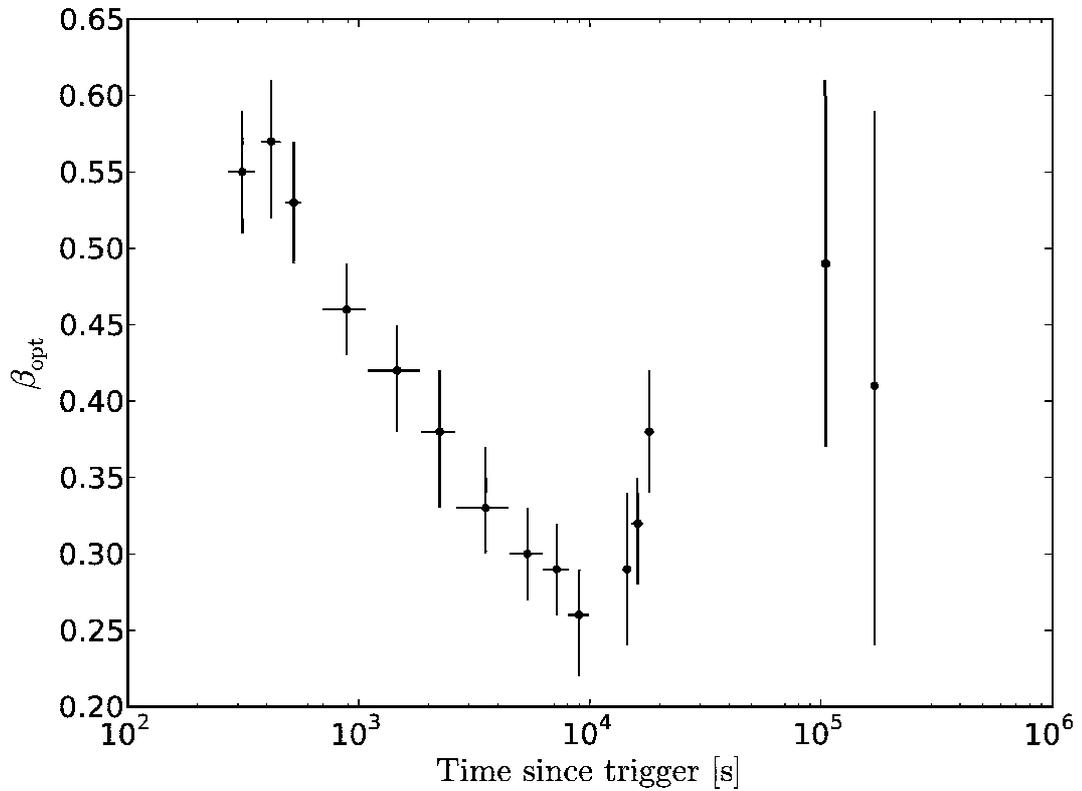
Figure 5.5 The optical/NIR spectral slope as a function of time.

multi-band observing capabilities of GROND, it is possible to measure the spectral slope β of the optical/NIR data as a function of time. Fig. 5.5 shows that the optical/NIR spectral index decreases from 0.57 ± 0.04 to 0.26 ± 0.03 between 0.4 and 9 ks, and then slowly increases again to a value of 0.49 ± 0.12 at around 100 ks. In addition, broad-band optical/NIR to X-ray SEDs were constructed at four different time intervals within this period, which are indicated in the light curve (Fig. 5.2). Fits of optical/NIR data alone as well as the broad-band fits resulted in a host dust extinction that was consistent with zero, therefore in all the models we assumed no host dust extinction for simplicity. The

g' band data were excluded from the fit because they show a signature of a Lyman-alpha break (Lamb and Reichart, 2000), which XSPEC does not support.
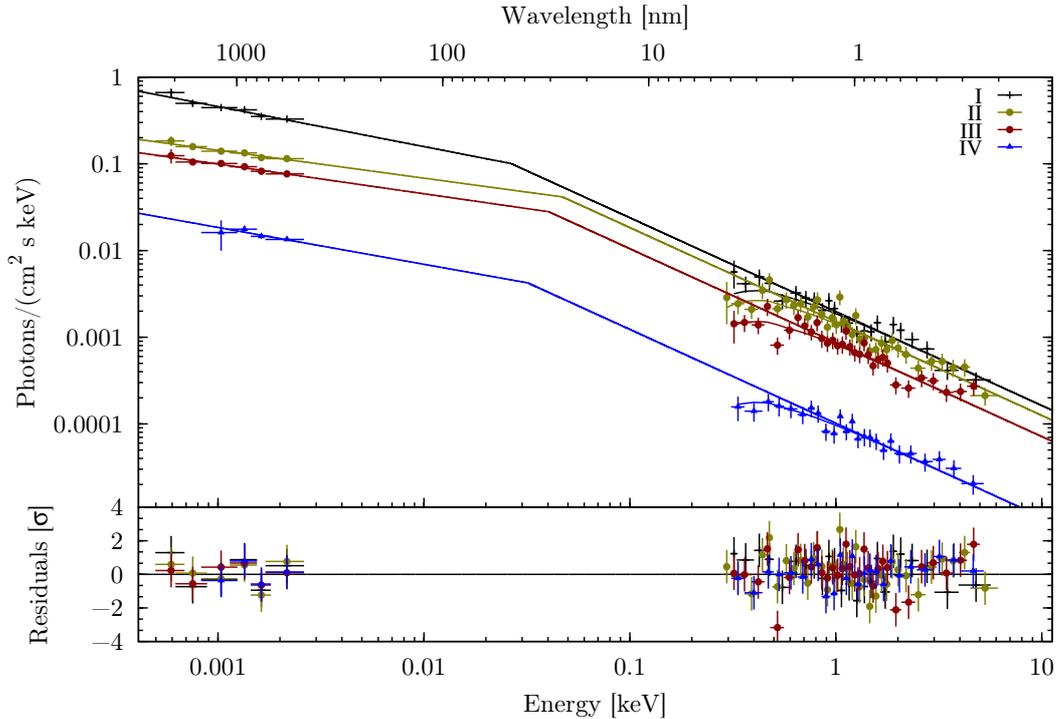
Figure 5.6 Broad-band optical/NIR to X-ray SEDs fitted with a broken power-law. Mid-times of each SED are listed in Table 5.4 and regions where the X-ray data were taken for each SED are shown in Fig. 5.2.

Because the broad-band SEDs proved to be inconsistent with a simple power-law model, we used models that include a break between the X-ray and optical/NIR data. We fitted all four epochs of broad-band SEDs simultaneously with a sharp broken power-law model, where the host-intrinsic absorbing column density and the X-ray spectral index are tied between each SED but left free to vary (Fig. 5.6). The low energy spectral indices and energy of the break were left untied between SEDs and free to vary. The best fit (red. $\chi^2 = 0.94$) gives values of the host-equivalent neutral hydrogen density $N_H = (3.0 \pm 1.3) \times 10^{21}$ cm^{-2} and the high-energy spectral index $\beta_X = 1.08^{+0.06}_{-0.05}$. The best-fit values of low-energy spectral indices and break energies are listed in Table 5.4. This fit shows that the break evolves in time to shorter wavelengths between SEDs I and II, and then it evolves the opposite way towards longer wavelengths between SEDs II and IV.

Table 5.4 Best-fit parameters resulting from the broken power-law fit to the broad-band SEDs. The host-equivalent neutral hydrogen density $N_H = (3.0 \pm 1.3) \times 10^{20}$ cm^{-2}

SED number	Midtime [s] of SED	Low energy spectral index	Cooling break [eV]	High energy spectral index
I	883	$0.46^{+0.06}_{-0.06}$	$26.4^{+15.2}_{-9.8}$	
II	7161	$0.32^{+0.05}_{-0.06}$	$47.2^{+20.8}_{-14.5}$	$1.08^{+0.06}_{-0.05}$
III	18056	$0.34^{+0.06}_{-0.06}$	$40.4^{+19.9}_{-13.1}$	
IV	104026	$0.42^{+0.23}_{-0.21}$	$31.6^{+115.5}_{-17.0}$	

5.3.3 Closure relations

Using values obtained in the fittings we can test the closure relations (Granot and Sari, 2002; Dai and Cheng, 2001; Zhang and Mészáros, 2004; Racusin et al., 2009) between temporal and spectral indices. Assuming the break in the broad-band SEDs to be the cooling break ν_c, we see that the X-ray data are above this frequency and the optical/NIR data below it during the afterglow observations. The fit-derived X-ray spectral index $\beta_X = 1.08^{+0.06}_{-0.05}$ results in a power-law index of the electron energy distribution $p = 2.17 \pm 0.11$. This spectral index and the late X-ray temporal slope of $\alpha_{X2} = 1.20 \pm 0.04$ are within 1σ consistent with the equation (Racusin et al., 2009) for $p > 2$ and a constant decay in the $\nu > \nu_c$ regime, where the jet is interacting with either a homogeneous interstellar medium (ISM) or a wind and is in the slow or fast cooling phase.

The late ($t > 20$ ks) optical/NIR single-component model decay index of $\alpha = 1.12 \pm 0.02$ and the late spectral index of $\beta = 0.49 \pm 0.12$ are within 1σ consistent with the equation for a normal decay in the $\nu_m < \nu < \nu_c$ regime, where the jet is interacting with a wind medium and is in the slow cooling phase. However, during the early shallow decay in the optical/NIR bands, the spectral index is evolving with time and thus cannot be tested with the simple closure relations. In the case of the two-component scenario (Fig. 5.4), the resulting spectral index β is the superposition of the spectral indices of the narrow and the wide jet and evolves with time as the ratio between these two jets changes. Without knowing the spectral indices of each component, the closure relations cannot be tested.

5.4 Discussion

The nearly-total decoupling of the optical/NIR and the X-ray light curves of the afterglow of GRB 091029 suggests a double outflow origin (Chapter 3, Huang et al., 2004; Peng et al., 2005; Sheth et al., 2003; Jin et al., 2007; Wu et al., 2005). That is supported by our finding that the X-ray spectral hardness does not evolve synchronously

with the optical spectral hardening at $0.3 - 10$ ks. We discuss three possible scenarios, all based on a two-component jet, to explain the peculiar behavior of the light curve and the spectrum of this afterglow.

5.4.1   Continuous energy injection

In this scenario, the X-ray light curve after 700 s is produced by the wider, X-ray dominating outflow, which has a deceleration time of a few ks. The pre-deceleration phase of the wide jet would cause the early shallow rise with the peak around 7.4 ks, after which the wide jet would turn into normal deceleration producing the $\alpha_{X2} \sim 1.2$ decay. The same principle would apply for the early optical light curve, where the early rise and peak at ~ 400 s would be a result of a pre-deceleration phase of the narrower, optically dominating outflow. From this peak time, we can calculate the initial Lorentz factor (Molinari et al., 2007) to be $\Gamma_n \sim 153$, substituting the measured quantities and normalizing to the typical values $n = 1$ cm^{-3} and $\eta = 0.2$ (Bloom et al., 2003). The shallow decay of the optical/NIR light curve until 10 ks is then a result of some form of a continuous energy injection by the central engine (Rees and Meszaros, 1998; Dai and Lu, 1998; Panaitescu et al., 1998; Sari and Mészáros, 2000; Zhang and Mészáros, 2001). When this energy injection in the narrow jet ends at ~ 20 ks, the temporal slope steepens to $\alpha \sim 1.1$, characteristic for a normal decay. However, this scenario cannot explain the time evolution of the optical/NIR spectral index during the injection time interval. The hardening of the optical spectrum would require that the electron index p changes in the outflow with time and after the injection ends, it changes back to its original value (Fig. 5.5), a scenario which so far has never been advocated.

5.4.2   Two outflows with different p parameters

The second scenario uses the two-component fit to the optical light curve (Fig. 5.4). The first component would represent a narrow, ultra-relativistic jet, with deceleration time of ~ 400 s, a normal decay phase afterwards, and a jet break at ~ 3.7 ks, followed by a steep post-jet break decay. The second component represents a wider and mildly relativistic jet with the deceleration time of ~ 14 ks and a normal decay. While the residuals in Fig. 5.4 might hint on a possible jet break of the wider component around 100 ks, the data are within 3σ of the straight power-law and there is no visible break in the X-ray data at that time, therefore we cannot make a reliable statement about this possible jet break. The narrow jet would be dominant in the early part of the light curve and the wide one would be responsible for the late hump and dominate the optical/NIR light curve afterwards. The shallow decay between $0.4 - 5$ ks would be a result of the superposition of fluxes from both outflows. This model can explain the flattening of the spectral index during this period, assuming that each outflow with different Lorentz factor has a different electron energy distribution index p. As the ratio between the narrow jet with a higher p value ($p \sim 2.1$) and the wide jet with a lower p value ($p \sim 1.5$) changes, the spectral index of the co-added flux is gradually evolving as well. However, this model does not explain the turnover of the spectral evolution at

~ 10 ks, where only the wide component with a constant p is dominant. It is also not consistent with the X-ray spectral index β_X being constant, independently of the ratio between the two jets. Even if we assume the wide jet to have a spectral cut-off and its influence being negligible in the X-ray domain, though the narrow jet has the p value consistent with the X-ray flux, their light curves are completely decoupled.

5.4.3 Passage of ν_m through optical bands

The third scenario uses the same two-component jet setup as the second one (Fig. 5.4) but both outflows have the same value of $p \sim 2.1$ and are at different stages of the synchrotron spectra evolution (Fig. 1.5). The flattening of the SEDs II and III in optical/NIR region (Fig. 5.6) would then be a result of the wide jet having both the cooling break ν_c and the injection frequency ν_m between the X-ray and optical/NIR wavelengths. In that case, the spectral slope in the optical/NIR bands of the narrow jet would be $\beta_X - 0.5 = 0.58 \pm 0.06$ and of the wide jet would be $-1/3$ (Sari et al., 1998). As the ratio between these two outflows changes, it would explain the spectral hardening in the optical/NIR bands, while being consistent with the X-ray spectral slope staying constant thanks to equal p values in both outflows. The turnover in the spectral evolution at ~ 10 ks can be explained by the passage of the frequency ν_m through the GROND filters, after which the optical/NIR spectral index would be consistent with the narrow jet. Given that the softening of the optical/NIR spectrum after ~ 10 ks is slow and gradual, the spectral break at the frequency ν_m must be very smooth (Granot and Sari, 2002, Chapter 4).

This model can also explain different break times in the X-ray and optical/NIR domains, assuming that the deceleration time of the wide jet is defined by the X-ray light curve peak but the movement of the break ν_m is neglecting the expected decay steepening in the optical/NIR bands until it passes through them and causes the late break in the light curve. However, this scenario is difficult to confirm or disprove by fitting the light curve and SEDs because this model has a huge number of unknown free parameters. Therefore it is very difficult to fit the broad-band SEDs with a model consisting of a double power-law and a triple power-law component and constrain all the five slopes and three break frequencies reliably. The fitting of light curves is confronted with similar difficulties. The optical/NIR light curve is in this case a superposition of two triple broken power-laws representing each of the jets. The late decay slope of the wide jet is the only parameter that is well constrained, the early rising and the first break can be estimated from the fit to the X-ray data but the errors are quite large. The middle power-law, representing the phase between the deceleration time of the wide jet and ν_m crossing the optical/NIR bands, can be estimated from the closure relations. Given that the latest decay phase is consistent with the wind environment, we can assume the wind medium also in the earlier times of the afterglow emission. The closure relations for the $\nu_a < \nu < \nu_m$ regime, slow cooling and $p > 2$ give the temporal decay slope of $\alpha = 0$ (Zhang and Mészáros, 2004), independent of β. The parameters of the narrow jet can only be obtained as the superposition of the two jets is fitted

to the optical/NIR light curve and their reliability is therefore fully dependent on the goodness of the estimates of the parameters of the narrow jet.

5.5 Conclusions

The growing number of well-sampled data sets from the latest generation of instruments like the *Swift* satellite and GROND imager show that the radiative mechanism responsible for the optical to X-ray GRB emission is not as simple and well understood as previously believed. Lately, the simplest fireball model has an increasing difficulty to explain the complex light curves of some GRB afterglows. In many cases, the optical and X-ray emission are seemingly decoupled, thus providing an indication that they are produced by different mechanisms. The afterglow of GRB 091029 is an extreme case, where the optical/NIR and the X-ray light curves are almost totally decoupled, as if they belonged to two different GRBs. Moreover, the GROND SEDs show a strong color evolution with the optical/NIR spectral index decreasing from roughly 0.57 to 0.26 between 0.4 and 9 ks, and then increasing again to a value of ~ 0.49 at around 100 ks, while the X-ray spectral index remains constant throughout the observations. This observational evidence leads us to an assumption that the emission in both energy bands has been produced by two different outflows.

We discuss several possible scenarios to explain this peculiar afterglow. The first one includes the continuous energy injection in order to explain the shallow initial decay of the optical/NIR light curve. However, this model is not able to explain the spectral evolution during the injection period, given that the theory assumes the electron energy distribution index p of the outflow constant. To solve this, the second scenario uses two components with different p values. As the ratio between these two outflows changes, the resulting spectral index changes as well. This model is, however, not able to explain neither the turnover in the spectral slope evolution, nor the different times of the breaks in the X-ray and optical/NIR light curves. The third scenario offers a solution by putting the two outflows with similar p values into two different stages of the spectral evolution. The narrow jet, dominating the optical/NIR wavelengths before the hump, has a cooling break between the optical and the X-ray bands, while the wide jet, responsible for the X-ray emission and the late optical/NIR light curve, has both ν_c and ν_m frequencies between the optical and the X-ray bands. During the hump, the injection frequency ν_m passes through the GROND filters and the light curve becomes similar to the X-ray one.

Even though the last model can in principle explain all the irregularities of the afterglow of GRB 091029, its complexity does not allow us to test it reliably with the presented dataset. Currently, there is no general model that would be able to model all the GRB afterglows. The data from instruments like *Swift*/XRT and GROND put increasing constraints on the favored fireball shock scenario. A larger study of the observational data of GRB afterglows is necessary to investigate whether the more and more expanded fireball model is consistent with the measurements.

Chapter 6

Summary and Outlook

While this thesis showed the constrains that the new generation of detectors, with GROND in the lead, put on the standard fireball shock model, it is focused on analysis of individual bursts. The next steps will require to combine a statistically significant sample of afterglow data. Using this sample of afterglows detected by both GROND and *Swift*, the physics of GRBs can be addressed in a systematic way. With such dataset, presenting an unprecedented time and frequency coverage, the morphology of afterglow light curves can be studied in great detail. We can measure at what time do the achromatic breaks, associated with jet breaks, occur, and what are the typical temporal decay indices before and after these breaks. We can study how often do the chromatic breaks happen and what is their possible cause, how different or similar is the early evolution of the optical light curve compared to the X-ray light curve, etc.

Thanks to the multi-wavelength capability of GROND, we can study the temporal evolution of the spectral index in the optical/NIR domain. Although the *Swift*/XRT has similar capabilities in the X-ray domain, spectral evolution has only been observed during the tail of the prompt emission, flares and supernovae bumps. GROND on the other hand detects spectral evolution even during normal decay phases of most of the afterglows and therefore allows to measure positions of spectral breaks with high time resolution. Having both the temporal decay index α and the spectral index β for a large fraction of detected bursts, the standard fireball model can be tested using the closure relations. This way we can conclusively answer the main question raised in this thesis: is the standard fireball shock model consistent with a large dataset of well-sampled afterglows in both the optical and X-ray regimes, or are the complex additions and modifications to this model just further complications of a fundamentally deficient model? The work on such study already started, using the analysis tools described in Chapter 2. Fig. 6.1 shows a small example of preliminary light curves, their fits and temporal evolutions of spectral indices. The number of light curves is constantly growing as more data are reduced and more afterglows observed.

A complete sample of GRBs can be used for studies which are outside of the frame of this thesis, like the redshift distribution, the average amount of the dust extinction, the nature of optically dark or short bursts, the average properties of host galaxies, the
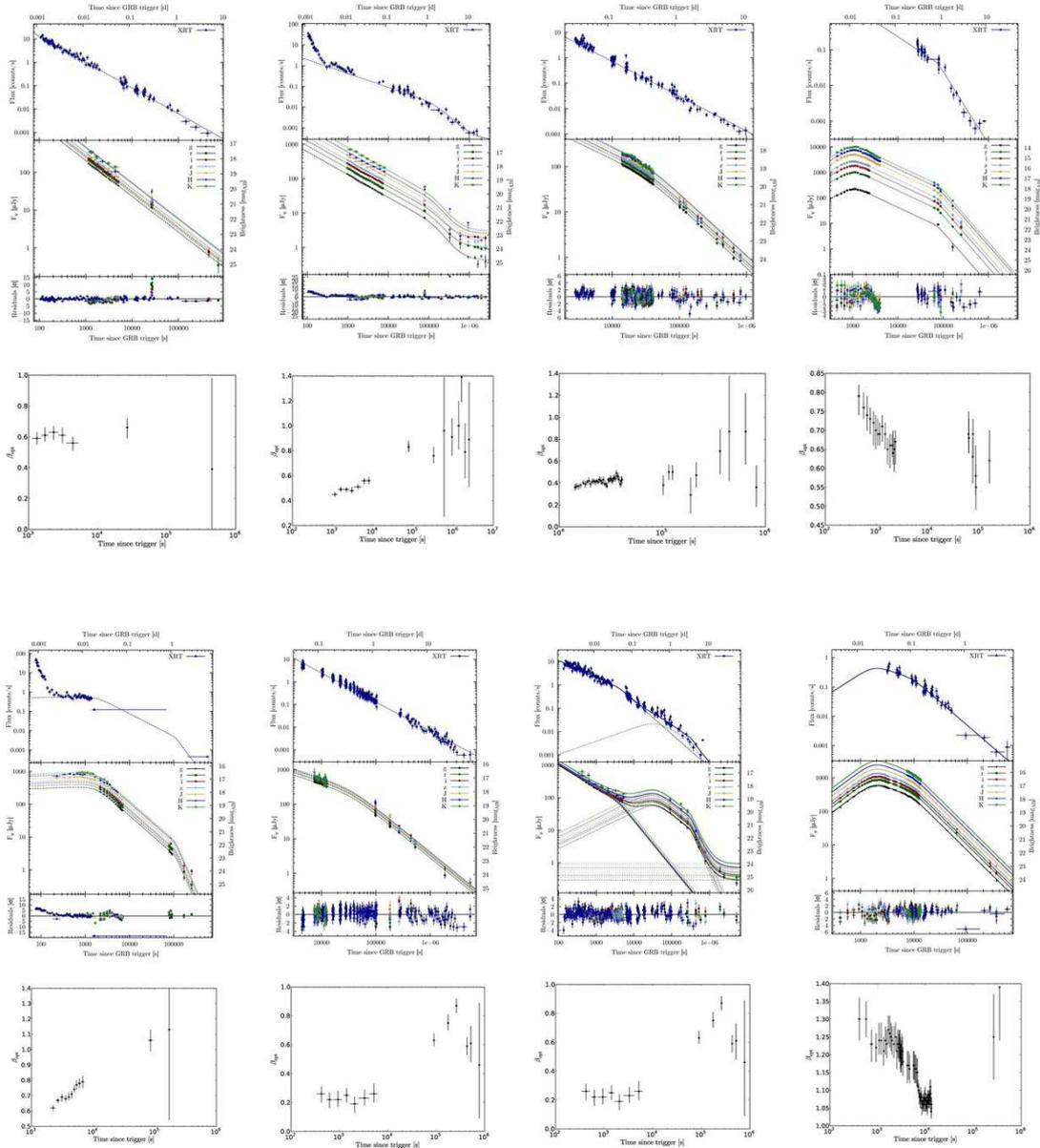
Figure 6.1 Example of preliminary light curves of several afterglows chosen for the sample study. **Upper figures of both rows:** Top panels represent XRT data, middle panels GROND data and bottom panels residuals to the fits. **Bottom figures of both rows:** Spectral indices of bursts as a function of time.

dust to gas ratio in the burst environment, the connection between the GRB and cosmic star-formation rates, and much more. Even with a large statistical sample, the study of individual bursts will lose nothing of its importance, GRBs with very high redshifts

will always be the most exciting example. They can provide information about the dark ages of the Universe, not accessible by other means than GRBs.

Even after 40 years since their discovery, GRBs remain one of the most exciting objects in the astronomy field, their characteristics still not fully understood. Combining the data from the dedicated space telescopes like the *Swift* and now the *Fermi* and from the increasing number of ground-based follow-up telescopes, promises to provide a better understanding of GRB physics in the time frame of a few years.

Bibliography

Akerlof, C., Balsano, R., Barthelmy, S., Bloch, J., Butterworth, P., Casperson, D., Cline, T., Fletcher, S., Frontera, F., Gisler, G., Heise, J., Hills, J., Kehoe, R., Lee, B., Marshall, S., McKay, T., Miller, R., Piro, L., Priedhorsky, W., Szymanski, J., and Wren, J.: 1999, *Nature* **398**, 400

Amati, L., Frontera, F., Tavani, M., in't Zand, J. J. M., Antonelli, A., Costa, E., Feroci, M., Guidorzi, C., Heise, J., Masetti, N., Montanari, E., Nicastro, L., Palazzi, E., Pian, E., Piro, L., and Soffitta, P.: 2002, *A&A* **390**, 81

Band, D., Matteson, J., Ford, L., Schaefer, B., Palmer, D., Teegarden, B., Cline, T., Briggs, M., Paciesas, W., Pendleton, G., Fishman, G., Kouveliotou, C., Meegan, C., Wilson, R., and Lestrade, P.: 1993, *ApJ* **413**, 281

Barthelmy, S. D., Barbier, L. M., Cummings, J. R., Fenimore, E. E., Gehrels, N., Hullinger, D., Krimm, H. A., Markwardt, C. B., Palmer, D. M., Parsons, A., Sato, G., Suzuki, M., Takahashi, T., Tashiro, M., and Tueller, J.: 2005, *Space Sci. Rev.* **120**, 143

Barthelmy, S. D., Baumgartner, W., Cummings, J., Fenimore, E., Gehrels, N., Krimm, H., Markwardt, C., McLean, K., Palmer, D., Sakamoto, T., Sato, G., Stamatikos, M., Tueller, J., and Ukwatta, T.: 2008, *GRB Coordinates Network* **7606**, 1

Barthelmy, S. D., Baumgartner, W. H., Cummings, J. R., Fenimore, E. E., Gehrels, N., Grupe, D., Krimm, H. A., Markwardt, C. B., Palmer, D. M., Parsons, A. M., Sakamoto, T., Sato, G., Stamatikos, M., Tueller, J., and Ukwatta, T. N.: 2009, *GRB Coordinates Network* **10103**, 1

Barthelmy, S. D., Cline, T. L., Butterworth, P., Kippen, R. M., Briggs, M. S., Connaughton, V., and Pendleton, G. N.: 2000, in R. M. Kippen, R. S. Mallozzi, & G. J. Fishman (ed.), *Gamma-ray Bursts, 5th Huntsville Symposium*, Vol. 526 of *American Institute of Physics Conference Series*, pp 731–735

Berger, E., Chornock, R., Holmes, T. R., Foley, R. J., Cucchiara, A., Wolf, C., Podsiadlowski, P., Fox, D. B., and Roth, K. C.: 2011, *ArXiv e-prints*

Berger, E., Kulkarni, S. R., Pooley, G., Frail, D. A., McIntyre, V., Wark, R. M., Sari, R., Soderberg, A. M., Fox, D. W., Yost, S., and Price, P. A.: 2003, *Nature* **426**, 154

Bertin, E. and Arnouts, S.: 1996, *A&AS* **117**, 393

Beuermann, K., Hessman, F. V., Reinsch, K., Nicklas, H., Vreeswijk, P. M., Galama, T. J., Rol, E., van Paradijs, J., Kouveliotou, C., Frontera, F., Masetti, N., Palazzi, E., and Pian, E.: 1999, *A&A* **352**, L26

Blandford, R. and Eichler, D.: 1987, *Physics Reports* **154**, 1

Bloom, J. S., Frail, D. A., and Kulkarni, S. R.: 2003, *ApJ* **594**, 674

Bloom, J. S., Kulkarni, S. R., and Djorgovski, S. G.: 2002, *AJ* **123**, 1111

Blustin, A. J., Band, D., Barthelmy, S., Boyd, P., Capalbi, M., Holland, S. T., Marshall, F. E., Mason, K. O., Perri, M., Poole, T., Roming, P., Rosen, S., Schady, P., Still, M., Zhang, B., Angelini, L., Barbier, L., Beardmore, A., Breeveld, A., Burrows, D. N., Cummings, J. R., Cannizzo, J., Campana, S., Chester, M. M., Chincarini, G., Cominsky, L. R., Cucchiara, A., de Pasquale, M., Fenimore, E. E., Gehrels, N., Giommi, P., Goad, M., Gronwall, C., Grupe, D., Hill, J. E., Hinshaw, D., Hunsberger, S., Hurley, K. C., Ivanushkina, M., Kennea, J. A., Krimm, H. A., Kumar, P., Landsman, W., La Parola, V., Markwardt, C. B., McGowan, K., Mészáros, P., Mineo, T., Moretti, A., Morgan, A., Nousek, J., O'Brien, P. T., Osborne, J. P., Page, K., Page, M. J., Palmer, D. M., Parsons, A. M., Rhoads, J., Romano, P., Sakamoto, T., Sato, G., Tagliaferri, G., Tueller, J., Wells, A. A., and White, N. E.: 2006, *ApJ* **637**, 901

Bolzonella, M., Miralles, J.-M., and Pelló, R.: 2000, *A&A* **363**, 476

Brennan, T., Reichart, D., Nysewander, M., Lacluyze, A., Ivarsen, K., Crain, J. A., Schubel, M., Foster, A., Haislip, J., Styblova, J., and Trotter, A.: 2008, *GRB Coordinates Network* **7629**, 1

Burrows, D. N., Hill, J. E., Chincarini, G., Tagliaferri, G., Campana, S., Moretti, A., Romano, P., Malesani, D., Racusin, J. L., Kobayashi, S., Zhang, B., Mészáros, P., O'Brien, P. T., Willingale, R., Osborne, J. P., Cusumano, G., Giommi, P., Angelini, L., Abbey, A. F., Antonelli, L. A., Beardmore, A. P., Capalbi, M., Covino, S., D'Avanzo, P., Goad, M. R., Kennea, J. A., Morris, D. C., Pagani, C., Page, K. L., Stella, L., Nousek, J. A., Wells, A. A., and Gehrels, N.: 2005a, *ApJL* **622**, L85

Burrows, D. N., Hill, J. E., Nousek, J. A., Kennea, J. A., Wells, A., Osborne, J. P., Abbey, A. F., Beardmore, A., Mukerjee, K., Short, A. D. T., Chincarini, G., Campana, S., Citterio, O., Moretti, A., Pagani, C., Tagliaferri, G., Giommi, P., Capalbi, M., Tamburelli, F., Angelini, L., Cusumano, G., Bräuninger, H. W., Burkert, W., and Hartner, G. D.: 2005b, *Space Sci. Rev.* **120**, 165

Burrows, D. N. and Racusin, J.: 2006, *Nuovo Cimento B Serie* **121**, 1273

Campana, S., Mangano, V., Blustin, A. J., Brown, P., Burrows, D. N., Chincarini, G., Cummings, J. R., Cusumano, G., Della Valle, M., Malesani, D., Mészáros, P.,

Nousek, J. A., Page, M., Sakamoto, T., Waxman, E., Zhang, B., Dai, Z. G., Gehrels, N., Immler, S., Marshall, F. E., Mason, K. O., Moretti, A., O'Brien, P. T., Osborne, J. P., Page, K. L., Romano, P., Roming, P. W. A., Tagliaferri, G., Cominsky, L. R., Giommi, P., Godet, O., Kennea, J. A., Krimm, H., Angelini, L., Barthelmy, S. D., Boyd, P. T., Palmer, D. M., Wells, A. A., and White, N. E.: 2006, *Nature* **442**, 1008

Castro-Tirado, A. J., Zapatero-Osorio, M. R., Caon, N., Cairos, L. M., Hjorth, J., Pedersen, H., Andersen, M. I., Gorosabel, J., Bartolini, C., Guarnieri, A., Piccioni, A., Frontera, F., Masetti, N., Palazzi, E., Pian, E., Greiner, J., Hudec, R., Sagar, R., Pandey, A. K., Mohan, V., Yadav, R. K. S., Nilakshi, N., Bjornsson, G., Jakobsson, P., Burud, I., Courbin, F., Valentini, G., Piersimoni, A., Aceituno, J., Montoya, L. M., Pedraz, S., Gredel, R., Claver, C. F., Rector, T. A., Rhoads, J. E., Walter, F., Ott, J., Hippelein, H., Sanchez-Bejar, V., Gutierrez, C., Oscoz, A., Zhu, J., Chen, J., Zhang, H., Wei, J., Zhou, A., Guziy, S., Shlyapnikov, A., Heise, J., Costa, E., Feroci, M., and Piro, L.: 1999, *Science* **283**, 2069

Cavallo, G. and Rees, M. J.: 1978, *MNRAS* **183**, 359

Chavan, A. M., Silva, D. R., Boarotto, C., Canavan, T., Kemp, R., and Giannone, G.: 2000, in P. J. Quinn (ed.), *Society of Photo-Optical Instrumentation Engineers (SPIE) Conference Series*, Vol. 4010 of *Society of Photo-Optical Instrumentation Engineers (SPIE) Conference Series*, pp 81–89

Chevalier, R. A. and Li, Z.-Y.: 1999, *ApJL* **520**, L29

Chevalier, R. A. and Li, Z.-Y.: 2000, *ApJ* **536**, 195

Chornock, R., Perley, D. A., and Cobb, B. E.: 2009, *GRB Coordinates Network* **10100**, 1

Cobb, B. E., Bloom, J. S., Perley, D. A., Morgan, A. N., Cenko, S. B., and Filippenko, A. V.: 2010, *ApJL* **718**, L150

Cohen, E., Piran, T., and Sari, R.: 1998, *ApJ* **509**, 717

Costa, E., Frontera, F., Heise, J., Feroci, M., in't Zand, J., Fiore, F., Cinti, M. N., Dal Fiume, D., Nicastro, L., Orlandini, M., Palazzi, E., Rapisarda#, M., Zavattini, G., Jager, R., Parmar, A., Owens, A., Molendi, S., Cusumano, G., Maccarone, M. C., Giarrusso, S., Coletta, A., Antonelli, L. A., Giommi, P., Muller, J. M., Piro, L., and Butler, R. C.: 1997, *Nature* **387**, 783

Covino, S., Campana, S., Conciatore, M. L., D'Elia, V., Palazzi, E., Thöne, C. C., Vergani, S. D., Wiersema, K., Brusasca, M., Cucchiara, A., Cobb, B. E., Fernández-Soto, A., Kann, D. A., Malesani, D., Tanvir, N. R., Antonelli, L. A., Bremer, M., Castro-Tirado, A. J., de Ugarte Postigo, A., Molinari, E., Nicastro, L., Stefanon, M., Testa, V., Tosti, G., Vitali, F., Amati, L., Chapman, R., Conconi, P., Cutispoto, G., Fynbo, J. P. U., Goldoni, P., Henriksen, C., Horne, K. D., Malaspina, G., Meurs,

E. J. A., Pian, E., Stella, L., Tagliaferri, G., Ward, P., and Zerbi, F. M.: 2010, *A&A* **521**, A53+

Cucchiara, A., Fox, D., Levan, A., and Tanvir, N.: 2009, *GRB Coordinates Network* **10202**, 1

Cucchiara, A., Fox, D. B., and Cenko, S. B.: 2008, *GRB Coordinates Network* **7615**, 1

Cucchiara, A., Levan, A. J., Fox, D. B., Tanvir, N. R., Ukwatta, T. N., Berger, E., Krühler, T., Küpcü Yoldaş, A., Wu, X. F., Toma, K., Greiner, J., Olivares, F. E., Rowlinson, A., Amati, L., Sakamoto, T., Roth, K., Stephens, A., Fritz, A., Fynbo, J. P. U., Hjorth, J., Malesani, D., Jakobsson, P., Wiersema, K., O'Brien, P. T., Soderberg, A. M., Foley, R. J., Fruchter, A. S., Rhoads, J., Rutledge, R. E., Schmidt, B. P., Dopita, M. A., Podsiadlowski, P., Willingale, R., Wolf, C., Kulkarni, S. R., and D'Avanzo, P.: 2011, *ApJ* **736**, 7

Dado, S., Dar, A., and De Rújula, A.: 2009, *ApJ* **696**, 994

Dai, Z. G. and Cheng, K. S.: 2001, *ApJL* **558**, L109

Dai, Z. G. and Lu, T.: 1998, *Physical Review Letters* **81**, 4301

Dai, Z. G. and Lu, T.: 2002, *ApJL* **565**, L87

Dai, Z. G. and Wu, X. F.: 2003, *ApJL* **591**, L21

Dar, A. and De Rujula, A.: 2000, *ArXiv Astrophysics e-prints*

de Pasquale, M., Piro, L., Gendre, B., Amati, L., Antonelli, L. A., Costa, E., Feroci, M., Frontera, F., Nicastro, L., Soffitta, P., and in't Zand, J.: 2006, *A&A* **455**, 813

de Ugarte Postigo, A., Castro-Tirado, A. J., Gorosabel, J., Jóhannesson, G., Björnsson, G., Gudmundsson, E. H., Bremer, M., Pak, S., Tanvir, N., Castro Cerón, J. M., Guzyi, S., Jelínek, M., Klose, S., Pérez-Ramírez, D., Aceituno, J., Campo Bagatín, A., Covino, S., Cardiel, N., Fathkullin, T., Henden, A. A., Huferath, S., Kurata, Y., Malesani, D., Mannucci, F., Ruiz-Lapuente, P., Sokolov, V., Thiele, U., Wisotzki, L., Antonelli, L. A., Bartolini, C., Boattini, A., Guarnieri, A., Piccioni, A., Pizzichini, G., del Principe, M., di Paola, A., Fugazza, D., Ghisellini, G., Hunt, L., Konstantinova, T., Masetti, N., Palazzi, E., Pian, E., Stefanon, M., Testa, V., and Tristram, P. J.: 2005, *A&A* **443**, 841

D'Elia, V., Baumgartner, W. H., Beardmore, A. P., Gehrels, N., Gelbord, J. M., Holland, S. T., Kennea, J. A., Krimm, H. A., Kuin, N. P. M., Markwardt, C. B., Palmer, D. M., Siegel, M. H., and Stratta, G.: 2011, *GRB Coordinates Network* **11699**, 1

Devillard, N.: 1997, *The Messenger* **87**, 19

Eichler, D., Livio, M., Piran, T., and Schramm, D. N.: 1989, *Nature* **340**, 126

Evans, P. A., Beardmore, A. P., Page, K. L., Osborne, J. P., O'Brien, P. T., Willingale, R., Starling, R. L. C., Burrows, D. N., Godet, O., Vetere, L., Racusin, J., Goad, M. R., Wiersema, K., Angelini, L., Capalbi, M., Chincarini, G., Gehrels, N., Kennea, J. A., Margutti, R., Morris, D. C., Mountford, C. J., Pagani, C., Perri, M., Romano, P., and Tanvir, N.: 2009a, *MNRAS* **397**, 1177

Evans, P. A., Beardmore, A. P., Page, K. L., Tyler, L. G., Osborne, J. P., Goad, M. R., O'Brien, P. T., Vetere, L., Racusin, J., Morris, D., Burrows, D. N., Capalbi, M., Perri, M., Gehrels, N., and Romano, P.: 2007, *A&A* **469**, 379

Evans, P. A., Page, K. L., and Troja, E.: 2009b, *GRB Coordinates Network* **10201**, 1

Filgas, R., Greiner, J., and Updike, A.: 2010, *GRB Coordinates Network* **10652**, 1

Filgas, R., Updike, A., and Greiner, J.: 2009a, *GRB Coordinates Network* **10098**, 1

Filgas, R., Updike, A., Rau, A., and Greiner, J.: 2009b, *GRB Coordinates Network* **10091**, 1

Fishman, G. J. and Meegan, C. A.: 1995, *ARA&A* **33**, 415

Fox, D. W., Price, P. A., Soderberg, A. M., Berger, E., Kulkarni, S. R., Sari, R., Frail, D. A., Harrison, F. A., Yost, S. A., Matthews, K., Peterson, B. A., Tanaka, I., Christiansen, J., and Moriarty-Schieven, G. H.: 2003a, *ApJL* **586**, L5

Fox, D. W., Yost, S., Kulkarni, S. R., Torii, K., Kato, T., Yamaoka, H., Sako, M., Harrison, F. A., Sari, R., Price, P. A., Berger, E., Soderberg, A. M., Djorgovski, S. G., Barth, A. J., Pravdo, S. H., Frail, D. A., Gal-Yam, A., Lipkin, Y., Mauch, T., Harrison, C., and Buttery, H.: 2003b, *Nature* **422**, 284

Frail, D. A., Kulkarni, S. R., Sari, R., Djorgovski, S. G., Bloom, J. S., Galama, T. J., Reichart, D. E., Berger, E., Harrison, F. A., Price, P. A., Yost, S. A., Diercks, A., Goodrich, R. W., and Chaffee, F.: 2001, *ApJL* **562**, L55

Frail, D. A., Waxman, E., and Kulkarni, S. R.: 2000, *ApJ* **537**, 191

Fruchter, A. S., Thorsett, S. E., Metzger, M. R., Sahu, K. C., Petro, L., Livio, M., Ferguson, H., Pian, E., Hogg, D. W., Galama, T., Gull, T. R., Kouveliotou, C., Macchetto, D., van Paradijs, J., Pedersen, H., and Smette, A.: 1999, *ApJL* **519**, L13

Fryer, C. L., Woosley, S. E., and Hartmann, D. H.: 1999, *ApJ* **526**, 152

Fukugita, M., Ichikawa, T., Gunn, J. E., Doi, M., Shimasaku, K., and Schneider, D. P.: 1996, *AJ* **111**, 1748

Fynbo, J. P. U., Jakobsson, P., Prochaska, J. X., Malesani, D., Ledoux, C., de Ugarte Postigo, A., Nardini, M., Vreeswijk, P. M., Wiersema, K., Hjorth, J., Sollerman, J., Chen, H.-W., Thöne, C. C., Björnsson, G., Bloom, J. S., Castro-Tirado, A. J.,

Christensen, L., De Cia, A., Fruchter, A. S., Gorosabel, J., Graham, J. F., Jaunsen, A. O., Jensen, B. L., Kann, D. A., Kouveliotou, C., Levan, A. J., Maund, J., Masetti, N., Milvang-Jensen, B., Palazzi, E., Perley, D. A., Pian, E., Rol, E., Schady, P., Starling, R. L. C., Tanvir, N. R., Watson, D. J., Xu, D., Augusteijn, T., Grundahl, F., Telting, J., and Quirion, P.-O.: 2009, *ApJS* **185**, 526

Galama, T. J., Vreeswijk, P. M., van Paradijs, J., Kouveliotou, C., Augusteijn, T., Böhnhardt, H., Brewer, J. P., Doublier, V., Gonzalez, J.-F., Leibundgut, B., Lidman, C., Hainaut, O. R., Patat, F., Heise, J., in't Zand, J., Hurley, K., Groot, P. J., Strom, R. G., Mazzali, P. A., Iwamoto, K., Nomoto, K., Umeda, H., Nakamura, T., Young, T. R., Suzuki, T., Shigeyama, T., Koshut, T., Kippen, M., Robinson, C., de Wildt, P., Wijers, R. A. M. J., Tanvir, N., Greiner, J., Pian, E., Palazzi, E., Frontera, F., Masetti, N., Nicastro, L., Feroci, M., Costa, E., Piro, L., Peterson, B. A., Tinney, C., Boyle, B., Cannon, R., Stathakis, R., Sadler, E., Begam, M. C., and Ianna, P.: 1998, *Nature* **395**, 670

Gehrels, N., Chincarini, G., Giommi, P., Mason, K. O., Nousek, J. A., Wells, A. A., White, N. E., Barthelmy, S. D., Burrows, D. N., Cominsky, L. R., Hurley, K. C., Marshall, F. E., Mészáros, P., Roming, P. W. A., Angelini, L., Barbier, L. M., Belloni, T., Campana, S., Caraveo, P. A., Chester, M. M., Citterio, O., Cline, T. L., Cropper, M. S., Cummings, J. R., Dean, A. J., Feigelson, E. D., Fenimore, E. E., Frail, D. A., Fruchter, A. S., Garmire, G. P., Gendreau, K., Ghisellini, G., Greiner, J., Hill, J. E., Hunsberger, S. D., Krimm, H. A., Kulkarni, S. R., Kumar, P., Lebrun, F., Lloyd-Ronning, N. M., Markwardt, C. B., Mattson, B. J., Mushotzky, R. F., Norris, J. P., Osborne, J., Paczynski, B., Palmer, D. M., Park, H.-S., Parsons, A. M., Paul, J., Rees, M. J., Reynolds, C. S., Rhoads, J. E., Sasseen, T. P., Schaefer, B. E., Short, A. T., Smale, A. P., Smith, I. A., Stella, L., Tagliaferri, G., Takahashi, T., Tashiro, M., Townsley, L. K., Tueller, J., Turner, M. J. L., Vietri, M., Voges, W., Ward, M. J., Willingale, R., Zerbi, F. M., and Zhang, W. W.: 2004, *ApJ* **611**, 1005

Gendre, B., Galli, A., Corsi, A., Klotz, A., Piro, L., Stratta, G., Boër, M., and Damerdji, Y.: 2007, *A&A* **462**, 565

Ghirlanda, G., Nava, L., Ghisellini, G., and Firmani, C.: 2007, *A&A* **466**, 127

Golenetskii, S., Aptekar, R., Frederiks, D., Mazets, E., Pal'Shin, V., Oleynik, P., Ulanov, M., Svinkin, D., and Cline, T.: 2009, *GRB Coordinates Network* **10209**, 1

Gomboc, A., Guidorzi, C., Melandri, A., Steele, I. A., Mundell, C. G., Bersier, D. F., Bode, M. F., Burgdorf, M. J., Fraser, S. N., Kobayashi, S., Mottram, C. J., Smith, R. J., O'Brien, P., Bannister, N., and Tanvir, N.: 2008, *GRB Coordinates Network* **7626**, 1

Goodman, J.: 1986, *ApJL* **308**, L47

Granot, J., Königl, A., and Piran, T.: 2006, *MNRAS* **370**, 1946

Granot, J. and Kumar, P.: 2003, *ApJ* **591**, 1086

Granot, J., Nakar, E., and Piran, T.: 2003, *Nature* **426**, 138

Granot, J., Panaitescu, A., Kumar, P., and Woosley, S. E.: 2002, *ApJL* **570**, L61

Granot, J. and Sari, R.: 2002, *ApJ* **568**, 820

Greiner, J., Bornemann, W., Clemens, C., Deuter, M., Hasinger, G., Honsberg, M., Huber, H., Huber, S., Krauss, M., Krühler, T., Küpcü Yoldaş, A., Mayer-Hasselwander, H., Mican, B., Primak, N., Schrey, F., Steiner, I., Szokoly, G., Thöne, C. C., Yoldaş, A., Klose, S., Laux, U., and Winkler, J.: 2008, *PASP* **120**, 405

Greiner, J., Bornemann, W., Clemens, C., Deuter, M., Hasinger, G., Honsberg, M., Huber, H., Huber, S., Krauss, M., Krühler, T., Küpcü Yoldas, A., Mayer-Hasselwander, H., Mican, B., Primak, N., Schrey, F., Steiner, I., Szokoly, G., Thöne, C. C., Yoldas, A., Klose, S., Laux, U., and Winkler, J.: 2007, *The Messenger* **130**, 12

Greiner, J., Krühler, T., Fynbo, J. P. U., Rossi, A., Schwarz, R., Klose, S., Savaglio, S., Tanvir, N. R., McBreen, S., Totani, T., Zhang, B. B., Wu, X. F., Watson, D., Barthelmy, S. D., Beardmore, A. P., Ferrero, P., Gehrels, N., Kann, D. A., Kawai, N., Yoldaş, A. K., Mészáros, P., Milvang-Jensen, B., Oates, S. R., Pierini, D., Schady, P., Toma, K., Vreeswijk, P. M., Yoldaş, A., Zhang, B., Afonso, P., Aoki, K., Burrows, D. N., Clemens, C., Filgas, R., Haiman, Z., Hartmann, D. H., Hasinger, G., Hjorth, J., Jehin, E., Levan, A. J., Liang, E. W., Malesani, D., Pyo, T.-S., Schulze, S., Szokoly, G., Terada, K., and Wiersema, K.: 2009a, *ApJ* **693**, 1610

Greiner, J., Krühler, T., Klose, S., Afonso, P., Clemens, C., Filgas, R., Hartmann, D. H., Küpcü Yoldaş, A., Nardini, M., Olivares E., F., Rau, A., Rossi, A., Schady, P., and Updike, A.: 2011, *A&A* **526**, A30+

Greiner, J., Krühler, T., McBreen, S., Ajello, M., Giannios, D., Schwarz, R., Savaglio, S., Yoldaş, A. K., Clemens, C., Stefanescu, A., Sala, G., Bertoldi, F., Szokoly, G., and Klose, S.: 2009b, *ApJ* **693**, 1912

Grupe, D., Burrows, D. N., Wu, X.-F., Wang, X.-Y., Zhang, B., Liang, E.-W., Garmire, G., Nousek, J. A., Gehrels, N., Ricker, G. R., and Bautz, M. W.: 2010, *ApJ* **711**, 1008

Grupe, D., Cummings, J. R., Marshall, F. E., Pagani, C., Palmer, D. M., Siegel, M. H., Stamatikos, M., Ukwatta, T. N., and Vetere, L.: 2009, *GRB Coordinates Network* **10097**, 1

Guetta, D., Fiore, F., D'Elia, V., Perna, R., Antonelli, L. A., Piranomonte, S., Puccetti, S., Stella, L., Angelini, L., Schartel, N., Campana, S., Chincarini, G., Covino, S., Tagliaferri, G., Malesani, D., Guidorzi, C., Monfardini, A., Mundell, C. G., de León

Cruz, J., Castro-Tirado, A. J., Guzly, S., Gorosabel, J., Jelinek, M., and Gomboc, A.: 2007, *A&A* **461**, 95

Guidorzi, C., Clemens, C., Kobayashi, S., Granot, J., Melandri, A., D'Avanzo, P., Kuin, N. P. M., Klotz, A., Fynbo, J. P. U., Covino, S., Greiner, J., Malesani, D., Mao, J., Mundell, C. G., Steele, I. A., Jakobsson, P., Margutti, R., Bersier, D., Campana, S., Chincarini, G., D'Elia, V., Fugazza, D., Genet, F., Gomboc, A., Krühler, T., Küpcü Yoldaş, A., Moretti, A., Mottram, C. J., O'Brien, P. T., Smith, R. J., Szokoly, G., Tagliaferri, G., Tanvir, N. R., and Gehrels, N.: 2009, *A&A* **499**, 439

Harrison, F. A., Yost, S. A., Sari, R., Berger, E., Galama, T. J., Holtzman, J., Axelrod, T., Bloom, J. S., Chevalier, R., Costa, E., Diercks, A., Djorgovski, S. G., Frail, D. A., Frontera, F., Hurley, K., Kulkarni, S. R., McCarthy, P., Piro, L., Pooley, G. G., Price, P. A., Reichart, D., Ricker, G. R., Shepherd, D., Schmidt, B., Walter, F., and Wheeler, C.: 2001, *ApJ* **559**, 123

Heyl, J. S. and Perna, R.: 2003, *ApJL* **586**, L13

Hjorth, J., Sollerman, J., Møller, P., Fynbo, J. P. U., Woosley, S. E., Kouveliotou, C., Tanvir, N. R., Greiner, J., Andersen, M. I., Castro-Tirado, A. J., Castro Cerón, J. M., Fruchter, A. S., Gorosabel, J., Jakobsson, P., Kaper, L., Klose, S., Masetti, N., Pedersen, H., Pedersen, K., Pian, E., Palazzi, E., Rhoads, J. E., Rol, E., van den Heuvel, E. P. J., Vreeswijk, P. M., Watson, D., and Wijers, R. A. M. J.: 2003, *Nature* **423**, 847

Huang, K. Y., Urata, Y., Filippenko, A. V., Hu, J. H., Ip, W. H., Kuo, P. H., Li, W., Lin, H. C., Lin, Z. Y., Makishima, K., Onda, K., Qiu, Y., and Tamagawa, T.: 2005, *ApJL* **628**, L93

Huang, Y. F., Wu, X. F., Dai, Z. G., Ma, H. T., and Lu, T.: 2004, *ApJ* **605**, 300

Immler, S. and Troja, E.: 2009, *GRB Coordinates Network* **10199**, 1

Ioka, K., Kobayashi, S., and Zhang, B.: 2005, *ApJ* **631**, 429

Jin, Z. P., Yan, T., Fan, Y. Z., and Wei, D. M.: 2007, *ApJL* **656**, L57

Johnson, H. L. and Morgan, W. W.: 1953, *ApJ* **117**, 313

Kalberla, P. M. W., Burton, W. B., Hartmann, D., Arnal, E. M., Bajaja, E., Morras, R., and Pöppel, W. G. L.: 2005, *A&A* **440**, 775

Kamble, A., Misra, K., Bhattacharya, D., and Sagar, R.: 2009, *MNRAS* **394**, 214

Kann, D. A., Klose, S., Zhang, B., Malesani, D., Nakar, E., Pozanenko, A., Wilson, A. C., Butler, N. R., Jakobsson, P., Schulze, S., Andreev, M., Antonelli, L. A., Bikmaev, I. F., Biryukov, V., Böttcher, M., Burenin, R. A., Castro Cerón, J. M., Castro-Tirado, A. J., Chincarini, G., Cobb, B. E., Covino, S., D'Avanzo, P., D'Elia,

V., Della Valle, M., de Ugarte Postigo, A., Efimov, Y., Ferrero, P., Fugazza, D., Fynbo, J. P. U., Gålfalk, M., Grundahl, F., Gorosabel, J., Gupta, S., Guziy, S., Hafizov, B., Hjorth, J., Holhjem, K., Ibrahimov, M., Im, M., Israel, G. L., Jelinek, M., Jensen, B. L., Karimov, R., Khamitov, I. M., Kiziloğlu, Ü., Klunko, E., Kubánek, P., Kutyrev, A. S., Laursen, P., Levan, A. J., Mannucci, F., Martin, C. M., Mescheryakov, A., Mirabal, N., Norris, J. P., Ovaldsen, J.-E., Paraficz, D., Pavlenko, E., Piranomonte, S., Rossi, A., Rumyantsev, V., Salinas, R., Sergeev, A., Sharapov, D., Sollerman, J., Stecklum, B., Stella, L., Tagliaferri, G., Tanvir, N. R., Telting, J., Testa, V., Updike, A. C., Volnova, A., Watson, D., Wiersema, K., and Xu, D.: 2010, *ApJ* **720**, 1513

Katz, J. I. and Piran, T.: 1997, *ApJ* **490**, 772

Kaufer, A., Stahl, O., Tubbesing, S., Nørregaard, P., Avila, G., Francois, P., Pasquini, L., and Pizzella, A.: 1999, *The Messenger* **95**, 8

Klebesadel, R. W., Strong, I. B., and Olson, R. A.: 1973, *ApJL* **182**, L85+

Kobayashi, S.: 2000, *ApJ* **545**, 807

Kobayashi, S., Mészáros, P., and Zhang, B.: 2004, *ApJL* **601**, L13

Kobayashi, S. and Sari, R.: 2000, *ApJ* **542**, 819

Kobayashi, S. and Zhang, B.: 2003a, *ApJ* **597**, 455

Kobayashi, S. and Zhang, B.: 2003b, *ApJL* **582**, L75

Komatsu, E., Dunkley, J., Nolta, M. R., Bennett, C. L., Gold, B., Hinshaw, G., Jarosik, N., Larson, D., Limon, M., Page, L., Spergel, D. N., Halpern, M., Hill, R. S., Kogut, A., Meyer, S. S., Tucker, G. S., Weiland, J. L., Wollack, E., and Wright, E. L.: 2009, *ApJS* **180**, 330

Kong, S. W., Wong, A. Y. L., Huang, Y. F., and Cheng, K. S.: 2010, *MNRAS* **402**, 409

Kouveliotou, C., Meegan, C. A., Fishman, G. J., Bhat, N. P., Briggs, M. S., Koshut, T. M., Paciesas, W. S., and Pendleton, G. N.: 1993, *ApJL* **413**, L101

Krimm, H. A., Yamaoka, K., Sugita, S., Ohno, M., Sakamoto, T., Barthelmy, S. D., Gehrels, N., Hara, R., Norris, J. P., Ohmori, N., Onda, K., Sato, G., Tanaka, H., Tashiro, M., and Yamauchi, M.: 2009, *ApJ* **704**, 1405

Kruehler, T., Greiner, J., Kupcu Yoldas, A., Clemens, C., Yoldas, A., and Szokoly, G.: 2008, *GRB Coordinates Network* **7599**, 1

Krühler, T., Greiner, J., Afonso, P., Burlon, D., Clemens, C., Filgas, R., Kann, D. A., Klose, S., Küpcü Yoldaş, A., McBreen, S., Olivares, F., Rau, A., Rossi, A., Schulze, S., Szokoly, G. P., Updike, A., and Yoldaş, A.: 2009, *A&A* **508**, 593

Krühler, T., Greiner, J., Schady, P., Savaglio, S., Afonso, P. M. J., Clemens, C., Elliott, J., Filgas, R., Gruber, D., Kann, D. A., Klose, S., Küpcü-Yoldas, A., McBreen, S., Olivares E., F., Pierini, D., Rau, A., Rossi, A., Nardini, M., Nicuesa Guelbenzu, A., Sudilovsky, V., and Updike, A. C.: 2011a, *ArXiv e-prints*

Krühler, T., Küpcü Yoldaş, A., Greiner, J., Clemens, C., McBreen, S., Primak, N., Savaglio, S., Yoldaş, A., Szokoly, G. P., and Klose, S.: 2008, *ApJ* **685**, 376

Krühler, T., Schady, P., Greiner, J., Afonso, P., Bottacini, E., Clemens, C., Filgas, R., Klose, S., Koch, T. S., Küpcü-Yoldaş, A., Oates, S. R., Olivares E., F., Page, M. J., McBreen, S., Nardini, M., Nicuesa Guelbenzu, A., Rau, A., Roming, P. W. A., Rossi, A., Updike, A., and Yoldaş, A.: 2011b, *A&A* **526**, A153+

Kulkarni, S. R., Djorgovski, S. G., Odewahn, S. C., Bloom, J. S., Gal, R. R., Koresko, C. D., Harrison, F. A., Lubin, L. M., Armus, L., Sari, R., Illingworth, G. D., Kelson, D. D., Magee, D. K., van Dokkum, P. G., Frail, D. A., Mulchaey, J. S., Malkan, M. A., McClean, I. S., Teplitz, H. I., Koerner, D., Kirkpatrick, D., Kobayashi, N., Yadigaroglu, I.-A., Halpern, J., Piran, T., Goodrich, R. W., Chaffee, F. H., Feroci, M., and Costa, E.: 1999, *Nature* **398**, 389

Kulkarni, S. R., Djorgovski, S. G., Ramaprakash, A. N., Goodrich, R., Bloom, J. S., Adelberger, K. L., Kundic, T., Lubin, L., Frail, D. A., Frontera, F., Feroci, M., Nicastro, L., Barth, A. J., Davis, M., Filippenko, A. V., and Newman, J.: 1998, *Nature* **393**, 35

Kumar, P. and Granot, J.: 2003, *ApJ* **591**, 1075

Kumar, P. and Panaitescu, A.: 2000, *ApJL* **541**, L9

Kumar, P. and Piran, T.: 2000, *ApJ* **532**, 286

Küpcü Yoldaş, A., Greiner, J., Klose, S., Krühler, T., and Savaglio, S.: 2010, *A&A* **515**, L2+

Lamb, D. Q. and Reichart, D. E.: 2000, *ApJ* **536**, 1

Landolt, A. U.: 1992, *AJ* **104**, 340

Laursen, L. T. and Stanek, K. Z.: 2003, *ApJL* **597**, L107

Lazzati, D., Perna, R., Flasher, J., Dwarkadas, V. V., and Fiore, F.: 2006, *MNRAS* **372**, 1791

Lazzati, D., Rossi, E., Covino, S., Ghisellini, G., and Malesani, D.: 2002, *A&A* **396**, L5

Li, W., Filippenko, A. V., Chornock, R., and Jha, S.: 2003, *ApJL* **586**, L9

Li, Z.-Y. and Chevalier, R. A.: 2001, *ApJ* **551**, 940

Li, Z.-Y. and Chevalier, R. A.: 2003, *ApJL* **589**, L69

Lipkin, Y. M., Ofek, E. O., Gal-Yam, A., Leibowitz, E. M., Poznanski, D., Kaspi, S., Polishook, D., Kulkarni, S. R., Fox, D. W., Berger, E., Mirabal, N., Halpern, J., Bureau, M., Fathi, K., Price, P. A., Peterson, B. A., Frebel, A., Schmidt, B., Orosz, J. A., Fitzgerald, J. B., Bloom, J. S., van Dokkum, P. G., Bailyn, C. D., Buxton, M. M., and Barsony, M.: 2004, *ApJ* **606**, 381

Liu, R.-Y. and Wang, X.-Y.: 2011, *ApJ* **730**, 1

MacFadyen, A. I. and Woosley, S. E.: 1999, *ApJ* **524**, 262

Malesani, D., Tagliaferri, G., Chincarini, G., Covino, S., Della Valle, M., Fugazza, D., Mazzali, P. A., Zerbi, F. M., D'Avanzo, P., Kalogerakos, S., Simoncelli, A., Antonelli, L. A., Burderi, L., Campana, S., Cucchiara, A., Fiore, F., Ghirlanda, G., Goldoni, P., Götz, D., Mereghetti, S., Mirabel, I. F., Romano, P., Stella, L., Minezaki, T., Yoshii, Y., and Nomoto, K.: 2004, *ApJL* **609**, L5

Meegan, C. A., Fishman, G. J., Wilson, R. B., Horack, J. M., Brock, M. N., Paciesas, W. S., Pendleton, G. N., and Kouveliotou, C.: 1992, *Nature* **355**, 143

Mészáros, P.: 2002, *ARA&A* **40**, 137

Mészáros, P.: 2006, *Reports on Progress in Physics* **69**, 2259

Meszaros, P., Laguna, P., and Rees, M. J.: 1993, *ApJ* **415**, 181

Meszaros, P. and Rees, M. J.: 1992, *ApJ* **397**, 570

Meszaros, P. and Rees, M. J.: 1993a, *ApJL* **418**, L59+

Meszaros, P. and Rees, M. J.: 1993b, *ApJ* **405**, 278

Meszaros, P. and Rees, M. J.: 1997a, *ApJ* **476**, 232

Meszaros, P. and Rees, M. J.: 1997b, *ApJL* **482**, L29+

Mészáros, P. and Rees, M. J.: 1999, *MNRAS* **306**, L39

Meszaros, P., Rees, M. J., and Wijers, R. A. M. J.: 1998, *ApJ* **499**, 301

Metzger, M. R., Djorgovski, S. G., Kulkarni, S. R., Steidel, C. C., Adelberger, K. L., Frail, D. A., Costa, E., and Frontera, F.: 1997, *Nature* **387**, 878

Molinari, E., Vergani, S. D., Malesani, D., Covino, S., D'Avanzo, P., Chincarini, G., Zerbi, F. M., Antonelli, L. A., Conconi, P., Testa, V., Tosti, G., Vitali, F., D'Alessio, F., Malaspina, G., Nicastro, L., Palazzi, E., Guetta, D., Campana, S., Goldoni, P., Masetti, N., Meurs, E. J. A., Monfardini, A., Norci, L., Pian, E., Piranomonte, S., Rizzuto, D., Stefanon, M., Stella, L., Tagliaferri, G., Ward, P. A., Ihle, G., Gonzalez, L., Pizarro, A., Sinclaire, P., and Valenzuela, J.: 2007, *A&A* **469**, L13

Monet, D. G., Levine, S. E., Canzian, B., Ables, H. D., Bird, A. R., Dahn, C. C., Guetter, H. H., Harris, H. C., Henden, A. A., Leggett, S. K., Levison, H. F., Luginbuhl, C. B., Martini, J., Monet, A. K. B., Munn, J. A., Pier, J. R., Rhodes, A. R., Riepe, B., Sell, S., Stone, R. C., Vrba, F. J., Walker, R. L., Westerhout, G., Brucato, R. J., Reid, I. N., Schoening, W., Hartley, M., Read, M. A., and Tritton, S. B.: 2003, *AJ* **125**, 984

Morganson, E., De Rosa, G., Decarli, R., Walter, F., Chambers, K., McGreer, I., Fan, X., Burgett, W., Flewelling, H., Hodapp, K., Kaiser, N., Magnier, E., Price, P., Rix, H.-W., Sweeney, B., and Waters, C.: 2011, *ArXiv e-prints*

Nakar, E. and Granot, J.: 2007, *MNRAS* **380**, 1744

Nakar, E. and Piran, T.: 2003, *ApJ* **598**, 400

Nakar, E., Piran, T., and Granot, J.: 2003, *New Astronomy* **8**, 495

Nardini, M., Ghisellini, G., Ghirlanda, G., Tavecchio, F., Firmani, C., and Lazzati, D.: 2006, *A&A* **451**, 821

Nardini, M., Greiner, J., Krühler, T., Filgas, R., Klose, S., Afonso, P., Clemens, C., Guelbenzu, A. N., Olivares E., F., Rau, A., Rossi, A., Updike, A., Küpcü Yoldaş, A., Yoldaş, A., Burlon, D., Elliott, J., and Kann, D. A.: 2011, *A&A* **531**, A39+

Nousek, J. A., Kouveliotou, C., Grupe, D., Page, K. L., Granot, J., Ramirez-Ruiz, E., Patel, S. K., Burrows, D. N., Mangano, V., Barthelmy, S., Beardmore, A. P., Campana, S., Capalbi, M., Chincarini, G., Cusumano, G., Falcone, A. D., Gehrels, N., Giommi, P., Goad, M. R., Godet, O., Hurkett, C. P., Kennea, J. A., Moretti, A., O'Brien, P. T., Osborne, J. P., Romano, P., Tagliaferri, G., and Wells, A. A.: 2006, *ApJ* **642**, 389

Oates, S. R., de Pasquale, M., Page, M. J., Blustin, A. J., Zane, S., McGowan, K., Mason, K. O., Poole, T. S., Schady, P., Roming, P. W. A., Page, K. L., Falcone, A., and Gehrels, N.: 2007, *MNRAS* **380**, 270

Paciesas, W. S., Meegan, C. A., Pendleton, G. N., Briggs, M. S., Kouveliotou, C., Koshut, T. M., Lestrade, J. P., McCollough, M. L., Brainerd, J. J., Hakkila, J., Henze, W., Preece, R. D., Connaughton, V., Kippen, R. M., Mallozzi, R. S., Fishman, G. J., Richardson, G. A., and Sahi, M.: 1999, *ApJS* **122**, 465

Paczynski, B.: 1986, *ApJL* **308**, L43

Paczynski, B.: 1990, *ApJ* **363**, 218

Paczynski, B.: 1998, *ApJL* **494**, L45+

Page, M., Palmer, D., Barthelmy, S., Burrows, D., Beardmore, A., Kennea, J., Chester, M., and Sakamoto, T.: 2005, *GRB Coordinates Network* **3839**, 1

Panaitescu, A.: 2005, *MNRAS* **363**, 1409

Panaitescu, A. and Kumar, P.: 2000, *ApJ* **543**, 66

Panaitescu, A. and Kumar, P.: 2001, *ApJL* **560**, L49

Panaitescu, A. and Kumar, P.: 2002, *ApJ* **571**, 779

Panaitescu, A. and Kumar, P.: 2004a, *MNRAS* **353**, 511

Panaitescu, A. and Kumar, P.: 2004b, *MNRAS* **350**, 213

Panaitescu, A. and Meszaros, P.: 1998, *ApJ* **501**, 772

Panaitescu, A., Mészáros, P., Burrows, D., Nousek, J., Gehrels, N., O'Brien, P., and Willingale, R.: 2006a, *MNRAS* **369**, 2059

Panaitescu, A., Mészáros, P., Gehrels, N., Burrows, D., and Nousek, J.: 2006b, *MNRAS* **366**, 1357

Panaitescu, A., Meszaros, P., and Rees, M. J.: 1998, *ApJ* **503**, 314

Panaitescu, A. and Vestrand, W. T.: 2008, *MNRAS* **387**, 497

Pei, Y. C.: 1992, *ApJ* **395**, 130

Peng, F., Königl, A., and Granot, J.: 2005, *ApJ* **626**, 966

Perri, M., Barthelmy, S. D., Cummings, J. R., Gehrels, N., Gronwall, C., Holland, S. T., Kennea, J. A., Markwardt, C. B., Mateos, S., Palmer, D. M., Parsons, A. M., Romano, P., Starling, R. L. C., Stratta, G., Ukwatta, T. N., vanden Berk, D. E., and Vergani, S. D.: 2007, *GRB Coordinates Network* **7058**, 1

Piran, T.: 1999, *Physics Reports* **314**, 575

Racusin, J. L., Karpov, S. V., Sokolowski, M., Granot, J., Wu, X. F., Pal'Shin, V., Covino, S., van der Horst, A. J., Oates, S. R., Schady, P., Smith, R. J., Cummings, J., Starling, R. L. C., Piotrowski, L. W., Zhang, B., Evans, P. A., Holland, S. T., Malek, K., Page, M. T., Vetere, L., Margutti, R., Guidorzi, C., Kamble, A. P., Curran, P. A., Beardmore, A., Kouveliotou, C., Mankiewicz, L., Melandri, A., O'Brien, P. T., Page, K. L., Piran, T., Tanvir, N. R., Wrochna, G., Aptekar, R. L., Barthelmy, S., Bartolini, C., Beskin, G. M., Bondar, S., Bremer, M., Campana, S., Castro-Tirado, A., Cucchiara, A., Cwiok, M., D'Avanzo, P., D'Elia, V., Della Valle, M., de Ugarte Postigo, A., Dominik, W., Falcone, A., Fiore, F., Fox, D. B., Frederiks, D. D., Fruchter, A. S., Fugazza, D., Garrett, M. A., Gehrels, N., Golenetskii, S., Gomboc, A., Gorosabel, J., Greco, G., Guarnieri, A., Immler, S., Jelinek, M., Kasprowicz, G., La Parola, V., Levan, A. J., Mangano, V., Mazets, E. P., Molinari, E., Moretti, A., Nawrocki, K., Oleynik, P. P., Osborne, J. P., Pagani, C., Pandey, S. B., Paragi, Z.,

Perri, M., Piccioni, A., Ramirez-Ruiz, E., Roming, P. W. A., Steele, I. A., Strom, R. G., Testa, V., Tosti, G., Ulanov, M. V., Wiersema, K., Wijers, R. A. M. J., Winters, J. M., Zarnecki, A. F., Zerbi, F., Mészáros, P., Chincarini, G., and Burrows, D. N.: 2008, *Nature* **455**, 183

Racusin, J. L., Liang, E. W., Burrows, D. N., Falcone, A., Sakamoto, T., Zhang, B. B., Zhang, B., Evans, P., and Osborne, J.: 2009, *ApJ* **698**, 43

Ramirez-Ruiz, E., Dray, L. M., Madau, P., and Tout, C. A.: 2001, *MNRAS* **327**, 829

Rees, M. J. and Meszaros, P.: 1992, *MNRAS* **258**, 41P

Rees, M. J. and Meszaros, P.: 1994, *ApJL* **430**, L93

Rees, M. J. and Meszaros, P.: 1998, *ApJL* **496**, L1+

Rhoads, J. E.: 1997, *ApJL* **487**, L1+

Rhoads, J. E.: 1999, *ApJ* **525**, 737

Rhoads, J. E.: 2001, *ApJ* **557**, 943

Roming, P. W. A., Kennedy, T. E., Mason, K. O., Nousek, J. A., Ahr, L., Bingham, R. E., Broos, P. S., Carter, M. J., Hancock, B. K., Huckle, H. E., Hunsberger, S. D., Kawakami, H., Killough, R., Koch, T. S., McLelland, M. K., Smith, K., Smith, P. J., Soto, J. C., Boyd, P. T., Breeveld, A. A., Holland, S. T., Ivanushkina, M., Pryzby, M. S., Still, M. D., and Stock, J.: 2005, *Space Sci. Rev.* **120**, 95

Rossi, E., Lazzati, D., and Rees, M. J.: 2002, *MNRAS* **332**, 945

Rossi, E. M., Lazzati, D., Salmonson, J. D., and Ghisellini, G.: 2004, *MNRAS* **354**, 86

Rykoff, E. S., Smith, D. A., Price, P. A., Akerlof, C. W., Ashley, M. C. B., Bizyaev, D., Garradd, G. J., McKay, T. A., McNaught, R. H., Phillips, A., Quimby, R., Schaefer, B., Schmidt, B., Vestrand, W. T., Wheeler, J. C., and Wren, J.: 2004, *ApJ* **601**, 1013

Sari, R.: 1997, *ApJL* **489**, L37+

Sari, R. and Mészáros, P.: 2000, *ApJL* **535**, L33

Sari, R. and Piran, T.: 1995, *ApJL* **455**, L143+

Sari, R. and Piran, T.: 1999a, *ApJL* **517**, L109

Sari, R. and Piran, T.: 1999b, *ApJ* **520**, 641

Sari, R., Piran, T., and Halpern, J. P.: 1999, *ApJL* **519**, L17

Sari, R., Piran, T., and Narayan, R.: 1998, *ApJL* **497**, L17+

Sato, R., Kawai, N., Suzuki, M., Yatsu, Y., Kataoka, J., Takagi, R., Yanagisawa, K., and Yamaoka, H.: 2004, in E. Fenimore & M. Galassi (ed.), *Gamma-Ray Bursts: 30 Years of Discovery*, Vol. 727 of *American Institute of Physics Conference Series*, pp 307–311

Schady, P., Mason, K. O., Page, M. J., de Pasquale, M., Morris, D. C., Romano, P., Roming, P. W. A., Immler, S., and vanden Berk, D. E.: 2007, *MNRAS* **377**, 273

Schady, P., Page, M. J., Oates, S. R., Still, M., de Pasquale, M., Dwelly, T., Kuin, N. P. M., Holland, S. T., Marshall, F. E., and Roming, P. W. A.: 2010, *MNRAS* **401**, 2773

Schlegel, D. J., Finkbeiner, D. P., and Davis, M.: 1998, *ApJ* **500**, 525

Shao, L. and Dai, Z. G.: 2005, *ApJ* **633**, 1027

Shemi, A. and Piran, T.: 1990, *ApJL* **365**, L55

Sheth, K., Frail, D. A., White, S., Das, M., Bertoldi, F., Walter, F., Kulkarni, S. R., and Berger, E.: 2003, *ApJL* **595**, L33

Skrutskie, M. F., Cutri, R. M., Stiening, R., Weinberg, M. D., Schneider, S., Carpenter, J. M., Beichman, C., Capps, R., Chester, T., Elias, J., Huchra, J., Liebert, J., Lonsdale, C., Monet, D. G., Price, S., Seitzer, P., Jarrett, T., Kirkpatrick, J. D., Gizis, J. E., Howard, E., Evans, T., Fowler, J., Fullmer, L., Hurt, R., Light, R., Kopan, E. L., Marsh, K. A., McCallon, H. L., Tam, R., Van Dyk, S., and Wheelock, S.: 2006, *AJ* **131**, 1163

Smith, J. A., Tucker, D. L., Kent, S., Richmond, M. W., Fukugita, M., Ichikawa, T., Ichikawa, S.-i., Jorgensen, A. M., Uomoto, A., Gunn, J. E., Hamabe, M., Watanabe, M., Tolea, A., Henden, A., Annis, J., Pier, J. R., McKay, T. A., Brinkmann, J., Chen, B., Holtzman, J., Shimasaku, K., and York, D. G.: 2002, *AJ* **123**, 2121

Stamatikos, M., Barthelmy, S. D., Baumgartner, W. H., Cummings, J. R., Fenimore, E. E., Gehrels, N., Krimm, H. A., Markwardt, C. B., Palmer, D. M., Sakamoto, T., Troja, E., Tueller, J., and Ukwatta, T. N.: 2009, *GRB Coordinates Network* **10197**, 1

Stamatikos, M., Beardmore, A. P., Gehrels, N., Hunsberger, S. D., Markwardt, C. B., Osborne, J. P., Page, K. L., Palmer, D. M., Sakamoto, T., Starling, R. L. C., and Troja, E.: 2008, *GRB Coordinates Network* **7598**, 1

Stanek, K. Z., Matheson, T., Garnavich, P. M., Martini, P., Berlind, P., Caldwell, N., Challis, P., Brown, W. R., Schild, R., Krisciunas, K., Calkins, M. L., Lee, J. C., Hathi, N., Jansen, R. A., Windhorst, R., Echevarria, L., Eisenstein, D. J., Pindor, B., Olszewski, E. W., Harding, P., Holland, S. T., and Bersier, D.: 2003, *ApJL* **591**, L17

Starling, R. L. C., Wijers, R. A. M. J., Wiersema, K., Rol, E., Curran, P. A., Kouveli-otou, C., van der Horst, A. J., and Heemskerk, M. H. M.: 2007, *ApJ* **661**, 787

Thoene, C. C., Goldoni, P., Covino, S., Antonelli, L. A., Malesani, D., Fynbo, J. P. U., Levan, A. J., Jakobsson, P., Flores, H., Milvang-Jensen, B., Hjorth, J., Watson, D., Wiersema, K., Tanvir, N. R., and de Ugarte Postigo, A.: 2009, *GRB Coordinates Network* **10233**, 1

Thöne, C. C., Kann, D. A., Jóhannesson, G., Selj, J. H., Jaunsen, A. O., Fynbo, J. P. U., Akerlof, C. W., Baliyan, K. S., Bartolini, C., Bikmaev, I. F., Bloom, J. S., Burenin, R. A., Cobb, B. E., Covino, S., Curran, P. A., Dahle, H., Ferrero, A., Foley, S., French, J., Fruchter, A. S., Ganesh, S., Graham, J. F., Greco, G., Guarnieri, A., Hanlon, L., Hjorth, J., Ibrahimov, M., Israel, G. L., Jakobsson, P., Jelínek, M., Jensen, B. L., Jørgensen, U. G., Khamitov, I. M., Koch, T. S., Levan, A. J., Malesani, D., Masetti, N., Meehan, S., Melady, G., Nanni, D., Näränen, J., Pakstiene, E., Pavlinsky, M. N., Perley, D. A., Piccioni, A., Pizzichini, G., Pozanenko, A., Roming, P. W. A., Rujopakarn, W., Rumyantsev, V., Rykoff, E. S., Sharapov, D., Starr, D., Sunyaev, R. A., Swan, H., Tanvir, N. R., Terra, F., de Ugarte Postigo, A., Vreeswijk, P. M., Wilson, A. C., Yost, S. A., and Yuan, F.: 2010, *A&A* **523**, A70+

Tody, D.: 1993, in R. J. Hanisch, R. J. V. Brissenden, & J. Barnes (ed.), *Astronomical Data Analysis Software and Systems II*, Vol. 52 of *Astronomical Society of the Pacific Conference Series*, pp 173–+

Torii, K., Fukazawa, Y., and Tsunemi, H.: 2005, *A&A* **437**, L23

Troja, E., Barthelmy, S. D., Baumgartner, W. H., Burrows, D. N., Evans, P. A., Gehrels, N., Guidorzi, C., Holland, S. T., Kennea, J. A., Mao, J., Marshall, F. E., Osborne, J. P., Page, K. L., Palmer, D. M., Racusin, J. L., Rowlinson, A., and Stamatikos, M.: 2009a, *GRB Coordinates Network* **10191**, 1

Troja, E., Beardmore, A. P., Hoversten, E. A., Krimm, H. A., Markwardt, C. B., O'Brien, P. T., Page, K. L., Palmer, D. M., Romano, P., Rowlinson, A., and Siegel, M. H.: 2009b, *GRB Coordinates Network* **9913**, 1

Troja, E. and Stamatikos, M.: 2008, *GRB Coordinates Network* **7608**, 1

Uemura, M., Kato, T., Ishioka, R., Yamaoka, H., Monard, B., Nogami, D., Maehara, H., Sugie, A., and Takahashi, S.: 2003, *Nature* **423**, 843

Updike, A., Rossi, A., Rau, A., Greiner, J., Afonso, P., and Yoldas, A.: 2009, *GRB Coordinates Network* **10195**, 1

van Eerten, H. J., Meliani, Z., Wijers, R. A. M. J., and Keppens, R.: 2009, *MNRAS* **398**, L63

van Marle, A. J., Langer, N., Achterberg, A., and García-Segura, G.: 2006, *A&A* **460**, 105

van Paradijs, J., Groot, P. J., Galama, T., Kouveliotou, C., Strom, R. G., Telting, J., Rutten, R. G. M., Fishman, G. J., Meegan, C. A., Pettini, M., Tanvir, N., Bloom, J., Pedersen, H., Nørdgaard-Nielsen, H. U., Linden-Vørnle, M., Melnick, J., van der Steene, G., Bremer, M., Naber, R., Heise, J., in't Zand, J., Costa, E., Feroci, M., Piro, L., Frontera, F., Zavattini, G., Nicastro, L., Palazzi, E., Bennett, K., Hanlon, L., and Parmar, A.: 1997, *Nature* **386**, 686

van Paradijs, J., Kouveliotou, C., and Wijers, R. A. M. J.: 2000, *ARA&A* **38**, 379

Vergani, S. D., Flores, H., Covino, S., Fugazza, D., Gorosabel, J., Levan, A. J., Puech, M., Salvaterra, R., Tello, J. C., de Ugarte Postigo, A., D'Avanzo, P., D'Elia, V., Fernández, M., Fynbo, J. P. U., Ghirlanda, G., Jelínek, M., Lundgren, A., Malesani, D., Palazzi, E., Piranomonte, S., Rodrigues, M., Sánchez-Ramírez, R., Terrón, V., Thöne, C. C., Antonelli, L. A., Campana, S., Castro-Tirado, A. J., Goldoni, P., Hammer, F., Hjorth, J., Jakobsson, P., Kaper, L., Melandri, A., Milvang-Jensen, B., Sollerman, J., Tagliaferri, G., Tanvir, N. R., Wiersema, K., and Wijers, R. A. M. J.: 2011, *ArXiv e-prints*

Vlahakis, N., Peng, F., and Königl, A.: 2003, *ApJL* **594**, L23

Vreeswijk, P. M., Ledoux, C., Smette, A., Ellison, S. L., Jaunsen, A. O., Andersen, M. I., Fruchter, A. S., Fynbo, J. P. U., Hjorth, J., Kaufer, A., Møller, P., Petitjean, P., Savaglio, S., and Wijers, R. A. M. J.: 2007, *A&A* **468**, 83

Vreeswijk, P. M., Thoene, C. C., Malesani, D., Fynbo, J. P. U., Hjorth, J., Jakobsson, P., Tanvir, N. R., and Levan, A. J.: 2008, *GRB Coordinates Network* **7601**, 1

Wang, X. and Loeb, A.: 2000, *ApJ* **535**, 788

Waxman, E.: 1997, *ApJL* **489**, L33+

Wijers, R. A. M. J. and Galama, T. J.: 1999, *ApJ* **523**, 177

Wisotzki, L., Selman, F., and Gilliote, A.: 2001, *The Messenger* **104**, 8

Woods, E. and Loeb, A.: 1999, *ApJ* **523**, 187

Woosley, S. E.: 1993, *ApJ* **405**, 273

Wu, X. F., Dai, Z. G., Huang, Y. F., and Lu, T.: 2003, *MNRAS* **342**, 1131

Wu, X. F., Dai, Z. G., Huang, Y. F., and Lu, T.: 2005, *MNRAS* **357**, 1197

Yoldaş, A. K., Krühler, T., Greiner, J., Yoldaş, A., Clemens, C., Szokoly, G., Primak, N., and Klose, S.: 2008, in M. Galassi, D. Palmer, & E. Fenimore (ed.), *American Institute of Physics Conference Series*, Vol. 1000 of *American Institute of Physics Conference Series*, pp 227–231

Yost, S. A., Alatalo, K., Rykoff, E. S., Aharonian, F., Akerlof, C. W., Ashley, M. C. B., Blake, C. H., Bloom, J. S., Boettcher, M., Falco, E. E., Göğüş, E., Güver, T., Halpern, J. P., Horns, D., Joshi, M., Kızıloğlu, Ü., McKay, T. A., Mirabal, N., Özel, M., Phillips, A., Quimby, R. M., Rujopakarn, W., Schaefer, B. E., Shields, J. C., Skrutskie, M., Smith, D. A., Starr, D. L., Swan, H. F., Szentgyorgyi, A., Vestrand, W. T., Wheeler, J. C., and Wren, J.: 2006, *ApJ* **636**, 959

Yost, S. A., Harrison, F. A., Sari, R., and Frail, D. A.: 2003, *ApJ* **597**, 459

Zeh, A., Klose, S., and Kann, D. A.: 2006, *ApJ* **637**, 889

Zerbi, R. M., Chincarini, G., Ghisellini, G., Rondonó, M., Tosti, G., Antonelli, L. A., Conconi, P., Covino, S., Cutispoto, G., Molinari, E., Nicastro, L., Palazzi, E., Akerlof, C., Burderi, L., Campana, S., Crimi, G., Danzinger, J., di Paola, A., Fernandez-Soto, A., Fiore, F., Frontera, F., Fugazza, D., Gentile, G., Goldoni, P., Israel, G., Jordan, B., Lorenzetti, D., McBreen, B., Martinetti, E., Mazzoleni, R., Masetti, N., Messina, S., Meurs, E., Monfardini, A., Nucciarelli, G., Orlandini, M., Paul, J., Pian, E., Saracco, P., Sardone, S., Stella, L., Tagliaferri, L., Tavani, M., Testa, V., and Vitali, F.: 2001, *Astronomische Nachrichten* **322**, 275

Zhang, B., Fan, Y. Z., Dyks, J., Kobayashi, S., Mészáros, P., Burrows, D. N., Nousek, J. A., and Gehrels, N.: 2006, *ApJ* **642**, 354

Zhang, B. and Kobayashi, S.: 2005, *ApJ* **628**, 315

Zhang, B., Kobayashi, S., and Mészáros, P.: 2003, *ApJ* **595**, 950

Zhang, B. and Mészáros, P.: 2001, *ApJL* **552**, L35

Zhang, B. and Mészáros, P.: 2002a, *ApJ* **571**, 876

Zhang, B. and Mészáros, P.: 2002b, *ApJ* **566**, 712

Zhang, B. and Mészáros, P.: 2004, *International Journal of Modern Physics A* **19**, 2385

Zhang, W., Woosley, S. E., and Heger, A.: 2004, *ApJ* **608**, 365

Zheng, W. and Deng, J.: 2010, *Science in China G: Physics and Astronomy* **53**, 265

Acknowledgments

Appendix

Table 6.1: $g'r'i'z'$ photometric data of GRB 080413B

$T_{\mathrm{mid}} - T_0$ [ks]	Exposure [s]	Brightness[a] $\mathrm{mag_{AB}}$			
		g'	r'	i'	z'
0.0765	30		16.19 ± 0.19		
0.1158	30		16.46 ± 0.16		
0.1549	30		16.65 ± 0.20		
0.2334	110		16.93 ± 0.20		
0.3421	35	17.44 ± 0.05	17.28 ± 0.03	17.24 ± 0.04	17.10 ± 0.05
0.4441	35	17.67 ± 0.04	17.53 ± 0.03	17.49 ± 0.04	17.37 ± 0.04
0.5443	35	17.86 ± 0.04	17.71 ± 0.03	17.73 ± 0.03	17.56 ± 0.04
0.6463	35	18.00 ± 0.04	17.86 ± 0.03	17.84 ± 0.04	17.67 ± 0.04
0.7646	35	18.11 ± 0.04	18.00 ± 0.04	18.01 ± 0.04	17.83 ± 0.05
0.8657	35	18.24 ± 0.04	18.10 ± 0.03	18.07 ± 0.04	17.89 ± 0.04
0.9677	35	18.29 ± 0.03	18.17 ± 0.03	18.15 ± 0.04	17.97 ± 0.04
1.0679	35	18.37 ± 0.04	18.21 ± 0.03	18.24 ± 0.04	18.05 ± 0.04
1.2390	35	18.49 ± 0.04	18.33 ± 0.04	18.32 ± 0.04	18.15 ± 0.05
1.3401	35	18.54 ± 0.04	18.39 ± 0.03	18.33 ± 0.04	18.21 ± 0.04
1.4394	35	18.57 ± 0.04	18.43 ± 0.03	18.45 ± 0.04	18.22 ± 0.04
1.5396	35	18.63 ± 0.04	18.45 ± 0.03	18.46 ± 0.04	18.29 ± 0.04
1.6813	35	18.63 ± 0.04	18.49 ± 0.04	18.49 ± 0.05	18.36 ± 0.05
1.7824	35	18.70 ± 0.03	18.54 ± 0.03	18.50 ± 0.04	18.40 ± 0.04
1.8835	35	18.72 ± 0.04	18.56 ± 0.03	18.56 ± 0.04	18.41 ± 0.04
1.9863	35	18.74 ± 0.03	18.58 ± 0.03	18.59 ± 0.04	18.45 ± 0.04
2.1021	35	18.77 ± 0.04	18.64 ± 0.04	18.62 ± 0.04	18.41 ± 0.05
2.2041	35	18.81 ± 0.04	18.64 ± 0.03	18.64 ± 0.04	18.47 ± 0.04
2.3034	35	18.83 ± 0.04	18.64 ± 0.04	18.64 ± 0.04	18.48 ± 0.04
2.4062	35	18.85 ± 0.04	18.72 ± 0.04	18.71 ± 0.04	18.58 ± 0.04
2.5237	35	18.88 ± 0.04	18.73 ± 0.04	18.65 ± 0.04	18.56 ± 0.06
2.6240	35	18.91 ± 0.04	18.76 ± 0.03	18.72 ± 0.04	18.57 ± 0.04
2.7242	35	18.91 ± 0.04	18.77 ± 0.03	18.77 ± 0.04	18.52 ± 0.04
2.8261	35	18.96 ± 0.04	18.81 ± 0.04	18.78 ± 0.04	18.61 ± 0.04
2.9428	35	19.00 ± 0.04	18.82 ± 0.04	18.85 ± 0.05	18.64 ± 0.05
3.0439	35	19.01 ± 0.03	18.84 ± 0.03	18.88 ± 0.04	18.69 ± 0.04
3.1441	35	19.03 ± 0.03	18.85 ± 0.03	18.83 ± 0.04	18.72 ± 0.05
3.2443	35	19.03 ± 0.04	18.88 ± 0.04	18.83 ± 0.04	18.69 ± 0.05
3.3566	35	19.06 ± 0.04	18.90 ± 0.04	18.87 ± 0.05	18.73 ± 0.06
3.4577	35	19.07 ± 0.04	18.92 ± 0.03	18.94 ± 0.04	18.72 ± 0.05
3.5580	35	19.10 ± 0.04	18.94 ± 0.03	18.91 ± 0.04	18.77 ± 0.05
3.6599	35	19.14 ± 0.04	18.94 ± 0.04	18.97 ± 0.04	18.83 ± 0.05

Table 6.1: continued.

$T_{\mathrm{mid}} - T_0$ [ks]	Exposure [s]	Brightness[a] $\mathrm{mag_{AB}}$			
		g'	r'	i'	z'
3.7731	35	19.11 ± 0.05	18.98 ± 0.04	18.96 ± 0.05	18.81 ± 0.06
3.8733	35	19.16 ± 0.05	18.95 ± 0.04	19.05 ± 0.05	18.83 ± 0.05
3.9735	35	19.13 ± 0.04	18.98 ± 0.04	19.03 ± 0.04	18.77 ± 0.04
4.0764	35	19.19 ± 0.04	19.06 ± 0.04	19.03 ± 0.05	18.81 ± 0.05
4.1913	35	19.20 ± 0.05	19.04 ± 0.04	18.98 ± 0.05	18.87 ± 0.06
4.2924	35	19.30 ± 0.04	19.06 ± 0.04	19.08 ± 0.04	18.92 ± 0.05
4.3943	35	19.24 ± 0.05	19.11 ± 0.04	19.00 ± 0.04	18.90 ± 0.05
4.4963	35	19.24 ± 0.04	19.10 ± 0.04	19.10 ± 0.05	18.85 ± 0.04
4.6172	35	19.29 ± 0.09	19.13 ± 0.05	19.03 ± 0.06	18.86 ± 0.08
4.7148	35	19.20 ± 0.06	19.15 ± 0.04	19.09 ± 0.05	18.86 ± 0.05
4.8159	35	19.24 ± 0.06	19.18 ± 0.04	19.13 ± 0.06	18.92 ± 0.07
4.9179	35	19.37 ± 0.07	19.10 ± 0.05	19.15 ± 0.08	18.95 ± 0.06
90.3010	2733	20.19 ± 0.04	19.91 ± 0.04	19.81 ± 0.05	19.65 ± 0.04
176.4193	3805	20.92 ± 0.05	20.55 ± 0.04	20.38 ± 0.05	20.27 ± 0.05
262.4098	3556	21.36 ± 0.04	21.00 ± 0.04	20.79 ± 0.04	20.57 ± 0.05
434.6533	4046	22.26 ± 0.05	22.01 ± 0.04	21.82 ± 0.06	21.51 ± 0.06
522.1878	3036	22.83 ± 0.12	22.46 ± 0.07	22.17 ± 0.11	22.22 ± 0.11
780.5056	3520	23.88 ± 0.30	23.50 ± 0.15	23.20 ± 0.18	23.49 ± 0.25
1901.2933	2989	24.69 ± 0.17	24.45 ± 0.23	> 23.54	> 23.34
2418.4846	7770	25.12 ± 0.19	24.90 ± 0.25	> 23.78	> 23.36
5185.0714	6995	25.61 ± 0.24	25.13 ± 0.22	> 24.22	> 23.87

[a] Not corrected for Galactic foreground reddening.

Table 6.2 JHK_s photometric data of GRB 080413B

$T_{\mathrm{mid}} - T_0$ [ks]	Exposure [s]	Brightness[a] $\mathrm{mag}_{\mathrm{AB}}^{(b)}$		
		J	H	K_s
0.0956	10		16.19 ± 0.12	
0.1746	10		16.97 ± 0.21	
0.4251	168	17.30 ± 0.07	17.20 ± 0.07	16.92 ± 0.15
0.6275	168	17.71 ± 0.06	17.65 ± 0.08	17.19 ± 0.20
0.9392	385	18.03 ± 0.06	17.89 ± 0.07	
1.4126	384	18.22 ± 0.07	18.14 ± 0.07	18.01 ± 0.12
2.0667	808	18.47 ± 0.07	18.48 ± 0.07	18.23 ± 0.11
3.3229	1637 (1216 for H)	18.69 ± 0.06	18.76 ± 0.07	18.38 ± 0.10
4.9974	2065 (1650 for J)	18.93 ± 0.06	18.91 ± 0.06	18.63 ± 0.08
90.3234	2780	19.42 ± 0.06	19.14 ± 0.05	19.00 ± 0.05
176.4426	3854	19.97 ± 0.05	19.81 ± 0.05	19.39 ± 0.05
262.4340	3605	20.23 ± 0.05	20.00 ± 0.05	19.91 ± 0.08
434.6775	4096	21.47 ± 0.08	21.48 ± 0.08	> 20.28
522.2111	3084	22.03 ± 0.09	> 21.60	> 20.56
780.5298	3567	> 22.16	> 21.48	> 20.55
1901.3193	3040	> 21.96	> 21.35	> 20.57
2418.5088	7822	> 22.36	> 21.63	> 20.90
5185.0938	7041	> 22.57	> 21.92	> 20.97

[a] Not corrected for Galactic foreground reddening. Converted to AB magnitudes for consistency with Table 6.1.

[a] For the SED fitting, the additional error of the absolute calibration of 0.07 (J and H) and 0.09 (K_s) mag was added.

Table 6.3: $g'r'i'z'$ photometric data of GRB 091127

$T_{\mathrm{mid}} - T_0$ [ks]	Exposure [s]	Brightness[a] mag$_{\mathrm{AB}}$			
		g'	r'	i'	z'
3.3031	35	16.57 ± 0.01	16.53 ± 0.01	16.48 ± 0.01	16.41 ± 0.01
3.4039	35	16.62 ± 0.01	16.56 ± 0.01	16.51 ± 0.01	16.44 ± 0.01
3.5195	35	16.63 ± 0.01	16.56 ± 0.01	16.51 ± 0.01	16.45 ± 0.01
3.6192	35	16.65 ± 0.01	16.58 ± 0.01	16.52 ± 0.01	16.47 ± 0.01
3.7202	35	16.67 ± 0.01	16.59 ± 0.01	16.53 ± 0.01	16.47 ± 0.01
3.8222	35	16.67 ± 0.01	16.61 ± 0.01	16.55 ± 0.01	16.49 ± 0.01
3.9920	115	16.69 ± 0.01	16.62 ± 0.01	16.55 ± 0.01	16.51 ± 0.01
4.1762	115	16.72 ± 0.01	16.64 ± 0.01	16.58 ± 0.01	16.53 ± 0.01
4.3638	115	16.74 ± 0.01	16.66 ± 0.01	16.59 ± 0.01	16.54 ± 0.01
4.5513	115	16.76 ± 0.01	16.69 ± 0.01	16.61 ± 0.01	16.55 ± 0.01
4.7693	115	16.79 ± 0.01	16.71 ± 0.01	16.65 ± 0.01	16.60 ± 0.01
4.9561	115	16.81 ± 0.01	16.72 ± 0.01	16.66 ± 0.01	16.60 ± 0.01
5.1544	115	16.82 ± 0.01	16.74 ± 0.01	16.69 ± 0.01	16.61 ± 0.01
5.3507	115	16.84 ± 0.01	16.76 ± 0.01	16.69 ± 0.01	16.62 ± 0.01
5.5330	35	16.87 ± 0.01	16.77 ± 0.01	16.72 ± 0.01	16.66 ± 0.01
5.6328	35	16.86 ± 0.01	16.79 ± 0.01	16.71 ± 0.01	16.66 ± 0.01
5.7340	35	16.89 ± 0.01	16.79 ± 0.01	16.73 ± 0.01	16.66 ± 0.01
5.8360	35	16.89 ± 0.01	16.81 ± 0.01	16.76 ± 0.01	16.67 ± 0.01
5.9714	35	16.91 ± 0.01	16.81 ± 0.01	16.74 ± 0.01	16.67 ± 0.01
6.0722	35	16.91 ± 0.01	16.83 ± 0.01	16.75 ± 0.01	16.71 ± 0.01
6.1740	35	16.91 ± 0.01	16.83 ± 0.01	16.75 ± 0.01	16.70 ± 0.01
6.2755	35	16.93 ± 0.01	16.85 ± 0.01	16.77 ± 0.01	16.70 ± 0.01
6.4035	35	16.94 ± 0.01	16.86 ± 0.01	16.80 ± 0.01	16.72 ± 0.01
6.5029	35	16.95 ± 0.01	16.86 ± 0.01	16.79 ± 0.01	16.72 ± 0.01
6.6042	35	16.95 ± 0.01	16.87 ± 0.01	16.79 ± 0.01	16.74 ± 0.01
6.7059	35	16.98 ± 0.01	16.88 ± 0.01	16.81 ± 0.01	16.74 ± 0.01
6.8294	35	16.97 ± 0.01	16.89 ± 0.01	16.82 ± 0.01	16.74 ± 0.01
6.9322	35	16.99 ± 0.01	16.90 ± 0.01	16.82 ± 0.01	16.75 ± 0.01
7.0341	35	17.00 ± 0.01	16.92 ± 0.01	16.83 ± 0.01	16.77 ± 0.01
7.1359	35	17.01 ± 0.01	16.92 ± 0.01	16.84 ± 0.01	16.77 ± 0.01
7.2592	35	17.02 ± 0.01	16.93 ± 0.01	16.84 ± 0.01	16.78 ± 0.01
7.3600	35	17.02 ± 0.01	16.93 ± 0.01	16.85 ± 0.01	16.78 ± 0.01
7.4623	35	17.03 ± 0.01	16.94 ± 0.01	16.87 ± 0.01	16.79 ± 0.01
7.5638	35	17.04 ± 0.01	16.95 ± 0.01	16.86 ± 0.01	16.80 ± 0.01
7.6804	35	17.05 ± 0.01	16.96 ± 0.01	16.88 ± 0.01	16.79 ± 0.01
7.7819	35	17.06 ± 0.01	16.96 ± 0.01	16.88 ± 0.01	16.82 ± 0.01
7.8837	35	17.07 ± 0.01	16.97 ± 0.01	16.91 ± 0.01	16.84 ± 0.01
7.9858	35	17.07 ± 0.01	16.99 ± 0.01	16.89 ± 0.01	16.83 ± 0.01
8.1035	35	17.07 ± 0.01	16.99 ± 0.01	16.92 ± 0.01	16.85 ± 0.01

Table 6.3: continued.

$T_{\mathrm{mid}} - T_0$ [ks]	Exposure [s]	Brightness[a] $\mathrm{mag_{AB}}$			
		g'	r'	i'	z'
8.2033	35	17.09 ± 0.01	17.00 ± 0.01	16.91 ± 0.01	16.85 ± 0.01
8.3060	35	17.10 ± 0.01	17.01 ± 0.01	16.92 ± 0.01	16.85 ± 0.01
8.4083	35	17.10 ± 0.01	17.01 ± 0.01	16.93 ± 0.01	16.87 ± 0.01
8.5548	35	17.13 ± 0.01	17.02 ± 0.01	16.93 ± 0.01	16.87 ± 0.01
8.6551	35	17.12 ± 0.01	17.03 ± 0.01	16.93 ± 0.01	16.87 ± 0.01
8.7563	35	17.14 ± 0.01	17.03 ± 0.01	16.96 ± 0.01	16.87 ± 0.01
8.8578	35	17.14 ± 0.01	17.03 ± 0.01	16.96 ± 0.01	16.89 ± 0.01
8.9765	35	17.15 ± 0.01	17.04 ± 0.01	16.95 ± 0.01	16.89 ± 0.01
9.0752	35	17.16 ± 0.01	17.04 ± 0.01	16.96 ± 0.01	16.91 ± 0.01
9.1764	35	17.17 ± 0.01	17.06 ± 0.01	16.97 ± 0.01	16.91 ± 0.01
9.2780	35	17.17 ± 0.01	17.07 ± 0.01	16.97 ± 0.01	16.91 ± 0.01
9.3991	35	17.17 ± 0.01	17.07 ± 0.01	16.99 ± 0.01	16.92 ± 0.01
9.4984	35	17.18 ± 0.01	17.09 ± 0.01	17.00 ± 0.01	16.92 ± 0.01
9.6003	35	17.19 ± 0.01	17.09 ± 0.01	17.01 ± 0.01	16.95 ± 0.01
9.7024	35	17.19 ± 0.01	17.09 ± 0.01	17.01 ± 0.01	16.95 ± 0.01
9.8230	35	17.21 ± 0.01	17.10 ± 0.01	17.02 ± 0.01	16.96 ± 0.01
9.9224	35	17.21 ± 0.01	17.11 ± 0.01	17.02 ± 0.01	16.96 ± 0.01
10.0238	35	17.22 ± 0.01	17.12 ± 0.01	17.03 ± 0.01	16.96 ± 0.01
10.1261	35	17.22 ± 0.01	17.12 ± 0.01	17.03 ± 0.01	16.97 ± 0.01
10.2507	35	17.24 ± 0.01	17.14 ± 0.01	17.03 ± 0.01	16.97 ± 0.01
10.3520	35	17.24 ± 0.01	17.14 ± 0.01	17.05 ± 0.01	16.97 ± 0.01
10.4540	35	17.25 ± 0.01	17.15 ± 0.01	17.06 ± 0.01	16.99 ± 0.01
10.5581	35	17.25 ± 0.01	17.15 ± 0.01	17.08 ± 0.01	16.99 ± 0.01
10.6782	35	17.25 ± 0.01	17.14 ± 0.01	17.06 ± 0.01	17.01 ± 0.01
10.7768	35	17.26 ± 0.01	17.16 ± 0.01	17.07 ± 0.01	17.00 ± 0.01
10.8783	35	17.26 ± 0.01	17.17 ± 0.01	17.06 ± 0.01	17.02 ± 0.01
10.9796	35	17.29 ± 0.01	17.17 ± 0.01	17.10 ± 0.01	17.00 ± 0.01
11.1013	35	17.28 ± 0.01	17.16 ± 0.01	17.08 ± 0.01	17.03 ± 0.01
11.2013	35	17.29 ± 0.01	17.18 ± 0.01	17.10 ± 0.01	17.02 ± 0.01
11.3023	35	17.30 ± 0.01	17.19 ± 0.01	17.11 ± 0.01	17.04 ± 0.01
11.4035	35	17.29 ± 0.01	17.19 ± 0.01	17.12 ± 0.01	17.03 ± 0.01
11.5335	35	17.31 ± 0.01	17.21 ± 0.01	17.11 ± 0.01	17.04 ± 0.01
11.6330	35	17.32 ± 0.01	17.21 ± 0.01	17.11 ± 0.01	17.06 ± 0.01
11.7365	35	17.33 ± 0.01	17.22 ± 0.01	17.13 ± 0.01	17.06 ± 0.01
11.8405	35	17.32 ± 0.01	17.21 ± 0.01	17.14 ± 0.01	17.06 ± 0.01
11.9610	35	17.33 ± 0.01	17.22 ± 0.01	17.13 ± 0.01	17.07 ± 0.01
12.0624	35	17.34 ± 0.01	17.23 ± 0.01	17.13 ± 0.01	17.07 ± 0.01
12.1642	35	17.35 ± 0.01	17.24 ± 0.01	17.14 ± 0.01	17.08 ± 0.01
12.2655	35	17.37 ± 0.01	17.24 ± 0.01	17.15 ± 0.01	17.08 ± 0.01

113

Table 6.3: continued.

$T_{\mathrm{mid}} - T_0$ [ks]	Exposure [s]	Brightness[a] mag$_{\mathrm{AB}}$			
		g'	r'	i'	z'
12.3911	35	17.35 ± 0.01	17.25 ± 0.01	17.15 ± 0.01	17.08 ± 0.01
12.4924	35	17.37 ± 0.01	17.25 ± 0.01	17.16 ± 0.01	17.09 ± 0.01
12.5943	35	17.38 ± 0.01	17.27 ± 0.01	17.16 ± 0.01	17.11 ± 0.01
12.6953	35	17.37 ± 0.01	17.26 ± 0.01	17.16 ± 0.01	17.09 ± 0.01
12.8208	35	17.38 ± 0.01	17.28 ± 0.01	17.17 ± 0.01	17.11 ± 0.01
12.9194	35	17.39 ± 0.01	17.28 ± 0.01	17.17 ± 0.01	17.13 ± 0.01
13.0215	35	17.39 ± 0.01	17.29 ± 0.01	17.20 ± 0.01	17.11 ± 0.01
13.1243	35	17.40 ± 0.01	17.29 ± 0.01	17.19 ± 0.01	17.12 ± 0.01
13.2482	35	17.39 ± 0.01	17.29 ± 0.01	17.19 ± 0.01	17.12 ± 0.01
13.3501	35	17.42 ± 0.01	17.31 ± 0.01	17.21 ± 0.01	17.14 ± 0.01
13.4522	35	17.42 ± 0.01	17.30 ± 0.01	17.21 ± 0.01	17.15 ± 0.01
13.5537	35	17.41 ± 0.01	17.31 ± 0.01	17.22 ± 0.01	17.15 ± 0.01
13.6766	35	17.43 ± 0.01	17.31 ± 0.01	17.22 ± 0.01	17.14 ± 0.01
13.7783	35	17.43 ± 0.01	17.32 ± 0.01	17.22 ± 0.01	17.16 ± 0.01
13.8797	35	17.44 ± 0.01	17.32 ± 0.01	17.24 ± 0.01	17.16 ± 0.01
13.9818	35	17.44 ± 0.01	17.34 ± 0.01	17.26 ± 0.01	17.15 ± 0.01
14.1025	35	17.46 ± 0.01	17.34 ± 0.01	17.25 ± 0.01	17.17 ± 0.01
14.2035	35	17.46 ± 0.01	17.34 ± 0.01	17.26 ± 0.01	17.18 ± 0.01
14.3064	35	17.47 ± 0.01	17.34 ± 0.01	17.25 ± 0.01	17.16 ± 0.01
14.4076	35	17.47 ± 0.01	17.36 ± 0.01	17.25 ± 0.01	17.19 ± 0.01
14.5296	35	17.48 ± 0.01	17.36 ± 0.01	17.26 ± 0.01	17.19 ± 0.01
14.6315	35	17.47 ± 0.01	17.36 ± 0.01	17.27 ± 0.01	17.19 ± 0.01
14.7306	35	17.48 ± 0.01	17.37 ± 0.01	17.27 ± 0.01	17.21 ± 0.01
14.8318	35	17.48 ± 0.01	17.37 ± 0.01	17.28 ± 0.01	17.22 ± 0.01
14.9555	35	17.49 ± 0.01	17.38 ± 0.01	17.28 ± 0.01	17.21 ± 0.01
15.0579	35	17.50 ± 0.01	17.39 ± 0.01	17.31 ± 0.01	17.22 ± 0.01
15.1596	35	17.51 ± 0.01	17.40 ± 0.01	17.29 ± 0.01	17.22 ± 0.01
15.2643	35	17.50 ± 0.01	17.40 ± 0.01	17.30 ± 0.01	17.23 ± 0.01
15.3892	35	17.52 ± 0.01	17.40 ± 0.01	17.30 ± 0.01	17.23 ± 0.01
15.4886	35	17.54 ± 0.01	17.42 ± 0.01	17.32 ± 0.01	17.24 ± 0.01
15.5903	35	17.53 ± 0.01	17.43 ± 0.01	17.30 ± 0.01	17.23 ± 0.01
15.6915	35	17.52 ± 0.01	17.41 ± 0.01	17.30 ± 0.01	17.24 ± 0.01
15.8137	35	17.54 ± 0.01	17.42 ± 0.01	17.32 ± 0.01	17.25 ± 0.01
15.9162	35	17.54 ± 0.01	17.43 ± 0.01	17.34 ± 0.01	17.26 ± 0.01
16.0176	35	17.54 ± 0.01	17.42 ± 0.01	17.32 ± 0.01	17.24 ± 0.01
16.1197	35	17.54 ± 0.01	17.44 ± 0.01	17.33 ± 0.01	17.26 ± 0.01
16.2395	35	17.57 ± 0.01	17.44 ± 0.01	17.34 ± 0.01	17.27 ± 0.01
16.3388	35	17.57 ± 0.01	17.45 ± 0.01	17.32 ± 0.01	17.29 ± 0.01
16.4424	35	17.57 ± 0.01	17.46 ± 0.01	17.33 ± 0.01	17.31 ± 0.01

Table 6.3: continued.

$T_{\mathrm{mid}} - T_0$ [ks]	Exposure [s]	Brightness[a] $\mathrm{mag_{AB}}$			
		g'	r'	i'	z'
16.5444	35	17.58 ± 0.01	17.47 ± 0.01	17.35 ± 0.01	17.33 ± 0.01
16.9464	115	17.60 ± 0.01	17.48 ± 0.01	17.37 ± 0.01	17.31 ± 0.01
17.1273	115	17.62 ± 0.01	17.49 ± 0.01	17.40 ± 0.01	17.31 ± 0.01
17.3279	115	17.62 ± 0.01	17.50 ± 0.01	17.40 ± 0.01	17.32 ± 0.01
17.5383	115	17.62 ± 0.01	17.51 ± 0.01	17.41 ± 0.01	17.32 ± 0.01
17.7360	115	17.62 ± 0.01	17.53 ± 0.01	17.42 ± 0.01	17.34 ± 0.01
17.9339	115	17.63 ± 0.01	17.53 ± 0.01	17.42 ± 0.01	17.34 ± 0.01
18.1312	115	17.65 ± 0.01	17.54 ± 0.01	17.45 ± 0.01	17.36 ± 0.01
18.3158	115	17.65 ± 0.01	17.55 ± 0.01	17.43 ± 0.01	17.38 ± 0.01
18.5209	115	17.67 ± 0.01	17.56 ± 0.01	17.47 ± 0.01	17.38 ± 0.01
18.7128	115	17.69 ± 0.01	17.58 ± 0.01	17.44 ± 0.01	17.39 ± 0.01
18.9061	115	17.68 ± 0.01	17.57 ± 0.01	17.46 ± 0.01	17.39 ± 0.01
19.1020	115	17.69 ± 0.01	17.59 ± 0.01	17.47 ± 0.01	17.42 ± 0.01
19.3182	115	17.71 ± 0.01	17.59 ± 0.01	17.50 ± 0.01	17.40 ± 0.01
19.5012	115	17.70 ± 0.01	17.60 ± 0.01	17.51 ± 0.01	17.43 ± 0.01
19.6840	115	17.73 ± 0.01	17.60 ± 0.01	17.50 ± 0.01	17.42 ± 0.01
19.8676	115	17.74 ± 0.01	17.61 ± 0.01	17.51 ± 0.01	17.42 ± 0.01
20.0781	115	17.73 ± 0.01	17.62 ± 0.01	17.52 ± 0.01	17.47 ± 0.01
20.2726	115	17.75 ± 0.01	17.63 ± 0.01	17.51 ± 0.01	17.46 ± 0.01
20.4570	115	17.76 ± 0.01	17.64 ± 0.01	17.52 ± 0.01	17.46 ± 0.01
20.6577	115	17.77 ± 0.01	17.65 ± 0.01	17.53 ± 0.02	17.49 ± 0.01
20.8744	115	17.77 ± 0.01	17.66 ± 0.01	17.54 ± 0.02	17.48 ± 0.02
21.0717	115	17.76 ± 0.01	17.68 ± 0.01	17.55 ± 0.01	17.49 ± 0.01
21.2673	115	17.79 ± 0.01	17.67 ± 0.01	17.56 ± 0.01	17.48 ± 0.01
21.4580	115	17.81 ± 0.01	17.69 ± 0.01	17.58 ± 0.01	17.49 ± 0.01
92.4295	701	19.66 ± 0.02	19.48 ± 0.02	19.29 ± 0.02	19.22 ± 0.03
93.2890	679	19.70 ± 0.02	19.49 ± 0.01	19.32 ± 0.02	19.22 ± 0.03
108.8565	686	19.92 ± 0.02	19.72 ± 0.01	19.58 ± 0.02	19.47 ± 0.02
179.6620	1695	20.78 ± 0.02	20.53 ± 0.02	20.31 ± 0.02	20.30 ± 0.03
189.9125	1714	20.85 ± 0.03	20.60 ± 0.02	20.42 ± 0.02	20.35 ± 0.03
277.0450	1708	21.55 ± 0.05	21.22 ± 0.04	21.04 ± 0.04	21.01 ± 0.06
363.9306	1697	21.96 ± 0.09	21.67 ± 0.05	21.48 ± 0.06	21.39 ± 0.06
533.5294	1707	22.43 ± 0.08	22.07 ± 0.06	21.91 ± 0.06	21.94 ± 0.08
959.0369	1709	23.18 ± 0.05	22.26 ± 0.03	21.86 ± 0.06	22.36 ± 0.15
960.8429	1709	23.21 ± 0.05	22.27 ± 0.03	21.92 ± 0.05	22.29 ± 0.12
3985.5129	3922	23.81 ± 0.08	22.86 ± 0.05	22.36 ± 0.06	22.61 ± 0.09
4244.3423	1700	23.87 ± 0.11	23.10 ± 0.06	22.65 ± 0.08	22.68 ± 0.17
4673.6840	1896	23.90 ± 0.19	23.16 ± 0.12	22.76 ± 0.13	22.78 ± 0.19
29225.2102	4906	24.12 ± 0.08	23.28 ± 0.05	22.88 ± 0.07	23.38 ± 0.18

Table 6.4: JH photometric data of GRB 091127

$T_{\mathrm{mid}} - T_0$ [ks]	Exposure [s]	Brightness[a] $\mathrm{mag}_{\mathrm{AB}}^{[b]}$	
		J	H
3.6948	386	16.37 ± 0.02	16.30 ± 0.03
4.2991	730	16.45 ± 0.02	16.33 ± 0.03
5.0877	752	16.51 ± 0.02	16.43 ± 0.03
5.7092	386	16.52 ± 0.02	16.45 ± 0.03
6.1479	387	16.56 ± 0.02	16.48 ± 0.03
6.5792	387	16.60 ± 0.02	16.51 ± 0.03
7.0072	388	16.63 ± 0.02	16.53 ± 0.03
7.4362	389	16.65 ± 0.02	16.53 ± 0.03
7.8569	389	16.69 ± 0.02	16.59 ± 0.03
8.2799	389	16.73 ± 0.02	16.60 ± 0.03
8.7311	385	16.75 ± 0.02	16.64 ± 0.03
9.1512	385	16.77 ± 0.02	16.69 ± 0.03
9.5755	387	16.83 ± 0.02	16.72 ± 0.03
9.9990	388	16.81 ± 0.02	16.76 ± 0.03
10.4291	391	16.84 ± 0.02	16.75 ± 0.03
10.8530	386	16.90 ± 0.02	16.77 ± 0.03
11.2784	388	16.91 ± 0.02	16.77 ± 0.03
11.7115	392	16.90 ± 0.02	16.77 ± 0.03
12.1371	388	16.90 ± 0.02	16.80 ± 0.03
12.5670	388	16.94 ± 0.02	16.86 ± 0.03
12.9968	388	17.00 ± 0.02	16.88 ± 0.03
13.4258	389	16.98 ± 0.02	16.88 ± 0.03
13.8544	387	17.01 ± 0.02	16.88 ± 0.03
14.2805	388	17.04 ± 0.02	16.88 ± 0.03
14.7055	385	17.07 ± 0.02	16.93 ± 0.03
15.1351	393	17.05 ± 0.02	16.93 ± 0.03
15.5656	387	17.08 ± 0.02	16.98 ± 0.03
15.9917	388	17.10 ± 0.02	17.00 ± 0.03
16.4118	381	17.12 ± 0.02	17.05 ± 0.03
17.2991	820	17.16 ± 0.02	17.03 ± 0.03
18.0559	742	17.22 ± 0.02	17.11 ± 0.03
18.8383	750	17.26 ± 0.02	17.15 ± 0.03
19.6202	720	17.28 ± 0.02	17.21 ± 0.03
20.3949	748	17.29 ± 0.02	17.26 ± 0.03
21.1932	753	17.34 ± 0.02	17.24 ± 0.03
92.4549	754	19.04 ± 0.09	18.83 ± 0.10
93.3151	733	19.09 ± 0.09	18.90 ± 0.09

Table 6.4: continued.

$T_{\mathrm{mid}} - T_0$ [ks]	Exposure [s]	Brightness[a] $\mathrm{mag}_{\mathrm{AB}}$[b]	
		J	H
107.4009	1751	19.23 ± 0.06	19.01 ± 0.08
179.6887	1751	20.09 ± 0.09	19.88 ± 0.11
189.9391	1770	20.09 ± 0.08	19.92 ± 0.12
277.0709	1762	20.54 ± 0.32	20.54 ± 0.23
363.9571	1750	20.88 ± 0.18	21.01 ± 0.29
533.5557	1750	21.53 ± 0.32	> 21.28
959.0635	1750	> 21.63	> 21.18
3985.5371	3969	21.74 ± 0.28	> 21.37
4244.2658	1750	> 21.69	> 21.21
4673.7890	1750	> 21.37	> 20.95

[a] Corrected for Galactic foreground reddening. Converted to AB magnitudes for consistency with Table 6.3.

[a] For the SED fitting, the additional error of the absolute calibration of 0.05 mag was added.

Table 6.5: $g'r'i'z'$ photometric data of GRB 091029

$T_{\mathrm{mid}} - T_0$ [ks]	Exposure [s]	Brightness[a] $\mathrm{mag}_{\mathrm{AB}}$			
		g'	r'	i'	z'
0.3067	66	18.19 ± 0.04	17.84 ± 0.02	17.78 ± 0.03	17.59 ± 0.08
0.4103	66	18.00 ± 0.04	17.69 ± 0.02	17.60 ± 0.02	17.38 ± 0.04
0.5154	66	18.09 ± 0.03	17.76 ± 0.02	17.66 ± 0.03	17.49 ± 0.05
0.7290	66	18.22 ± 0.03	17.92 ± 0.02	17.87 ± 0.04	17.64 ± 0.05
0.8257	66	18.31 ± 0.03	17.98 ± 0.02	17.94 ± 0.03	17.76 ± 0.06
0.9237	66	18.39 ± 0.03	18.07 ± 0.02	18.02 ± 0.03	17.84 ± 0.05
1.0238	66	18.47 ± 0.04	18.14 ± 0.02	18.09 ± 0.03	17.92 ± 0.07
1.1549	115	18.50 ± 0.03	18.21 ± 0.02	18.16 ± 0.04	18.02 ± 0.05
1.3407	115	18.58 ± 0.04	18.31 ± 0.01	18.26 ± 0.03	18.12 ± 0.05
1.5249	115	18.67 ± 0.03	18.39 ± 0.02	18.36 ± 0.02	18.19 ± 0.05
1.7169	115	18.73 ± 0.02	18.46 ± 0.01	18.44 ± 0.03	
1.9195	115	18.80 ± 0.03	18.53 ± 0.02	18.50 ± 0.03	18.32 ± 0.05
2.1132	115	18.83 ± 0.03	18.58 ± 0.02	18.56 ± 0.02	18.44 ± 0.04
2.3095	115	18.90 ± 0.03	18.64 ± 0.01	18.63 ± 0.03	18.43 ± 0.05
2.5040	115	18.96 ± 0.03	18.70 ± 0.01	18.66 ± 0.02	18.51 ± 0.05
2.8368	375	19.04 ± 0.02	18.77 ± 0.01	18.76 ± 0.02	18.58 ± 0.03
3.2896	375	19.12 ± 0.02	18.88 ± 0.01	18.85 ± 0.01	18.73 ± 0.03
3.7418	375	19.20 ± 0.02	18.95 ± 0.02	18.93 ± 0.02	18.81 ± 0.03

Table 6.5: continued.

$T_{\mathrm{mid}} - T_0$ [ks]	Exposure [s]	Brightness[a] mag$_{\mathrm{AB}}$			
		g'	r'	i'	z'
4.1939	375	19.27 ± 0.02	19.02 ± 0.01	19.00 ± 0.02	18.86 ± 0.04
4.6568	375	19.32 ± 0.02	19.07 ± 0.01	19.05 ± 0.02	18.89 ± 0.03
5.1021	375	19.35 ± 0.02	19.11 ± 0.01	19.09 ± 0.02	18.98 ± 0.04
5.5542	375	19.38 ± 0.01	19.14 ± 0.01	19.11 ± 0.02	18.98 ± 0.03
6.0063	375	19.39 ± 0.02	19.15 ± 0.01	19.14 ± 0.02	19.02 ± 0.04
6.4708	375	19.40 ± 0.02	19.17 ± 0.01	19.15 ± 0.02	19.01 ± 0.03
6.9143	375	19.41 ± 0.02	19.18 ± 0.01	19.17 ± 0.02	19.04 ± 0.03
7.3624	375	19.42 ± 0.01	19.18 ± 0.01	19.17 ± 0.02	19.06 ± 0.03
7.8060	375	19.45 ± 0.01	19.21 ± 0.01	19.18 ± 0.02	19.05 ± 0.03
8.2685	375	19.46 ± 0.02	19.21 ± 0.01	19.20 ± 0.02	19.07 ± 0.04
8.7202	375	19.48 ± 0.02	19.24 ± 0.01	19.23 ± 0.02	19.09 ± 0.03
9.1693	375	19.50 ± 0.02	19.27 ± 0.01	19.26 ± 0.02	19.10 ± 0.04
9.6214	375	19.53 ± 0.01	19.29 ± 0.01	19.29 ± 0.02	19.14 ± 0.03
14.4446	375	19.70 ± 0.01	19.47 ± 0.01	19.43 ± 0.02	19.30 ± 0.04
15.3777	375	19.75 ± 0.01	19.50 ± 0.01	19.48 ± 0.02	19.32 ± 0.05
15.8274	375	19.78 ± 0.01	19.53 ± 0.01	19.51 ± 0.02	19.38 ± 0.03
16.2785	375	19.80 ± 0.01	19.54 ± 0.01	19.52 ± 0.02	19.39 ± 0.04
16.7300	375	19.81 ± 0.01	19.57 ± 0.01	19.50 ± 0.02	19.36 ± 0.04
17.3570	375	19.84 ± 0.02	19.58 ± 0.01	19.55 ± 0.02	19.41 ± 0.04
17.8057	375	19.87 ± 0.02	19.60 ± 0.01	19.58 ± 0.02	19.42 ± 0.04
18.2565	375	19.95 ± 0.03	19.63 ± 0.01	19.55 ± 0.04	19.46 ± 0.05
104.0014	686	21.82 ± 0.05	21.51 ± 0.03	21.44 ± 0.06	21.25 ± 0.09
170.5107	1714	22.47 ± 0.09	22.14 ± 0.06	22.19 ± 0.09	21.95 ± 0.11
188.6865	1724	22.62 ± 0.03	22.34 ± 0.03	22.43 ± 0.06	22.12 ± 0.09
344.9195	3521	23.28 ± 0.20	23.21 ± 0.15	23.12 ± 0.15	23.29 ± 0.17
438.7789	3520	> 23.83	23.80 ± 0.23	23.64 ± 0.28	> 23.48
872.9788	7136	> 24.19	> 23.92	> 23.87	> 23.85
1478.9968	7096	> 24.04	> 24.24	> 23.88	> 24.10
4832.0789	7182	> 24.81	> 25.50	> 24.02	> 24.37

[a] Corrected for Galactic foreground reddening.

Table 6.6 JHK_s photometric data of GRB 091029

$T_{\mathrm{mid}} - T_0$ [ks]	Exposure [s]	Brightness[a] $\mathrm{mag}_{\mathrm{AB}}^{[b]}$		
		J	H	K_s
0.3135	82	17.33 ± 0.08	17.26 ± 0.06	17.17 ± 0.11
0.4171	82	17.22 ± 0.08	17.13 ± 0.06	16.91 ± 0.09
0.5221	82	17.34 ± 0.07	17.23 ± 0.06	17.13 ± 0.11
0.8835	377	17.72 ± 0.03	17.61 ± 0.05	17.28 ± 0.07
1.4625	729	18.09 ± 0.03	17.94 ± 0.04	17.59 ± 0.08
2.2379	754	18.35 ± 0.03	18.45 ± 0.06	17.98 ± 0.10
3.5383	1780	18.63 ± 0.03	18.57 ± 0.05	18.55 ± 0.11
5.3549	1772	18.91 ± 0.04	18.80 ± 0.05	18.68 ± 0.13
7.1614	1758	18.98 ± 0.04	18.86 ± 0.06	18.68 ± 0.11
8.9684	1775	19.01 ± 0.04	19.12 ± 0.06	18.91 ± 0.14
16.0777	1777	19.31 ± 0.05	19.24 ± 0.08	18.98 ± 0.17
18.0561	1775	19.33 ± 0.05	19.30 ± 0.07	19.11 ± 0.19
104.0267	739	21.33 ± 0.40	> 20.16	> 19.53
105.2524	1644	21.27 ± 0.29	> 20.48	> 19.70
170.5336	1762	21.79 ± 0.38	> 20.83	> 19.98
188.7100	1773	21.90 ± 0.32	> 21.12	> 20.23
344.9423	3569	> 21.77	> 21.40	> 20.66
438.8024	3569	> 21.68	> 21.10	> 20.80
873.0025	7184	> 22.03	> 21.43	> 21.14
1479.0224	7142	> 22.07	> 21.51	> 20.98
4832.1018	7230	> 22.12	> 21.54	$-$

[a] Corrected for Galactic foreground reddening. Converted to AB magnitudes for consistency with Table 6.5.

[a] For the SED fitting, the additional error of the absolute calibration of 0.05 (J and H) and 0.07 (K_s) mag was added.